1

Introduction

Background

Fluorescence-based technologies are widely used in biochemical research, drug discovery, and clinical diagnosis. They have become one of the leading methods in cell biology, genomics and proteomics. Examples of current applications of fluorescence include DNA sequencing, clinical assays, studies of metabolic enzyme activity, identification of biomolecules, and genetic analysis by fluorescence in situ hybridization. Fluorescence occurs in many molecules but it is most widespread among aromatic compounds. Typical fluorescent substances, also referred to as fluorophores, include fluorescein and rhodamin B. They can be covalently attached to another molecule, such as a protein or nucleic acid, in a procedure called fluorescent labeling. The most common approach involves fluorescent labeling of antibodies, which are then used as molecularly specific probes for detection of a particular biomolecular target.

One of the current fundamental challenges in fluorescence detection is to enhance the fluorophores' brightness. This will make it possible to analyze rare biomolecules in a cell or selected cells within complex biological samples such as tissues or other complex media. This capability is important because trace amounts of specific biomolecules often carry essential information from a biological/medical point of view important for early-stage disease diagnosis or new drug discoveries. This requires a fluorophore to have high fluorescence intensity and high photostability. However, most traditional fluorophores, especially those with long fluorescence lifetimes, produce weak optical signals and the majority are prone to photobleaching. Additionally most biological samples suffer from strong interfering autofluorescence background. These drawbacks impose serious limitations and prevent fluorescence-based techniques to achieve high sensitivity. Although new nanoparticle-based fluorophores, e.g. semiconductor quantum dots, have been intensely investigated due to their higher photostability and high brightness, they frequently tend to aggregate and are difficult to apply in many biological settings. Therefore, molecular fluorophores are still preferred in the fluorescence labeling-based studies.

In comparison with the challenges facing the development of nanoparticle-based fluorophores, the application of metal nanostructures is an effective and low-cost way to improve the optical properties of fluorophores. This approach is based on the fluorophore-metal interaction within the optimal distance between fluorophores and metal nanostructures, which results in fluorescence enhancement [1–5], hence it is termed "metal enhanced fluorescence" (MEF). MEF has a long scientific history, perhaps starting with the classic reports of Drexhage [6] in 1970, and has now become a leading technology to increase fluorescence detection sensitivity, especially in diagnostic setting, such as immunoassays. In the same period another surface-sensitive technique known as Surface -Enhanced Raman Scattering (SERS) has been established [7, 8]. SERS produces several orders of magnitude enhancement of the Raman scattering cross-section from molecules on rough metal surfaces. Although the two effects are related, the conditions in which they occur are very different. The optimal MEF signal occurs at a certain distance between fluorophores and the metal, owing to quenching of

fluorescence via Förster energy transfer to the metal [1]. In particular, fluorophores in direct contact to the metal are typically completely quenched. In contrast, the SERS signal is maximally enhanced when molecules are immediately adjacent to the metal. Due to the interaction between metal nanostructures and fluorophores, the MEF technique has been shown to produce desirable effects such as increased fluorescence emission efficiency ("quantum yield") and improved photostability of fluorophores [2, 3]. In addition, MEF can significantly increase the efficiency of Förster resonance energy transfer (FRET) between two fluorophores, known as the donors and acceptors. This is significant for traditional FRET assays, where both the donors and the acceptors are prone to photodegradation, which decreases the measured FRET efficiency [9].

The aim of this PhD project is to develop metal nanostructures used as MEF substrates and their potential in fluorescence-based applications requiring very high sensitivity. To this aim, two types of MEF substrates were firstly synthesized and characterized. One is the silver nanostructure-coated silica bead (400 nm and 5μm) which was suitable for flow cytometry based bead immunoassays and cell imaging. Another is europium chelate-doped Ag@SiO_2 nanostructure which was bright enough to be observed as the singal nanocomposite under high excitation. Then a series of experiments were designed to investigate the potential biological applications of these MEF substrates. The detailed project objectives are listed in the following section.

Objectives

The previously MEF substrates were mainly developed on the planar platform such as the glass slide. Such architecture usually limited their applications to the solid surface, preventing other applications in solution-based sensing platform. Recently more interests were focused on core-shell nanostructures due to their potential in a range of biological applications such as immunoassays and bioimaging whose labeling needs to be carried out in the solution. Therefore, this project aimed to synthesize such nanostructures and evaluate their performance in the above applications. The main the objectives included the following 5 parts:

1. To engineer and characterize metal nanostructures (Ag-coated silica beads and Ag@SiO_2 nanocomposites)which are more suitable in suspension system.

2. To test the ability of Ag-coated silica beads to enhance fluorescence intensity from some conventional fluorophores (such as Alexa 430 and Eu chelates) using the model immunoassay and cell imaging in both solide surface (the glass slide) and suspension system (flow cytometry).

3. To study the feasibility of Ag-coated silica beads to increase upconversion luminescence signal from $NaYF_4 : Yb, Er$ nanoparticles using the streptavidin-biotin binding system.

4. To demonstrate the performance of $Ag@SiO_2$ nanocomposites in MEF using the model bioassay where these Eu chelate-doped nanocomposites were firstly conjugated with strepptavidin and then attached to biotinylated antibody molecules.

5. To understand the mechanism for the high enhancement induced by these nanostructures.

Thesis Structure

The whole thesis consists of nine chapters. Chapter 1 introduces the background and the significance for conducting this project, and outlines the main objectives. Chapter 2 presents a summary of fluorescence phenomenon and techniques of relevance for fluorescence detection. Chapter 3 reviews the MEF technique and its biological applications.

Chapter 4 describes the preparation of Ag nanostructures-coated silica microspheres, their characterisation and the application in an enhanced fluorescence immunoassay compatible with flow cytometry readout. These Ag nanostructures greatly increased the fluorescence emission of Alex 430 fluorophore excited at 430 nm via the immunoassay model. At the same time, the lifetime was dramatically reduced by 3.5-fold compared to the sample without Ag nanostructures. Additionally, they were also applied to the flow cytometry experiment where the flurescence enhancemnt factor was lower than that in the immunoassy due to the less favourable overlap of the plasmons band with 488 excitation used in the flow cytometry. Work shown in Chapter 5 was another demonstration of these silica beads in biological applications. The fluorescence intensity enhancement factor of $BHHCT - Eu^{3+}$, a new type of Eu chelate, induced by these silica beads was about 11 times, while the simultaneously measured fluorescence

lifetime was reduced twofold. The mechanism responsible for this phenomenon was also discussed. Subsequently, they were applied to time-gated fluorescence imaging of Giardia lamblia cells stained by $BHHCT - Eu^{3+}$ with improvement in brightness by a factor of two. Chapter 6 introduces luminescence from upconversion nanoparticles which can be used in MEF as a new tpye of biolabel materials. Chapter 7 demonstrates the ability of these Ag-coated silica beads to increase the upconversion intensity from $NaYF_4 : Yb, Er$ nanoparticles using a simple bioassay. In Chapter 8, I demonstrated feasibility of another type of MEF substrate, enhanced luminescence from Eu chelate-doped $Ag@SiO_2$ nanocomposites, where both the silver-fluorophore distance and the Ag-core size are adjusted to optimize the luminescence enhancement. Based on these experimental results, we estimated the mechanism contributing to the high enhancement. The final chapter, Chapter 9, summarizes of the work through my PhD study and outlines possible research prospect in this field.

2

Fluorescence and Fluorescence Instrumentation (review)

2.1 Fluorescence

Luminescence is a process in which susceptible molecules emit light from electronically excited states created by either a physical (for example, absorption of light), mechanical (friction), or chemical mechanism. Generation of luminescence through excitation of a molecule by ultraviolet or visible light photons is termed photoluminescence. It is formally divided into two categories, fluorescence and phosphorescence, depending upon the electronic configuration of the excited state and the emission pathway. Fluorescence involves atoms and molecules absorbing light at a particular wavelength which is subsequently emitted light at longer wavelengths after a brief interval, termed the fluorescence lifetime. The process of phosphorescence occurs in a manner

similar to fluorescence, but with a much longer excited state lifetime. Fluorescence is now a dominant methodology used extensively in biotechnology, flow cytometry, medical diagnostics, DNA sequencing, forensics, and genetic analysis, to name a few [10]. There has been dramatic growth in the use of fluorescence detection for cellular and molecular imaging. Fluorescence imaging can reveal the localization and measurements of intracellular molecules, sometimes at the level of single-molecule detection.

2.1.1 The fluorescence process

Fluorescence is a result of a three-stage process that occurs in certain molecules (generally polyaromatic hydrocarbons or heterocycles) called fluorophores or fluorescent dyes. A fluorescent probe is a fluorophore designed to respond to a specific stimulus or to localize within a specific region of a biological specimen. The process responsible for the fluorescence of fluorescent probes and other fluorophores is illustrated by a typical Jablonski diagram (see Fig. 5.1).

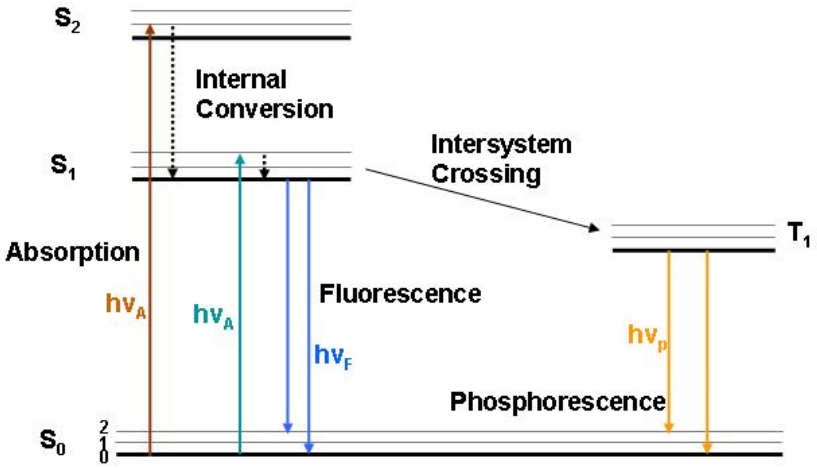

FIGURE 2.1: Example of Jablonski diagram

The singlet ground, first, and second electronic states are denoted by S_0, S_1, and S_2, respectively. At each of these electronic energy levels the fluorophores can exist in a number of vibrational energy levels, denoted by 0, 1, 2, etc. In this Jablonski diagram we ignored a number of interactions, such as quenching, energy transfer, and solvent interactions. The transitions between states are denoted as vertical lines to illustrate the instantaneous nature of light absorption.

A photon of energy is supplied by an external source such as an incandescent lamp or a laser and absorbed by the fluorophore, creating an excited electronic singlet state. This process distinguishes fluorescence from chemiluminescence, in which the excited state is populated by a chemical reaction. Once a fluorophore molecule has absorbed energy, there are a number of routes by which it can return to the ground state.

Firstly, two radiative processes will occur after absorption of energy by a molecule. If the photon emission occurs between the same spin states (e.g. $S_1 \rightarrow S_0$) this is termed fluorescence (shown in shorter wavelength blue). If the spin state of the initial and final energy levels are different (e.g. from the first triplet state T_1 to the singlet ground state S_0), the emission is called phosphorescence (shown in longer wavelength red). Since fluorescence is statistically much more likely than phosphorescence, the lifetimes of fluorescent states are very short (1×10^{-5} to 10^{-8}s) and phosphorescence somewhat longer (1×10^{-4}s to minutes or even hours).

In addition, three nonradiative deactivation processes are also significant here: internal conversion (IC), intersystem crossing (ISC) and vibrational relaxation. Examples of the first two can also be seen in this diagram. Internal conversion is the radiationless transition between energy states of the same spin state (shown with vertical dashed lines)and generally occurs within 10^{-12}s or less. Since fluorescence lifetimes are typically near 10^{-8}s, internal conversion is generally complete prior to emission. Hence, fluorescence emission generally results from a thermally equilibrated excited state, that is, the lowest energy vibrational state of S_1. Conversion of S_1 to T_1 is called intersystem crossing (shown with the solid line). Since the heavy atoms facilitate intersystem crossing and enhance phosphorescence quantum yields, molecules containing heavy atoms such as bromine and iodine are frequently phosphorescent. Vibrational relaxation, the most common of the three-for most molecules, occurs very quickly ($<1 \times 10^{-12}$s) and is enhanced by physical contact of an excited molecule with other particles, where the energy, in the form of vibrations and rotations, can be transferred through collisions. In a solution, thermal relaxation of a vibrationally excited molecule is quite rapid through transfer of excess vibrational energy from the solute molecule to the solvent. This means that an excited molecule in a solution will firstly undergo vibrational

relaxation, and then emit a photon from the lowest vibrational level of an excited state.

2.1.2 Fluorescence lifetimes and quantum Yields

The fluorescence lifetime and quantum yield are perhaps the most important characteristics of a fluorophore.Their meanings are best represented by a simplified Jablonski diagram (see Fig. 5.2) [10]. In this diagram we focus on those processes responsible for return to the ground state. In particular, we are interested in the radiative decay rate of the fluorophore (Γ) and its nonradiative decay rate (K_{nr}).

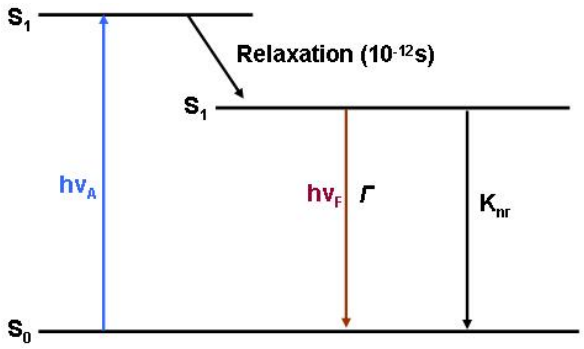

FIGURE 2.2: A simplified Jablonski diagram to illustrate the meaning of quantum yields and lifetimes.

The fluorescence lifetime refers to the average time the molecule stays in its excited state before emitting a photon. For the fluorophore illustrated in Fig. 5.2 the lifetime (τ) is given by,

$$\tau = \frac{1}{\Gamma + k_{nr}} \tag{2.1}$$

For commonly used fluorescent compounds typical excited state decay times for fluorescent compounds that emit photons with energies from the UV to near infrared are within the range of 0.5 to 20 nanoseconds. The fluorescence lifetime is an important parameter for practical applications of fluorescence such as fluorescence resonance energy transfer, beacuse it determines the time available for the fluorophore to interact with or diffuse in its environment, and the information available from its emission.

Quantum yield, Q, is the number of emitted photons relative to the number of absorbed photons, as follows:

$$Q = \frac{\texttt{Number of photons emitted}}{\texttt{Number of photons absorbed}} \tag{2.2}$$

For the fluorophore illustrated in Fig. 5.2 Q is given by,

$$Q = \frac{\Gamma}{\Gamma + k_{nr}} \tag{2.3}$$

The quantum yield can be close to unity if the radiationless decay rate is much smaller than the rate of radiative decay, that is $k_{nr}<\Gamma$. We note that the energy yield of fluorescence is always less than unity because of Stokes losses. The maximum fluorescence quantum yield is 1.0 (100%), which means every photon absorbed results in a photon emitted. Compounds with quantum yields of 0.10 are still considered quite fluorescent. Fluorescence quantum yield are usually measured by comparison to a standard with known quantology. The quinine salt, quinine sulfate, in a sulfuric acid solution is a common fluorescence standard.

The quantum yield and lifetime can be modified by factors that affect either Γ or k_{nr}. For example, a molecule may be nonfluorescent as a result of a large rate of internal conversion or a slow rate of emission. Scintillators are generally chosen for their high quantum yields. These high yields are a result of large Γ values. Hence, the lifetimes are generally short, near 1 ns. In addition, the quantum yields of phosphorescence are extremely small in fluid solutions at room temperature. The reason can be attributed as follows: the triplet-to-singlet transition is forbidden by symmetry, therefore Γ values are about $10^3 s^{-1}$ or smaller; on the other hand k_{nr} values are near $10^9 s^{-1}$. From Eq. 2.2 one can predict phosphorescence quantum yields of 10^{-6}.

2.1.3 Fluorescence quenching

Quenching refers to any process which decreases the fluorescence intensity of a given substance. A variety of processes can result in quenching, such as excited state reactions, energy transfer, complex-formation and collisional quenching. As a consequence, quenching is often heavily dependent on pressure and temperature. Molecular oxygen and the iodide ion are common chemical quenchers. Quenching poses a problem for non-instant spectroscopic methods, such as laser-induced fluorescence.

Now we discuss collisional quenching which is illustrated on the modified Jablonski diagram (see Fig. 5.3) [10].

In this case the fluorophore is returned to the ground state during an encounter

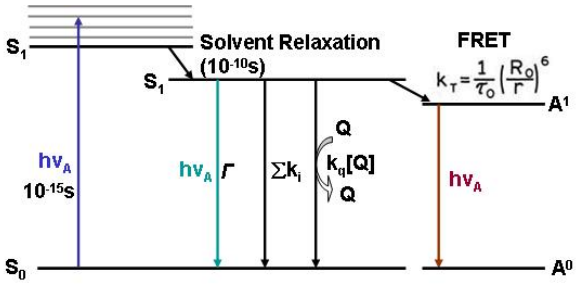

FIGURE 2.3: Jablonski diagram with collisional quenching and fluorescence resonance energy transfer (FRET). The term $\sum k_i$ is used to represent non-radiative paths to the ground state aside from quenching and FRET.

with the quencher. The molecules are not chemically altered in the process. For collisional quenching the decrease in intensity is described by the well-known Stern-Volmer equation:

$$F_0/F = 1 + K[Q] = 1 + k_q\tau_0[Q] \tag{2.4}$$

In this expression K is the Stern-Volmer quenching constant, k_q is the bimolecular quenching constant, τ_0 is the unquenched lifetime, and [Q] is the quencher concentration. The Stern-Volmer quenching constant K indicates the sensitivity of the fluorophore to a quencher. A fluorophore buried in a macromolecule is usually inaccessible to quenchers, so that the value of K is low. Larger values of K are found if the fluorophore is free in solution or on the surface of a biomolecule.

Aside from collisional quenching, fluorescence quenching can occur by a variety of other processes. Fluorophores can form nonfluorescent complexes with quenchers. This process is referred to as static quenching since it occurs in the ground state and does not rely on diffusion or molecular collisions. Quenching can also occur by a variety of trivial, i.e., non-molecular mechanisms, such as attenuation of the incident light by the fluorophore itself or other absorbing species.

2.1.4 Application of fluorescence in biochemistry and medicine

Fluorescence in the life sciences is used generally as a non-destructive way of tracking or analysis biological molecules by means of the fluorescent emission at a specific frequency where there is no background from the excitation light, as relatively few cellular components are naturally fluorescent (called intrinsic or autofluorescence). In

fact, a protein or other component can be "labelled" with a extrinsic fluorophore, a fluorescent dye which can be a small molecule, protein or quantum dot, finding a large use in many biological applications [10]. The main applications are as follows:

1. Immunoassay. An immunoassay is a biomedical assay based on specific binding between an antibody and an antigen. The antibody that specifically binds to the antigen can usually be labelled with a fluorescent reagent. The immunoassay can measure the presence or concentration of a substance in solutions that frequently contain a complex mixture of biomaterials via the fluorescence detection.

2. Fluorescence microscopy. Fluorescence microscopy is often used to image specific features of tissues, cells or subcellular structures. It is also used to conduct viability studies on cell populations.These can be accomplished by labeling an antibody with a fluorophore and allowing the antibody to find its target antigen within the sample. When the reflected light and background fluorescence is filtered in this type of microscopy the targeted parts of a given sample can be imaged. In addition, labeling multiple antibodies with different fluorophores allows visualization of multiple targets within a single image (multiple channels).

3. Fluorescent-activated cell sorting. It is a specialized type of flow cytometry where the cell suspension is entrained in the center of a narrow, rapidly flowing stream of liquid. Just before the stream breaks into droplets, the flow passes through a fluorescence measuring station where the fluorescent properties of each labelled cell is measured, therefore providing fast, objective and quantitative recording of fluorescent signals from individual cells.

2.2 Fluorescence instruments

The following part will give a brief review on the fluorescence instrumentations which are necessary for this project, such as fluorescence spectroscopy, epifluorescence microsopy and confocal microscopy with Fluorescence Lifetime Imaging Microscopy (FLIM).

2.2.1 Fluorescence spectroscopy

Spectral properities of fluorophores are usually recorded with spectrophotometers. A spectrophotometer is a photometer that measures the intensity of radiation as a

function of frequency (or wavelength) of the radiation. There are many kinds of spectrophotometers. Among the most important distinctions used to classify them are the wavelengths they work with, the measurement techniques they use, how they acquire a spectrum, and the sources of intensity variation they are designed to measure. Fig. 5.4 shows a schematic diagram of a general-purpose spectrofluorometer [10]. This instrument has a xenon lamp as a source of exciting light. Such lamps are generally useful because of their high intensity at all wavelengths ranging upward from 250 nm. The instrument shown is equipped with monochromators to select both the excitation and emission wavelengths. The excitation monochromator in this schematic contains two gratings, which decrease stray light, that is, light with wavelengths different from the chosen one. In addition, these monochromators use concave gratings, produced by holographic means to further decrease stray light. Both monochromators are motorized to allow automatic scanning of wavelength. The fluorescence is detected with photomultiplier tubes and quantified with the appropriate electronic devices. The output is usually presented in graphical form and stored digitally.

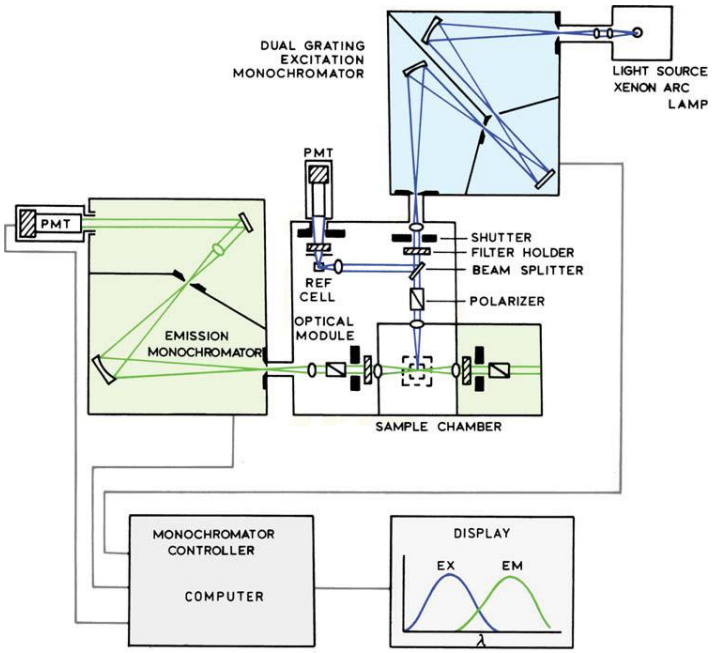

FIGURE 2.4: Schematic diagram of a spectrofluorometer.

Light sources

We now describe the individual components of a spectrofluorometer. The general characteristics of these components are considered along with the reason for choosing specific components. Understanding the characteristics of these components allows one to understand the capabilities and limitations of spectrofluorometers. We will first consider light sources.

At present the most versatile light source for a steady-state spectrofluorometer is a high-pressure xenon (Xe) arc lamp. These lamps provide a relatively continuous light output from 250 to 700 nm. Xenon arc lamps emit a continuum of light as a result of recombination of electrons with ionized Xe atoms. These ions are generated by collisions of Xe atoms with the electrons that flow across the arc. Complete separation of the electrons from the atoms yields the continuous emission. Xe atoms that are in excited states but not ionized yield lines rather than broad emission bands. The output intensity drops rapidly below 280 nm. Furthermore, many Xe lamps are classified as being ozone-free, meaning that their operation does not generate ozone in the surrounding air.

The wavelength-dependent output of Xe lamps is a major reason for distortion of the excitation spectra of compounds that absorb in the visible and ultraviolet. To illustrate this effect Fig. 5.5 shows corrected and uncorrected excitation fluorescein spectra. The uncorrected spectra are recorded emission intensities with no correction for wavelength-dependent excitation intensity. The uncorrected excitation spectrum displays a number of peaks near 450 nm. These peaks are due to the output of the Xe lamp, which also displays peaks near 450 nm. Also shown in Fig. 5.5 is the excitation spectrum, corrected for the wavelength-dependent output of the Xe arc lamp.

Monochromators

Monochromators are used to disperse polychromatic or white light into the various colors or wavelengths. This dispersion can be accomplished using prisms or diffraction gratings. The monochromators in most spectrofluorometers use diffraction gratings rather than prisms. The performance specifications of a monochromator include dispersion, efficiency, and stray light levels. Dispersion is usually given in nm/mm. The slit width is sometimes expressed in mm, which requires knowledge of the dispersion.

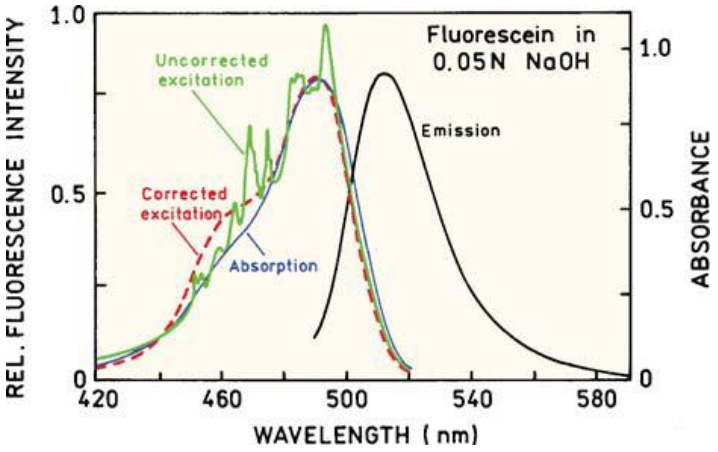

FIGURE 2.5: Corrected and uncorrected excitation spectra of fluorescein.

A monochromator for fluorescence spectroscopy should have low stray light levels to avoid problems due to scattered or stray light. Monochromators are also chosen for high efficiency to maximize the ability to detect low light levels.

Monochromators can have planar or concave gratings (Fig. 5.6). Planar gratings are usually produced mechanically. Concave gratings are usually produced by holographic and photoresist methods. Monochromators based on concave gratings can have fewer reflecting surfaces, lower stray light, and can be more efficient. A concave grating can serve as both the diffraction and focusing element, resulting on one instead of three reflecting surfaces. For these reasons the holographic gratings are usually preferable for fluorescence spectroscopy.

Optical filters

While spectrofluorometers have monochromators for wavelength selection, it is often important to use optical filters in addition to monochromators. Optical filters are used to compensate for the less-than-ideal behavior of monochromators. A large range of filters are available. The manufacturers typically provide the transmission spectra of the filters. Before the advances in thin film technology, most filters were colored-glass filters. Colored-glass filters can transmit a range of wavelengths (Fig. 5.7, top). Some color filters are called long-pass filters and transmit all wavelengths above some particular wavelength (Fig.5.7, bottom). The names of the filters divide them into classes according to their colors (BG, blue glass, GG, green glass, etc.).

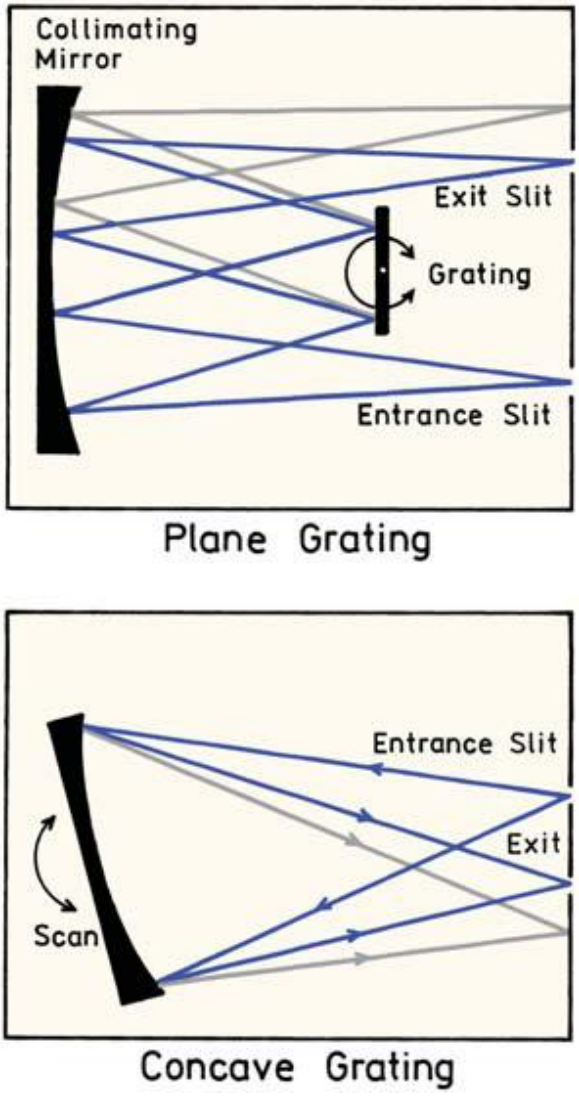

FIGURE 2.6: Monochromators based on a plane (top) or concave (bottom) grating.

A wide variety of colored-glass filters are available, but the transmission curves are not customized for any given application. During the past ten years there have been significant advances in the design of thin-film optical filters [11]. Almost any desired transmission curve can be obtained. Filters are now being designed for specific applications, rather than choosing the colored-glass filter that best suits an application. Long-pass filters are an example of this type filter (Fig. 5.8). These filters have a sharp cut on the transmission above 325 nm or 488 nm, which are wavelengths available from a helium-cadmium or argon ion laser, respectivel. The transmission above the cut-on

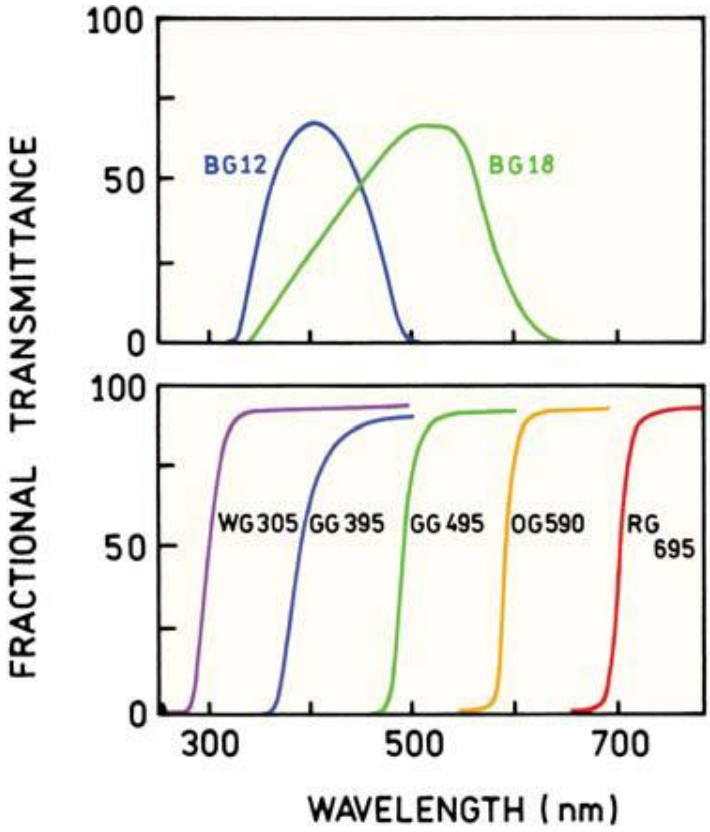

FIGURE 2.7: Transmission spectra of some typical colored glass filters.

wavelength is close to 100% to provide maximum sensitivity.

Photomultiplier tubes

Almost all fluorometers use photomultiplier tubes (PMTs) as detectors, and it is important to understand their capabilities and limitations. A PMT is best regarded as a current source. The current is proportional to the light intensity. A PMT responds to individual photons, and the pulses can be detected as an average signal or counted as individual photons. A PMT vacuum tube consists of a photocathode and a series of dynodes which are the amplification stages (Fig. 5.9). The photocathode is a thin film of metal on the inside of the window. Incident photons cause electrons to be ejected from this surface. The generation efficiency of photoelectrons is dependent upon the incident wavelength. The photocathode is held at a high negative potential, typically -1000 to -2000 volts.

For quantitative measurements, the anode current must be proportional to the

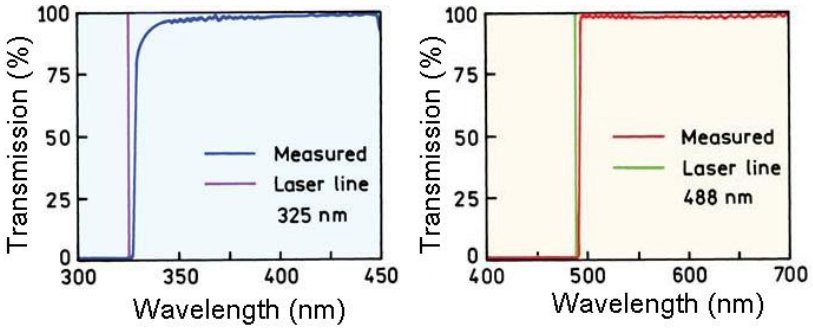

FIGURE 2.8: Long-pass filters designed to reject light from a helium-cadmium laser at 325 nm or an argon ion laser at 488 nm.

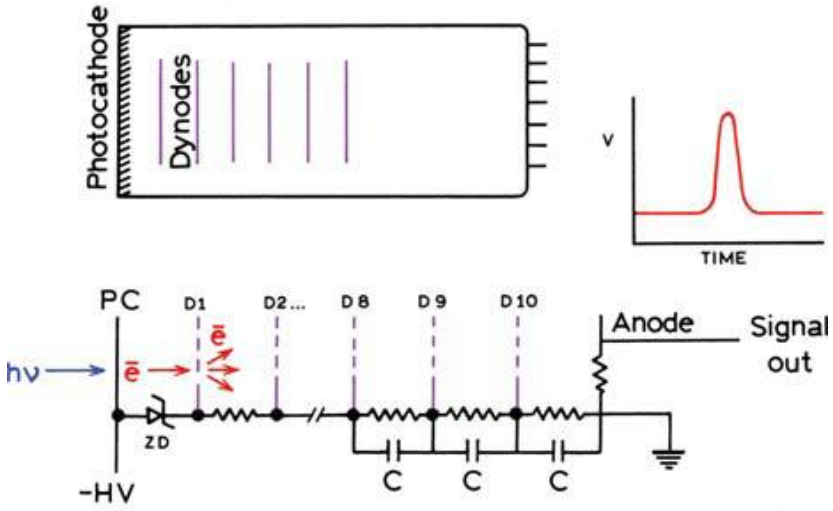

FIGURE 2.9: Schematic diagram of a photomultiplier tube and its dynode chain.

light intensity. A nonlinear response can result from an excessive current being drawn from the photocathode. Under high-intensity illumination the electrical potential of the photocathode can be decreased because of its limited current-carrying capacity. This decreases the voltage difference between the photocathode and the first dynode, and also decreases the gain. Excessive photocurrents can damage the light-sensitive photocathodes, resulting in loss of gain and excessive dark currents. The dark current from a PMT is the current in the absence of incident light.

PMTs are available in a wide variety of types. They can be classified in various ways, such as according to the design of the dynode chain, size, and shape, spectral response, or temporal response.

Sample containers

The sample containers, cells or cuvettes, must be fabricated from material that is transparent to radiation in the spectral region of interest. The commonly used materials for different wave length regions are:

Quartz or fused silica: UV to 2 μm in IR

Silicate glass: Above 350 nm to 2 μm in IR

Plastic: visible region

Polished NaCl or AgCl: Wave lengths longer than 2 μm

Cuvettes or cells are provided in pairs that have been carefully matched to make possible the transmission through the solvent and the sample. Accurate spectrophotometric analysis requires the use of good quality, matched cells. These should be regularly checked against one another to detect differences that can arise from scratches, etching and wear. The most common cell path for UV-visible region is 1 cm. For reasons of economy, cylindrical cells are frequently used. Care must be taken to duplicate the position of such cells with respect to the light path; otherwise, variations in path length and in reflection losses will introduce errors.

2.2.2 Flow cytometry

Flow cytometry is a powerful technique for the analysis of multiple parameters of individual cells within heterogeneous populations. Flow cytometers are used in a range of applications from immunophenotyping, to cell counting and GFP (green fluorescent protein) expression analysis. The flow cytometer performs this analysis by passing thousands of cells per second through a laser beam and capturing the light that emerges from each cell as it passes through. The data gathered can be analyzed statistically by flow cytometry software to report cellular characteristics suac as size, relative granularity or internal complexity, and relative fluorescence intensity (see Fig. 5.10) [12–14].

A flow cytometer is made up of some systems: fluidic system, Lasers or arc lamps, the optics, the detectors and electronics.

1. The fluidic system presents samples to the interrogation point and takes away the waste.

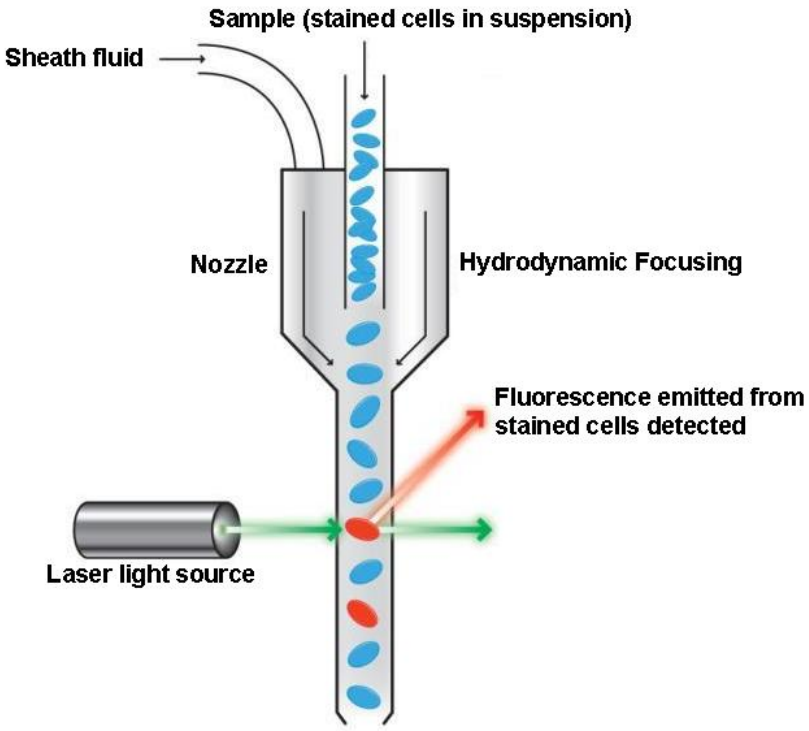

FIGURE 2.10: Schematic diagram of a flow cytometer.

2. Lasers (or arc lamps) are the light source for scatter and fluorescence.

3. The optics gather and direct the light signals to the the appropriate detectors.

4. The detectors receive the light.

5. The electronics system converts the signals from the detectors into digital data and performs necessary analyses.

Fluidic system

One of the fundamentals of flow cytometry is the ability to measure the properties of individual particles. When a sample in solution is injected into a flow cytometer, the particles are randomly distributed in three-dimensional space. The sample must therefore be ordered into a stream of single particles that can be interrogated by the machines detection system. This process is managed by the fluidics system.

Essentially, the fluidics system consists of a central channel/core through which the sample is injected, enclosed by an outer sheath that contains faster flowing fluid. As the sheath fluid moves, it creates a massive drag effect on the narrowing central chamber. This alters the velocity of the central fluid whose flow front becomes parabolic

with greatest velocity at its center and zero velocity at the wall. The effect creates a single file of particles and is called hydrodynamic focusing. Under optimal conditions (laminar flow) the fluid in the central chamber will not mix with the sheath fluid (see Fig. 5.11).

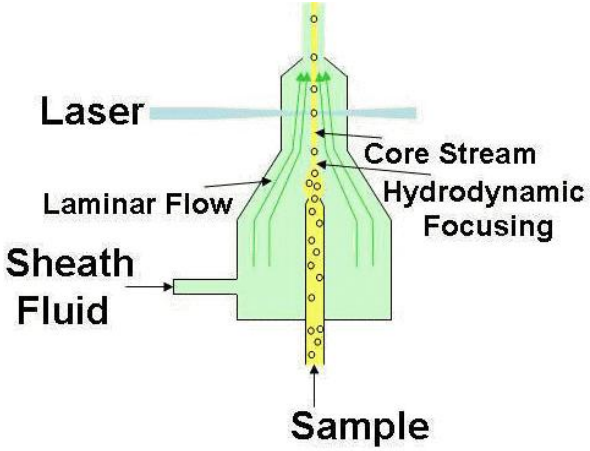

FIGURE 2.11: Hydrodynamic focusing of the sample core through a flow cell.

The flow characteristics of the central fluid can be estimated using Reynolds Number (R_e):

$$R_e = \frac{pVD}{\mu} \tag{2.5}$$

where D is tube diameter, V is mean velocity of fluid, p is density of fluid, and μ is viscosity of fluid. When $R_e < 2300$, flow is always laminar. When $R_e > 2300$, flow can be turbulent, which accelerates diffusion. Without hydrodynamic focusing the nozzle of the instrument (typically 70 μM) would become blocked, and it would not be possible to analyze one cell at a time.

Optics and detection

After hydrodynamic focusing, each particle passes through one or more beams of light. Light scattering or fluorescence emission (if the particle is labeled with a fluorophore) provides information about the particle's properties. The laser and the arc lamp are the most commonly used light sources in modern flow cytometry. Lasers produce a single wavelength of light at one or more discreet frequencies. Arc lamps tend to be less expensive than lasers and exploit the color emissions of an ignited gas

within a sealed tube.

However, this produces unstable incoherent light of a mixture of wavelengths, which needs subsequent optical filtering. Light that is scattered in the forward direction, typically up to 20 degrees offset from the laser beam's axis, is collected by a lens known as the forward scatter channel (FSC). The FSC intensity roughly equates to the particle's size and can also be used to distinguish between cellular debris and living cells. FSC provides a suitable method of detecting particles greater than a given size independent of their fluorescence and is therefore often used in immunophenotyping to trigger signal processing. Light measured approximately at a 90 degrees angle to the excitation line is called side scatter which is proportional to cell granularity or internal complexity. The side scatter channel (SSC) provides information about the granular content within a particle. SSC is a measurement of mostly refracted and reflected light that occurs at any interface within the cell where there is a change in refractive index (Fig. 5.12). Both FSC and SSC are unique for every particle, and a combination of the two may be used to differentiate different cell types in a heterogeneous sample.

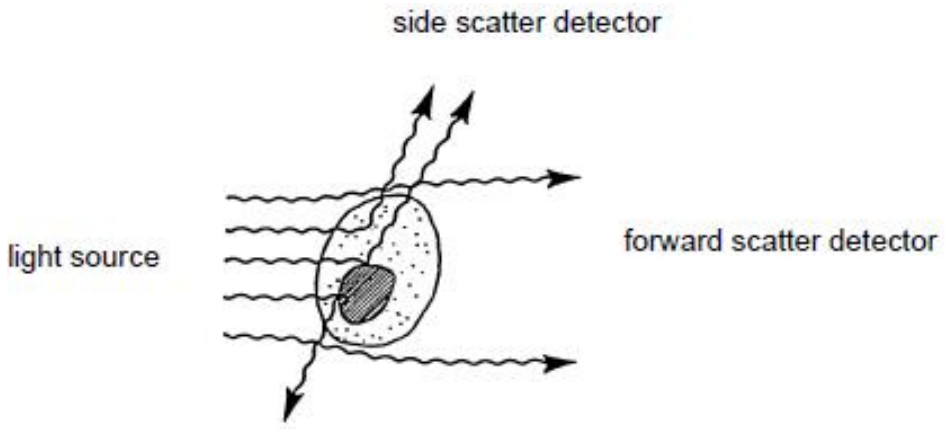

FIGURE 2.12: Light-scattering properties of a cell.

Flow cytometers use separate fluorescence channels to detect light emitted. The fluorescent light coming from labeled cells as they pass through the laser travels along the same path as the side scatter signal. As the light travels along this path, it is directed through a series of filters and mirros, so that particular wavelength ranges are delivered to the appropriate detectors. The number of detectors will vary according to

the machine and its manufacturer. Detectors are either silicon photodiodes or PMTs. Silicon photodiodes are usually used to measure forward scatter when the signal is strong. PMTs are more sensitive instruments and are ideal for scatter and fluorescence readings.The specificity of detection is controlled by optical filters, which block certain wavelengths while transmitting others. To detect multiple signals simultaneously, the precise choice and order of optical filters will be an important consideration.

2.2.3 Epifluorescence microscopy

Fluorescence microscopy has become an essential tool in biology as well as in materials science as it has attributes that are not readily available in other optical microscopy techniques, such as phase gradients, light absorption, and birefringence. The use of an array of fluorophores has made it possible to identify cells and submicroscopic cellular components and entities with a high degree of specificity amid nonfluorescing material. The fluorescence microscope can reveal the presence of a single fluorescing molecule. In a sample, through the use of multiple staining, different probes can simultaneously identify several target molecules. Although the fluorescence microscope cannot provide spatial resolution below the diffraction limit of the respective objects, the detection of fluorescing molecules below such limits is readily achieved.

Most fluorescence microscopy is performed using the epifluorescence configuration. The term epifluorescence refers to excitation and emission passing through the same objective (see Fig. 5.13). Epifluorescence microscopy is a method of fluorescence microscopy that is widely used in life sciences. The excitatory light is passed from above (or, for inverted microscopes, from below), through the objective and then onto the specimen instead of passing it first through the specimen (In the latter case the transmitted excitation light reaches the objective together with light emitted from the specimen). The fluorescence in the specimen gives rise to emitted light which is focused to the detector by the same objective that is used for the excitation. A filter between the objective and the detector filters out the excitation light from fluorescent light. Since most of the excitation light is transmitted through the specimen, only reflected excitation light reaches the objective together with the emitted light and this method therefore gives an improved signal to noise ratio. Additionally, the excitation can be

observed for the same location. Even though most of the excitation passes through the sample, a substantial fraction of the excitation is reflected or scattered back into the objective. A common use in biology is to apply fluorescent stains to the specimen in order to image a protein or other molecule of interest. These microscopes have become an important part in the field of biology, opening the doors for more advanced microscope designs, such as the confocal microscope and the total internal reflection fluorescence microscope (TIRF).

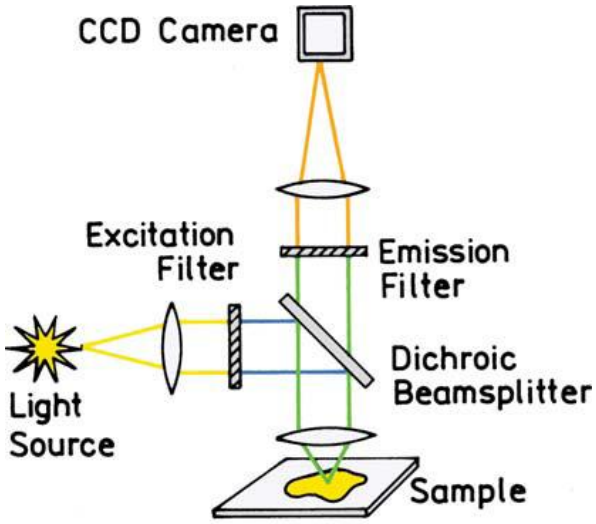

FIGURE 2.13: Schematic of a typical epifluorescence microscopy.

2.2.4 Confocal Microscopy

Although conventional light and fluorescence microscopy allow the examination of both living and fixed specimens, certain problems exist with these techniques. One of the main problems is multiple scattering of the light in thick specimens, as the light that enters the sample undergoes many scattering events resulting in a reduction in image contrast and a decrease in resolution.

In the confocal microscope all out-of-focus structures are suppressed at image formation. This is obtained by the following sollutions. On one hand, point by point illumination of the sample is employed to minimize aberrant rays of scattered light from regions outside the image plane of interest. On the other hand, a pinhole aperture in the image plane on the other side of the objective is used to reject out-of-focus light.

It means that such pinhole does not permit rays of light from out-of-focus points to pass through it. The emitted light passing through the detector pinhole is transformed into electrical signals by a photomultiplier and displayed on a computer monitor (See Fig. 9.7). Therefore, these two improvements enabled confocal microscopy to become a powerful tool for many scientific fields.

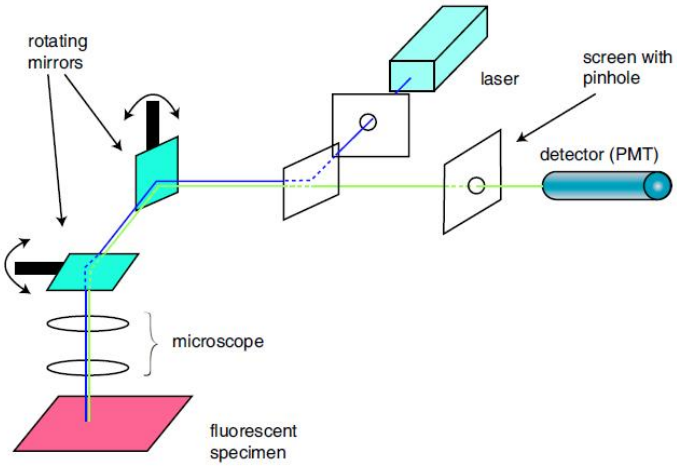

FIGURE 2.14: The schematic confocal microscopy.

The primary advantage of confocal microscopy is the ability to serially produce thin (0.5 to 1.5 μm) optical sections through fluorescent specimens that have a thickness ranging up to 50 μm or more [15]. The image series is collected by coordinating incremental changes in the microscope fine focus mechanism (using a stepper motor) with sequential image acquisition at each step. Image information is restricted to a well-defined plane, rather than being complicated by signals arising from remote locations in the specimen. Contrast and definition are dramatically improved due to the reduction in background fluorescence and improved signal-to-noise [15]. Furthermore, optical sectioning eliminates artifacts that occur during physical sectioning and fluorescent staining of tissue specimens for traditional forms of microscopy. The non-invasive confocal optical sectioning technique enables the examination of both living and fixed specimens under a variety of conditions with enhanced clarity.

Principle of confocal microscopy

The confocal microscope incorporates two principal ideas: point by point illumination of the sample and rejection of out of focus light [16–18]. One drawback with imaging a point onto the specimen is that there are fewer emitted photons to collect at any given instant. Thus, to avoid building a noisy image each point must be illuminated for a long time to collect enough light to make an accurate measurement [19]. In turn, this increases the length of time needed to create a point-by-point image. The solution is to use a light source of very high intensity, which Minsky did with a zirconium arc lamp. The modern choice is a laser light source, which has the additional benefit of being available in a wide range of wavelengths.

Fig. 9.7 shows the internal workings of a confocal microscope. The laser light (blue line) reflects off a dichroic mirror, which directs it to an assembly of vertically and horizontally scanning mirrors. The light then passes through the microscope objective and excites the fluorescent sample. The fluorescent light (green line) is descanned by the same mirrors that are used to scan the excitation light from the laser and then passes through the dichroic mirror. After that, the light is focused onto the pinhole which rejects all out-of-focus light arriving from the sample. The light that makes it through the pinhole is finally measured by a detector such as a photomultiplier tube.

In confocal microscopy, there is never a complete image of the specimen because at any instant only one point is observed. Thus, for visualization a computer reconstructs the 2D image plane one pixel at a time. For a 512 $\times$ 512-pixel image this is typically done at a frame rate of 0.1-30 Hz. As the laser scans over the plane of interest, a whole image is obtained pixel-by-pixel and line-by-line, whereas the brightness of a resulting image pixel corresponds to the relative intensity of detected light.

Applications

The broad range of applications available to laser scanning confocal microscopy includes a wide variety of studies in neuroanatomy and neurophysiology, as well as morphological studies of a wide spectrum of cells and tissues. In addition, the growing use of new fluorescent proteins is rapidly expanding the number of original research reports coupling these useful tools to modern microscopic investigations. Other applications include resonance energy transfer, stem cell research, photobleaching studies,

lifetime imaging, multiphoton microscopy, total internal reflection, DNA hybridization, membrane and ion probes, bioluminescent proteins, and epitope tagging [20, 21]. Moreover, confocal microscopy is clinically used in the evaluation of various eye diseases. It is particularly useful for imaging, qualitative analysis and quantitafication of endothelial cells of the cornea. Last but not the least, confocal microscopy is also used as the data retrieval mechanism in some 3D optical data storage systems.

2.2.5 Fluorescence lifetime imaging microscopy

The fluorescence of organic molecules is not only characterised by the emission spectrum, it has also a characteristic lifetime. Any energy transfer between an excited molecule and its environment in a predictable way changes the fluorescence lifetime. By detecting differences in lifetime, it is possible to distinguish even dyes having the same fluorescent color as well as to identify autofluorescence. Furthermore, high signal-to-noise images can be obtained by using a probe with very long lifetime compared to that of the fluorescent dyes normally used. Fluorescence lifetime imaging also makes it possible to obtain information on the molecules while observing a living cell. The factors affecting the fluorescence lifetime include ion intensity, hydrophobic properties, oxygen concentration, molecular binding, and molecular interaction by energy transfer when two proteins approach each other. Lifetime is, however, independent of dye concentration, photobleaching, light scattering and excitation light intensity. Therefore, fluorescence lifetime imaging allows us to perform accurate ion concentration measurement and FRET analysis. Fluorescence lifetime imaging microscopy (FLIM), a new fluorescence microscopy technology, has been widely explored by researchers around the world. It is a functional imaging methodology that is currently experiencing a rapid increase in uptake due to its excellent specificity and its relative insensitivity to intensity artifacts. FLIM entails determining the (average) fluorescence decay time for each pixel in a field of view and producing a map of fluorescence lifetime data. This technique is being applied to biological samples ranging from single cells to bulk tissue using both exogenous fluorophore labels, particularly genetically expressed labels such as green fluorescent protein, and endogenous fluorophores in biological tissue to provide intrinsic contrast. This section will gives several of the important aspects of FLIM.

Technology for FLIM

There are two methods of fluorescence lifetime imaging: the time-domain method and the frequency-domain method.

1. Time-correlated FLIM: In some cases of delay after excitation by a pulse laser, the fluorescence image can be obtained by the gate operation of the image intensifier. The lifetime is measured in nanoseconds by a laser with a pulse duration of a few hundred picoseconds and a nanosecond-level shutter because the lifetime of an excitation state is usually 1 to 20 nanoseconds. The fluorescence lifetime at each pixel can also be obtained by measuring while varying the delay time until a gate opens. Fluorescence lifetime images are shown in pseudocolor according to their lifetimes.

2. Frequency-domain FLIM: Synchronous detection is used to determine the phase difference and change in modulation depth between a sinusoidally modulated excitation laser signal and the resulting sinusoidally modulated fluorescence signal.The measurement may be taken either by laser scanning (photomultiplier) or using a charge-coupled device (CCD).

In principle the time and frequency approaches can provide equivalent information but in practice the choice of approach is impacted by the specific FLIM application. The frequency domain approach is sometimes considered to be simpler and cheaper since it is straightforward to sinusoidally modulate a c.w. laser for nanosecond measurements. When picosecond resolution is required, the necessary high frequency (GHz) electronics means that the cost and complexity of the frequency domain technology becomes comparable to that of the time domain. A further consideration is that biological systems often exhibit complex fluorescence decays that do not fit to a simple mono-exponential decay model. While double exponential decay profiles may be readily analysed in the frequency domain, more complex decay profiles may be more straightforward to analyse from direct time-domain measurements.

In our project, we use a photon counting technology of time-domain method called time-Correlated Single Photon Counting (TCSPC) [22–24]. The structure of SPC-830 TCSPC modules in the basic ′Scan Sync In′ imaging mode is shown in the Fig. 5.15. The modules employ an advanced three dmensional TCSPC technique featuring both

high count rate and low differential. It contains the usual building blocks (CFDs, TAC, ADC) in the ′reversed start-stop′ configuration together with a scanning interface and a large histogram memory integrated on one board.

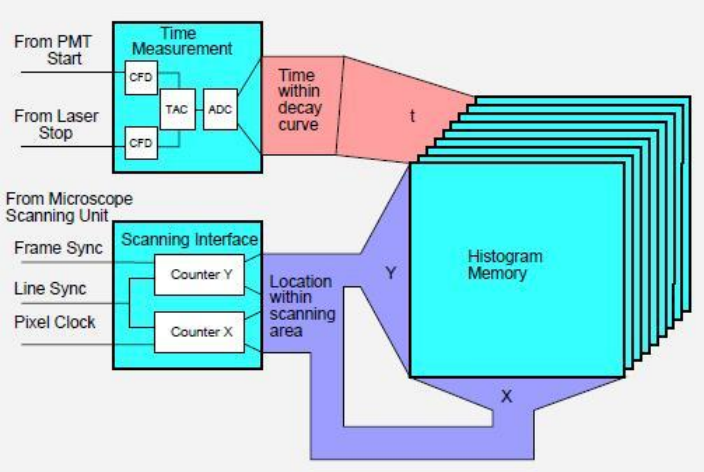

FIGURE 2.15: Basic principle of the SPC-830 TCSPC Imaging module.

The TCSPC module receives the single photon pulses from the photomultiplier (PMT) of the microscope, the reference pulses from the laser and the Frame Sync, Line Sync and Pixel Clock signals from the scanning unit of the microscope. For each PMT pulse, i.e. for each photon, the TCSPC module determines the time of the photon within the laser pulse sequence and the location within the scanning area. These values are used to address the histogram memory in which the events are accumulated. Thus, in the memory the distribution of the photon density over the scan coordinates, x, y, and the time, t, within the fluorescence decay function builds up. The result can be interpreted as a two-dimensional (x, y) array of fluorescence decay curves or as a sequence of fluorescence images for different times (t) after the excitation pulse.

Interestingly, there is practically no loss of photons in the TCSPC imaging process. As long as the photon detection rate is not too high all detected photons are processed and accumulated in the histogram, thus providing near-ideal signal-to-noise ratio and maximum sensitivity. This is a key advantage of TCSPC imaging compared to gated photon counting [25, 26], gated image intensifiers [27, 28] and modulation techniques [29–31]. A comparison of the efficiency of the different methods is given in [32].

Another benefit of TCSPC imaging is the high time resolution. The time channel width can be as small as 820 fs. Decay times down to a few picoseconds can be determined with fast detectors. On the other hand, TCSPC imaging is flexible in that a large number of pixels can be measured with wide time channels or precision measurements can be done at a small number of pixels. Furthermore, the method can work with the fastest scanning speed of the microscope thus avoiding heat concentration in the excited spot of the sample.

The whole FLIM systems we used in this project was shown in Fig. 5.16. The pulsed excitation is obtained either from the Ti:Sapphire laser of a multiphoton system or from a picosecond diode laser. The Ti:Sapphire laser is free-beam coupled to the SP2 scan head; the diode laser is coupled through a single-mode fibre. The wavelength of the Ti:Sapphire laser is tuneable from 710 nm to 890 nm, the wavelength of the diode laser is 405 nm. The standard detector is a PMC-100-0 of Becker Hickl. The PMH-100-0 detector delivers an instrument response function (IRF) of about 150 ps width. For each detected photon, the detector delivers a pulse of about 1.5 ns width and about 100 mV amplitude. These single-photon pulses are fed into a Becker Hickl SPC-830 TCSPC module. Using these signals, the SPC-830 modules builds up a photon distribution over the time of the photons in the laser period and the coordinates of the scan area. This detector of the FLIM system is protected by a shutter. The recording of FLIM data is based on concerted operation of the TCS SP2 microscope and the SPC-830 TCSPC module. Controlled by its LCS software, the TCS SP2 microscope scans the sample. The photons detected by the FLIM detector are processed in the TCSPC module,which is controlled by its SPCM software.

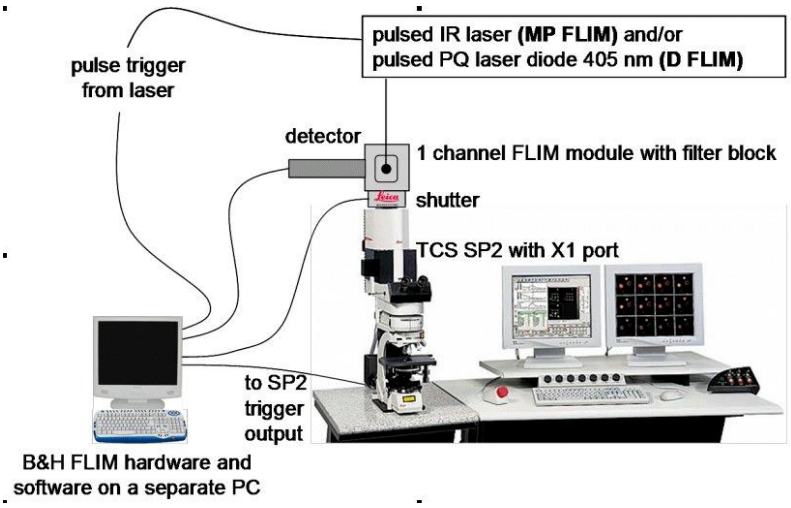

FIGURE 2.16: System configuration of the Leica FLIM systems.

3

Metal-enhanced Fluorescence and its Biological Application (review)

3.1 Introduction

One of the current fundamental challenges in fluorescence detection is to enhance the emission intensity of a fluorophore and lower the detection limit. In this regard, there has been a recent explosion in the use of metallic nanostructures to favorably modify the spectral properties of fluorophores and to alleviate some of their more classical photophysical constraints [33–36]. Such fluorophore-metal interactions is defined as metal-enhanced fluorescence (MEF). It is the interaction of the excited fluorophores with surface plasmon resonances in metals, and this effect is particularly prominent in metal nanostructures. Such structures can produce desirable effects such as increased quantum yields, decreased lifetimes, increased photostability, and potential for

improved energy transfer. However, at very close proximity the fluorescence quenching effect competes with all these favorable effects [6]. It has been demonstrated that fluorophore quenches within 5 nm from the surface of metallic particles. At further distances the enhancement starts to override the quenching and reaches its maximum at about 10 nm from the metal surface [34]. At larger metal-fluorophore separation the enhancement effect progressively declines.

MEF has a long scientific history starting with the classic reports of Drexhage [6], and has now become a leading technology to increase fluorescence detection sensitivity, especially in diagnostic setting, such as immunoassays. In the same period another surface-sensitive technique known as Surface-Enhanced Raman Scattering (SERS) has been established [7, 8]. SERS produces several orders of magnitude enhancement of the Raman scattering cross-section from molecules on rough metal surfaces. Although the two effects are related, the conditions in which they occur are very different. The optimal MEF signal occurs at a certain distance between fluorophores and the metal, owing to quenching of fluorescence via Förster energy transfer to the metal [1]. In particular, fluorophores in direct contact to the metal are typically completely quenched. In contrast, the SERS signal is maximally enhanced when molecules are immediately adjacent to the metal. Due to the interaction between metal nanostructures and fluorophores, the MEF technique has been shown to produce desirable effects such as increased fluorescence emission efficiency ('quantum yield') and improved photostability of fluorophores [2, 3]. In addition, MEF can significantly increase the efficiency of Förster resonance energy transfer (FRET) between two fluorophores, known as the donors and acceptors. This is significant for traditional FRET assays, where both the donors and the acceptors are prone to photodegradation, which decreases the measured FRET efficiency [9]. In this chapter, we begin with a brief overview of MEF, highlighting some current theoretical results, typical metal nanostructures used as MEF substrates and fluorescence-based biological applications of the MEF technique.

3.2 The principle of metal-induced fluorescence enhancement

Prior to focusing on the theory for metal-enhanced fluorescence, it is useful to review the optical properties of metal colloids and discontinuous films. Metal colloids have

been used for centuries to make coloured glass [37]. The origin of the colour as due to metallic colloids was first recognized by Faraday in 1857 [38]. The term plasmon indicates that the electrons are free to migrate in the metal in a manner similar to that of ions in gaseous plasma. Plasmons are important because they play a major role in determining the optical properties of metals. The frequency of the plasmon resonance can be estimated in the free electron model as:

$$\omega = \sqrt{\frac{ne^2}{m\varepsilon_0}} \tag{3.1}$$

where n is the valence electron density, e is the elementary charge, m is the electron mass and ε_0 the permittivity of free space.

The properties of plasmons depend on the geometry of metal. One of the most important special cases is the interface of metal and vacuum. In this situation the long wavelength absorption is called the surface plasmon absorption, which is due to electron oscillations on the metal surface. Fig. 6.1 shows surface plasmons on a flat metal surface by illumination of the metal surface with p-polarized light. However, they are induced by incident light only under special optical conditions. In addition, surface plasmons are also created by direct illumination of metal colloids (see Fig. 6.2), resulting in rapid osillation of the spatially bound electrons [39]. Unlike planar metal surfaces, no special conditions are required to observe the surface plasmon absorption in colloids.

These surface plasmons are thus characterized by a distinctive absorption spectrum with specific feature in the visible spectrum which is affected by the shape, size, composition and dielectric environment of the particles as well as the direction of the exciting light [41–43].

Now we focus on the interactions between fluorophores and metallic surfaces. The fluorophores dissolved in a nearly homogeneous solution emit into free space and are observed in the far field. Near-field effects are usually very difficult to observe because of the small size of fluorophores relative to the experimental chamber. However, the nearby metal nanostructures can alter the ′free space′ condition of fluorophores and this effect is most pronounced in a specific distance range distance between fluorophores

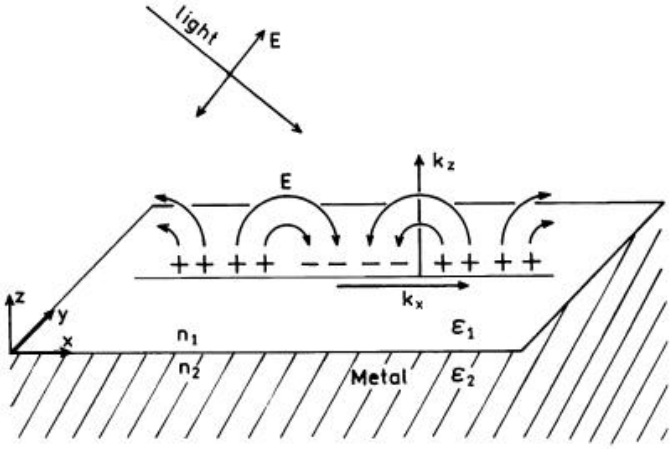

Figure 3.1: Schematic of surface plasmons on a metal surface. Adapted from [40]

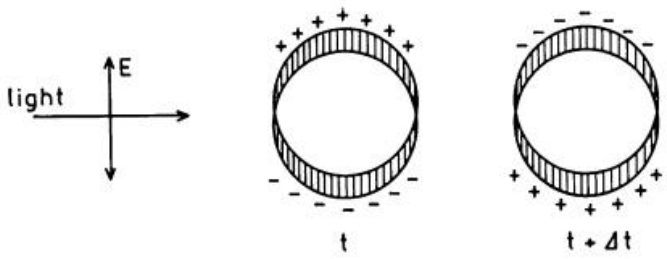

Figure 3.2: Surface plasmon oscillation in a metallic colloid. Adapted from [39]

and metal nanostructures. Under these conditions the radiative rate of the fluorophore is modified (see Fig. 6.3).

The presence of metal nanostructures can affect the optical properties of nearby fluorophores. Metal nanostructures are able to produce an increase in local electromagnetic field and this leads to an increased excitation rate of fluorophores. The modified density of electromagnetic field modes additionally produces increase of the radiative decay rate of fluorophores. The latter effect is moderated by the enhanced nonradiative energy transfer to the metal. The local electromagnetic field enhancement produces a higher excitation rate but it does not change the lifetime of the fluorophore. This effect is referred to as excitation enhancement (E_{ex}). The second effect is referred to as emission enhancement (E_{em}), increasing the quantum yield and reducing the lifetime of the fluorophore. If the fluorophore is in free space, its lifetime (τ) is usually

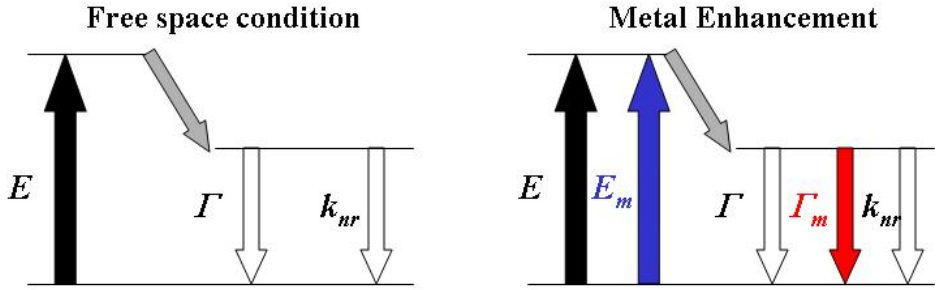

FIGURE 3.3: Classical Jablonski diagram: E_m is metal enhanced excitation rate, Γ_m is radiative rate in the presence of metal, k_{nr} is nonradiative decay rate of fluorophores. The weak effect of metals on k_{nr} is ignored.

given by [1]

$$\tau = \frac{1}{\Gamma + k_{nr}} \tag{3.2}$$

where Γ and k_{nr} are the radiative and nonradiative decay rates, respectively. The radiative decay rate Γ is an intrinsic property of a fluorophore. The fluorescence quantum yield (Q) is given by

$$Q = \frac{\Gamma}{\Gamma + k_{nr}} \tag{3.3}$$

Assume the presence of a nearby metal (m) surface increases the radiative rate by addition of a new rate Γ_m(Fig. 6.3, right part). In this case the lifetime τ_m and quantum yield Q_m of the fluorophore near the metal surface are given by [1]:

$$\tau_m = \frac{1}{\Gamma + \Gamma_m + k_{nr}} \tag{3.4}$$

$$Q_m = \frac{\Gamma + \Gamma_m}{\Gamma + \Gamma_m + k_{nr}} \tag{3.5}$$

These equations result in unusual predictions for a fluorophore near a metal surface. As the value of Γ_m increases, the quantum yield increases while the lifetime decreases. The most dramatic relative changes are found for fluorophores with the lowest quantum yields.

If the dye has a high quantum yield ($Q_0 \to 1$), then the additional radiative decay rate cannot substantially increase the quantum yield. In this case energy transfer

quenching to the metal will dominate [35], resulting in the fluorescence quenching. While in the case of the low Q, such as 0.1, the metal-induced rate Γ_m increases the quantum yield. At sufficiently high values of Γ_m, the quantum yields of all fluorophores approach 1.0. In addition, the larger values of Γ_m/Γ are required to change the lifetime or quantum yield of low quantum yield fluorophores. This effect occurs because, for the same unquenched lifetime τ_0, lower quantum yields imply larger values of k_{nr}. Larger values of Γ_m are required to compete with the larger values of k_{nr}. This suggests that the emission from weakly fluorescent substances can be increased if they are positioned at an appropriate distance from a metal surface or colloid.

Now we disscuss three effects induced by metal surface nearby: quenching at short distance, an increase in the excitation field, and an increase in the radiative decay rate. These effects are highly dependent on distance and the geometry of the metal close to a fluorophore. At short fluorophore-metal distances the fluorophores are quenched. At proper distances near 5-20 nm the radiative rates are increased. In addition to increased radiative rates, the fluorophores can also be exposed to higher local fields due to interactions between the metal and the incident light (see Fig. 6.4)[34].

Firstly we consider the effects of quenching when the fluorophores are close to the surface (<5 nm) (Fig. 6.4 solid line, top left). Assuming there is no change in the emission rate (Γ_m), the intensity of the fluorophores will be decreased near the surface (Fig. 6.4, top left). However, it is known such quenching results in increased photostability because the molecules spend less time in the excited state and thus have fewer opportunities for photochemical reactions [44]. Increased photostability has also been observed on metal-island films [45]. Since the lifetime of the fluorophores will be decreased (Fig. 6.4, top center), quenching by the surface is expected to result in increased stability and an increase in the number of excitation-deexcitation cycles prior to photodecomposition. While the quantum yield is reduced, the number of detected photons or detectability is expected to be about the same, as can be seen from the integrated area for continuous illumination (Fig. 6.4, upper right).

Now we consider the effect of a metal-induced concentrations of the incident field felt by the fluorophore at the same illumination intensity (Fig. 6.4, middle panel). This

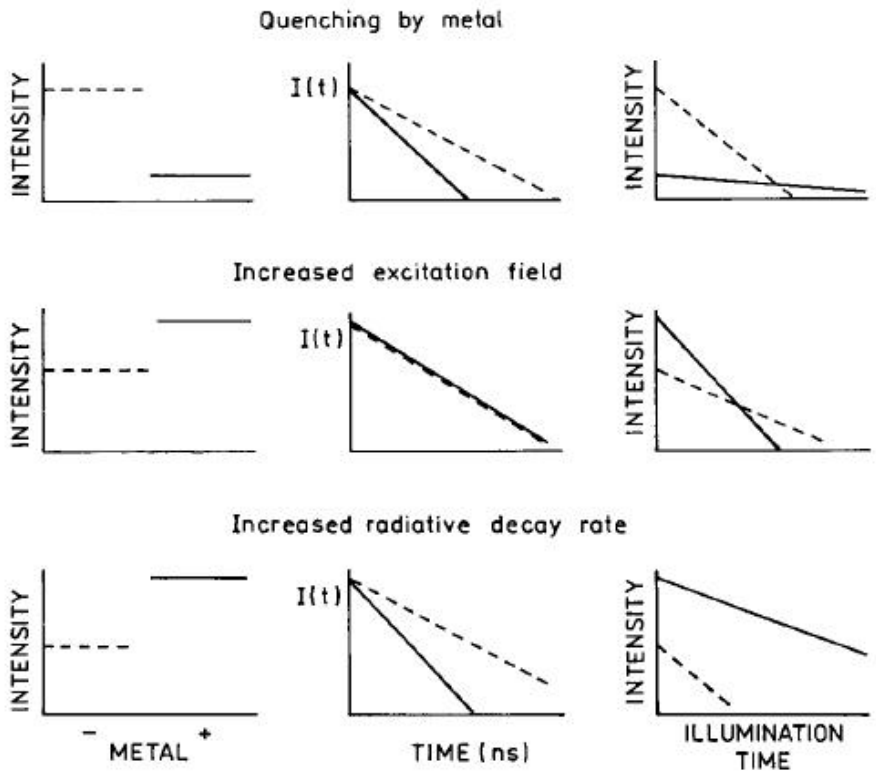

FIGURE 3.4: Effects of metals on the steady-state intensity, intensity decay, and photobleaching of a nearby fluorophore. From top to bottom the panels show quenching by the metal, the effect of an increased excitation field, and the effects of an increased radiative decay rate. The dashed lines indicate the absence of metal and the solid line indicates the presence of metal, adopted from [34].

effect will result in an increased intensity when compared to the no-metal sample, both observed with the same incident intensity. The intensity will be higher for the same incident intensity (Fig. 6.4, middle right). However, the excited molecules will have the same radiative decay rate Γ and Γ_m. The lifetimes will remain the same. Since there is no quenching, we expect the same overall numbers of emitted photons until the fluorophore is destroyed, as seen from the integrated area with continuous illumination (middle right).

The lower panels in Fig. 6.4 illustrate the effect of an increased radiative rate. In contrast to the previous two effects, an increase in the radiative decay rate is expected to result in dramatic increases in the number of photons observed from each fluorophore. An increase in the radiative rate will result in an increased intensity due

to the increased quantum yield (Fig. 6.4, bottom). The lifetime will be shortened by the metal-induced increase in the radiative rate. Since the fluorophore will spend less time in the excited state for each cycle, the extent of photobleaching is expected to decrease. The combination of increased quantum yield and decreased photobleaching should result in a substantially increased number of detected photons per fluorophore when the radiative rate is increased (lower right).

To sum up, nearby metal surfaces can increase radiative decay rates, increase quantum yields, decrease lifetimes, and increased photostability. These effects can be used in the biochemical and medical applications of fluorescence. However, such successful application will require considerable efforts in nanoscale fabrication, surface coating, and coupling of fluorophores and macromolecules to the surfaces. Therefore, we will subsequently showcase a brief snapshot on different metal substrates employed in MEF so far.

3.3 Methodologies for the preparation of MEF substrates

In the previous section we established that metal nanostructures can adjust the optical properties of fluorophores, inducing enhanced fluorescence. However the manner in which this is accomplished depends sensitively on fine details of nanostructure morphology, the type of metal used and the relationship between surface plasmon resonance in the metal and the properties of the fluorophore. Furthermore the practical application of a particular type of nanostructure, for example in a specific bioassay may depend not only on the combination of physical properties such as those listed above, but also on engineering issues such as uniformity of nanostructure coverage over macroscopic area, geometry of that area, chemical stability, as well as manufacturing cost. These issues are addressed in the studies focusing on MEF substrates and the present section provides a brief overview.

Silver nanostructures are an important class of MEF substrates. Different silver nanomorphologies have been reported and employed in MEF, among those silver island films (SiFs) was most frequently used so far. In a typical SiF preparation [46], silver salt is reduced to silver, which is then randomly deposited on the glass surface, upon the sequential addition of sodium hydroxide, ammonium hydroxide, and D-glucose

solutions. This preparation method results in a relatively wide distribution of metal particle sizes, raning from 30 to 80 nm, and displays the plasmon extinctionmaximum near 430 nm [46]. The SiF substrates have been reported to produce the enhancement factors of about 5 and 7 for Cy3-DNA, and Cy5-DNA respectively [46]. The main drawbacks of SiFs as substrates for fluorescence amplification are poor reproducibility and lack of spatial homogeneity leading to undesirable variations in the enhancement factor.

Other silver nanoscale morphologies, including silver colloids [2, 4], silver nanorods [5], silver triangles [47] and silver fractal-like nanostructures [3], were also investigated in the context of MEF. The synthesis of silver colloids involves simply boiling a solution of silver nitrate in the presence of a weak reducing agent, such as sodium citrate. The as-prepared silver colloids usually comprise large, inhomogeneous, spherical particles. They can be chemically bound with biomaterials labelled by fluorophores, such as, for example, cyanine (Cy5)-labeled single-stranded oligonucleotides. In this case, single-molecule fluorescence was reported to be enhanced by 7 times on the silver colloid monomer and 13 times on the silver colloid dimer relative to the free Cy5-labeled oligonucleotide in the absence of silver colloids [48]. For preparation of anisotropic silver nanoparticles, such as nanorods, they are usually deposited directly on the glass slide using the seed-mediated cetyltrimethylammonium (CTAB) directed growth. The application of such silver nanorods in metal-induced fluorescence enhancement shows that 50-fold increase in fluorescence intensity for indocyanine (ICG) conjugated human serum albumin (HSA) monolayers [49]. Silver fractal-like nanostructures deposited on the glass surface have also shown strong fluorescence enhancement [50]. In that study, silver foil electrodes were placed in deionised water about 10 mm apart and a constant current was applied. When such silver fractal-like nanostructures were used in MEF, an over 1000-fold increase in fluorescence signal was obtained for Fluorescein isothiocyanate (FITC) conjugated HSA monolayers [50]. All of these recent silver nanostructure preparations have resulted in attractive silvered surfaces for MEF applications.

Apart from silver, other metal nanostructures were also employed as MEF substrates such as gold [51, 52] and aluminum [53]. In preparation of aluminum film, aluminum was deposited on quartz slides using a vacuum evaporation chamber under high vacuum. The deposition rate was adjusted by the filament current and the thickness of film was measured with a quartz crystal microbalance. The experimental results [53] show that such aluminum films can significantly enhance the emission intensity and photostability of a layer of PVA film containing separately neutral derivatives of tryptophan (NATA) and tyrosine (NATAtyr). Aluminum consistently shows higher enhancements than silver in the 300-350 nm range, which is relevant for protein (and most other biomolecule) fluorescence. This predicts that aluminum is a more efficient metal than silver for use in MEF applications in the ultraviolet.

3.4 Applications of metal-enhanced fluorescence to biotechnology

3.4.1 Metal-enhanced fluorescent probes

Fluorophores were essential in fluorescence-based technologies such as immunoassay or for the immunostaining of biological specimens with the specific antibodies. In these applications, fluorescein is one of the most widely used probes [54]. An unfortunate property of fluorescein is self-quenching, which results from Förster resonance energy transfer between nearby fluorescein molecules. As a result, the intensity of a labled protein does not increase with increased extents of labeling, but actually decreases [55]. It has been reported that self-quenching can be largely eliminated by the close proximity to Ag nanostructures nearby. Lakowicz et al examined changes in fluorescence from FITC-HSA conjugates on the SiFs [55]. The dramatic difference in the intensity of heavily labeled HSA on glass and on SiFs was observed: an almost invisible signal on quartz and a very bright image on the SiFs. It was found that most of the self-quenching can be partially eliminated by proximity of the labeled protein to metallic silver particles. These results show silver particles or colloids, when bound to protein heavily labeled with fluorophores, can provide significantly higher intensities due to a decrease in the content of self-quenching.

In addition, our group also demonstrated the change in the fluorescence intensity of FITC-HSA by employing the homogeneous silvered nanostructures on the glass surfaces

[56]. The fluorescence enhancement was investigated by using a monolayer of FITC-HSA on the glass slide with and without silver nanostructures, respectively. A 13-fold increase in fluorescence intensity was obtained when FITC-HSA conjugates was on the surface of sliver nanostructures with a size of about 47 nm (see Fig. 6.5), suggesting that this system can be employed in many areas of life sciences and biotechnology such as imaging and sensing applications based on enhanced fluorescence detection.

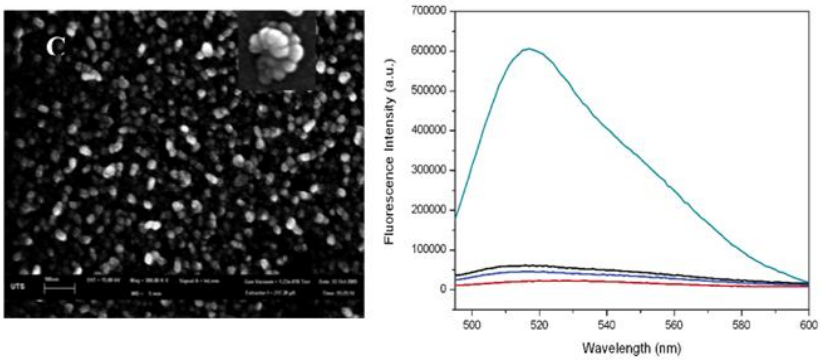

FIGURE 3.5: (Left) silver nanostructures with a size of 47 nm on the glass slide. Inserts show the morphology of individual particles. (Right) Fluorescence emission intensity of FITC-HSA (from top to bottom): on the surface of silver nanostructures with a size of 47 nm; on the surface of silver nanostructures with a size of 19 nm; on the clean glass surface without silver nanostructures; on the surface of gold colloid monolayer, adopted from [56].

Similarly, Geddes reported the effects of Ag colloids on the fluorescence spectral properties of indocyanine green (ICG), which is a dye widely used for in vivo medical testing [57]. The colloid-coated surfaces were found to cause a 30-fold increase in the intensity of ICG, which was held close to the metal surface by adsorbed albumin. The increased intensities of ICG were also associated with decreased lifetimes and increased photostability, which are indicative of modifying the fluorophores radiative decay rate. These results suggest the use of metal colloid-enhanced ICG for applications to retinal angiography and vascular imaging and as a contrast agent for optical tomography.

Moreover, there were also reports of the effects of silver particles on metal-ligand complexes, which are deemed to be useful as luminescence probes in biochemistry owing to their long luminescent decay times [58]. The emission spectral properties of $[Ru(bpy)_3]^{2+}$ on SiFs and glass yielded several fold higher intensities on SiFs, accompanied by shortened lifetimes. These results are consistent with an approximate 20-fold

increase in radiative decay rate of the $[Ru(bpy)_3]^{2+}$ in close proximity to silver particles.

3.4.2 Fluorescent immunoassays based on the MEF

MEF has also been utilized in the improved detection sensitivity in the immunoassay. Lakowicz et al [59] present an immunoassay platform that uses enhanced total internal reflection fluorescence in the proximity of SiFs. This platform is used with a model immunoassay where a protein antigen, rabbit immunoglobulin G, was immobilized on the SiF-coated glass surface (see Fig. 6.6). The signal from a fluorescent dye labeled anti-rabbit antibody binding to the surface antigen was detected. In this study, different color dyes have been tested. A 40-fold increase in fluorescence emission was observed from the fluorophore-labeled antibody on the SiFs compared to that on the glass slide alone.

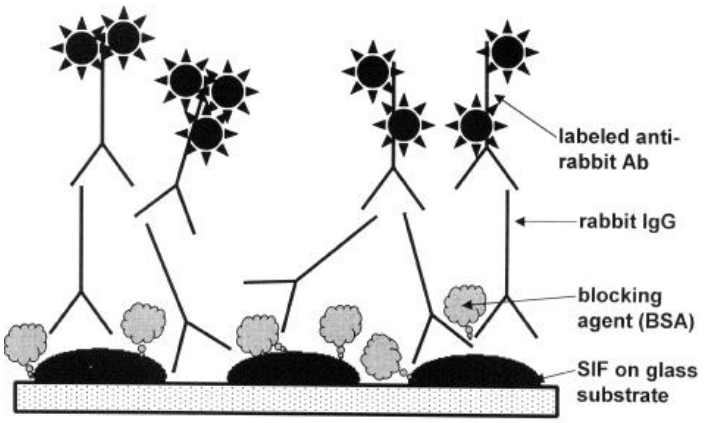

Figure 3.6: Scheme of the model immunoassay, adopted from [59].

Matveeva et al also present fluoroimmunoassays on plain metal-coated surfaces (metal mirrors) enhanced by SiFs [60]. Metal mirrors (aluminum, gold, or silver protected with a thin silica layer) were coated with SiFs, and an immunoassay (model assay for rabbit immunoglobulin G or myoglobin immunoassay) was performed on this surface using fluorescently labeled antibodies(see Fig. 6.7). The results showed that SiFs alone (on glass surface not coated with metal) enhance the immunoassay signal approximately 3- to 10-fold. Using a metal mirror instead of glass as support for SIFs results in up to 50-fold signal enhancement(see Fig. 6.8).

In addition to using SiFs as substrates in enhanced fluorescence immmunoassay,

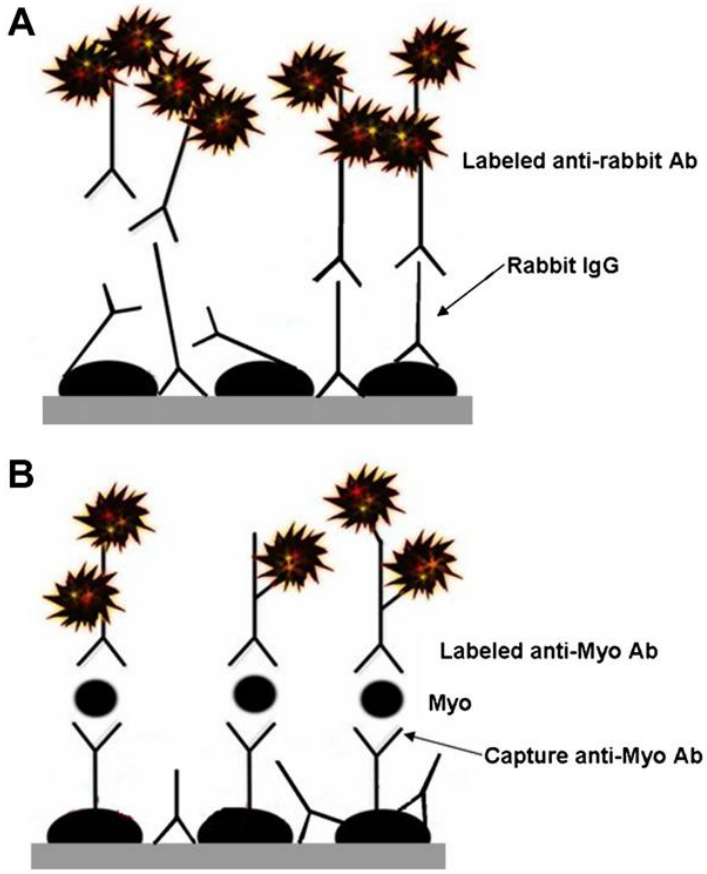

FIGURE 3.7: Scheme of the model immunoassay (A) and myoglobin (sandwich-format) immunoassay (B) on the SiF-modified slide surface. Ab, antibody, adopted from [60].

the silver film generated by vapor deposition method was also utilized [61]. In this study, The morphology of the silver film was controlled through the thickness of the film. A silica layer was coated on the silver film to protect the film and separate the fluorophore from the metal surface. Rabbit immunoglobulin G (IgG) was adsorbed on the silica by physiosorption and then dye labeled anti-rabbit IgG was bound to the immobilized rabbit IgG. It was observed that the fluorophore was quenched on a thin silver film (2 nm), enhanced on a thick film (>5 nm), and reached saturation (ca. 10 times enhancement) at 20 nm (see Fig. 6.9a). The MEF was also dependent on the thickness of the silica. The maximum enhancement occurred at a 10 nm thickness of silica and became very weak at 50 nm (see Fig. 6.9b). The lifetime was shortest at a 10 nm thickness of silica, became longer with increasing the thickness of silica, and was close to that on the glass substrate at 50 nm. Moreover, dependence of the MEF on

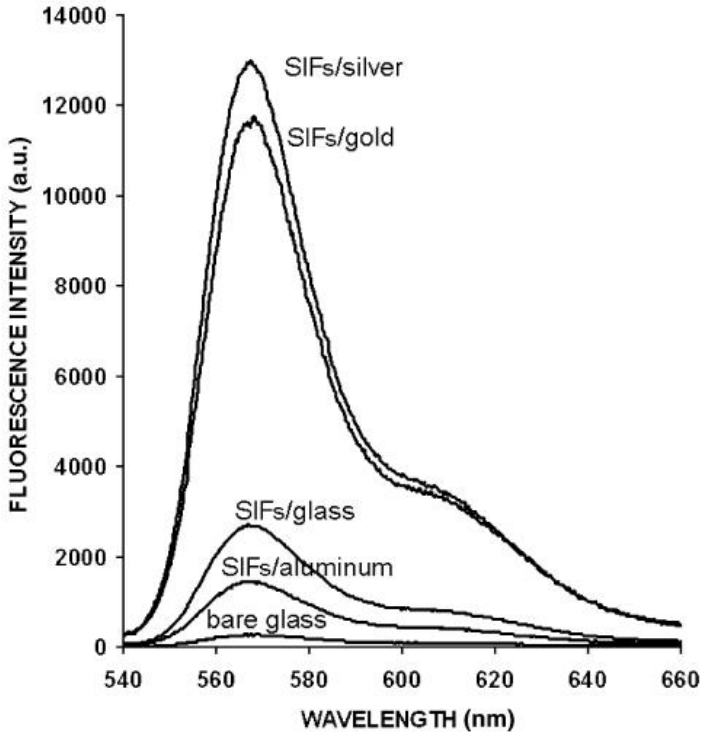

Figure 3.8: Fluorescence spectra of the labeled (AlexaFluor 55) anti-rabbit antibodies bound to the antigen immobilized on various slide supports used for immunoassay: glass only, SiFs on aluminum mirror, SiFs on bare glass, SiFs on gold mirror, and SiFs on silver mirror, adopted from [60].

the emission wavelength was also studied using different dye-labeled anti-rabbit IgGs to the immobilized IgG, showing that the fluorescence in the near-IR region could be enhanced more efficiently than that in the visible region for the fluoroimmunoassay analysis (see Fig. 6.9c).

3.4.3 DNA-based Technologies using MEF

DNA capture assays are the basis of a wide range of biotechnology and diagnostics applications [62] and are routinely used in gene chips [63], during PCR [64–66] and fluorescence-base in situ hybridization [66]. In most cases, the DNA capture assays are required to be highly sensitive, specific and fast whenever possible. The sensitivity of the fluorescence-based DNA hybridization assays is affected by multiple factors, which include unwanted background emission and the photostability of the fluorescent probe used. Moreover, DNA capture assays are often kinetically slow, requiring long incubation times. Therefore, there is a clear need for the development of more sensitive

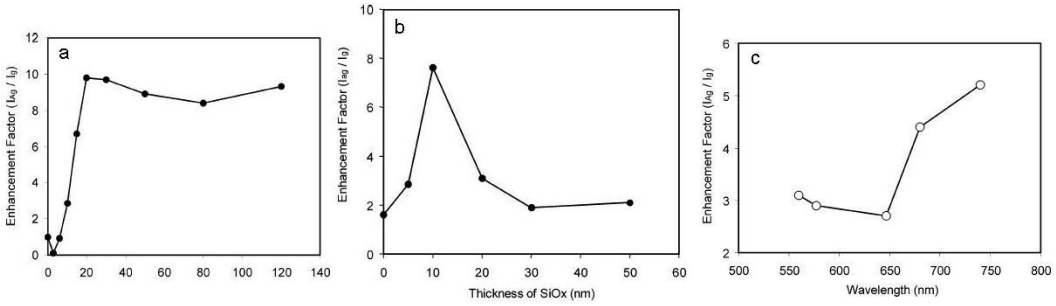

FIGURE 3.9: (a) Dependence of the enhancement factor on the thickness of silver film coated by a 5 nm thickness of silica upon excitation at 514 nm; (b)Dependence of the enhancement factor on the thickness of silica coated on a 10 nm thickness of silver film; (c)Dependence of the enhancement factor on the emission wavelength of a fluorophore-labeled antibody on a 10 nm thickness of a silver film coated by a 5 nm thickness of silica, adopted from [61].

and faster detection methods for more efficient DNA capture assays.

Recently, there are some reports on improving the sensitivity of DNA hybridization and sensing by using MEF [67–70]. Sabanayagam et al [70] employed MEF to measure two dyes commonly used in DNA microarrays, Cy3 and Cy5. A 4-fold signal enhancement for Cy3 and 28-fold for Cy5 were obtained compared to avidin-coated glass substrates. Hybridization of singly-labeled oligonucleotides to arrayed single-stranded probes showed lower maximal MEF factors of 10-fold for Cy5 and 2.5-fold for Cy3, because of the smaller amount of immobilized fluorophores as a result of reduced surface hybridization efficiencies. Fig. 6.10 shows the format of DNA hibridization in solution versus on a surface. MEF on SiFs was evaluated using a biotinylated 23 bp double-stranded DNA singly-labeled with Cy3 or Cy5. For the solution hybridization, biotinylated probe oligonucleotides $'b'$ and fluorophore-labeled target oligonucleotides $'F'$ are mixed to form fluorescently-labeled double-strand DNA at 85^oC. After cooling to room temperature, the DNAs are arrayed onto avidin-coated microscope slides. For the surface hybridization, biotinylated probe oligonucleotides are arrayed onto avidin-coated microscope slides. Fluorophore-labeled target oligonucleotides are deposited onto the array surface for hybridization at 45^oC. They also shows the difference in MEF when comparing Cy3 and Cy5. The larger enhancement for Cy5 may occur because the scattering component of the extinction spectrum is stronger for the far red Cy5 emission (see Fig. 6.11).

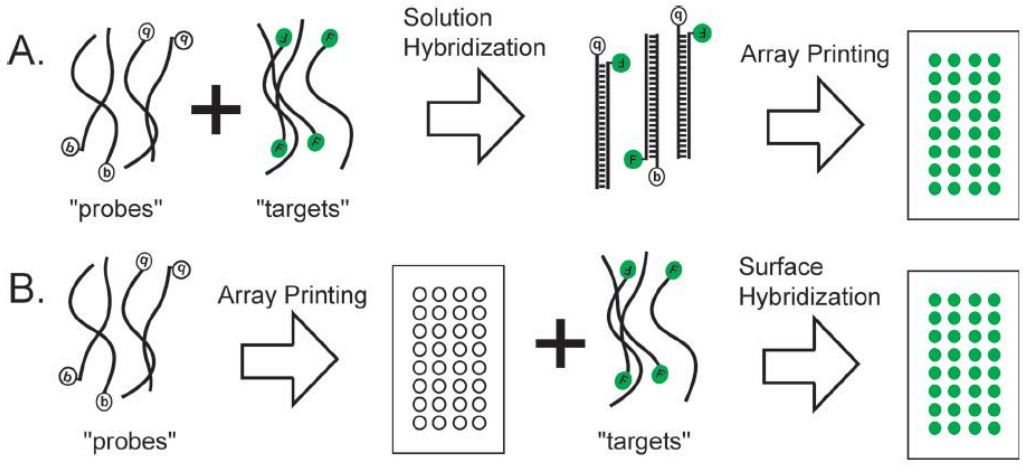

Figure 3.10: Scheme showing DNA hybridization in solution versus on a surface. (A) Solution hybridization; (B) Surface hybridization, adopted from [70].

3.4.4 Metal-enhanced fluorescence imaging

Molecularly specific fluorescent imaging of cells is expanding very rapidly with improved access to fluorescence microscopes, easy availability of a large number of fluorescent probes and most importantly the capability for genetic targeting. This imaging technology is critically required to identify cellular pathways and disease diagnostics at the molecular level [71, 72]. However, these organic fluorophores often display emission signals of low intensity relative to the background from the autofluorescence of cell lines [73]. Thus, it is difficult to separate the emission signals by the labeled targets from the whole cell images. Therefore metal-enhanced fluorophores were used instead of regular organic ones as the molecular agents in cell imaging [74–77]. Zhang used SiFs as the support to detect the fluorescence images of the labeled cell lines. The fluorescence signals by the fluorophores bound on the cell membranes were enhanced significantly by SiF supports as compared with those on the glass (see Fig. 6.12). In addition to the increase in the intensity, there was a dramatic shortening of the emission lifetime. In contrast to the Alexa Fluor 680 fluorophores on the membranes, the YOYO fluorophores (YOYO, a blue light-excited fluorescent dye) intercalated in the cell nuclei were not influenced significantly by the silver islands (see Fig. 6.13). This result can be interpreted by an effect of the distance on coupling between the fluorophores and metal particles: the fluorophores on the cell membranes are localized within, but the

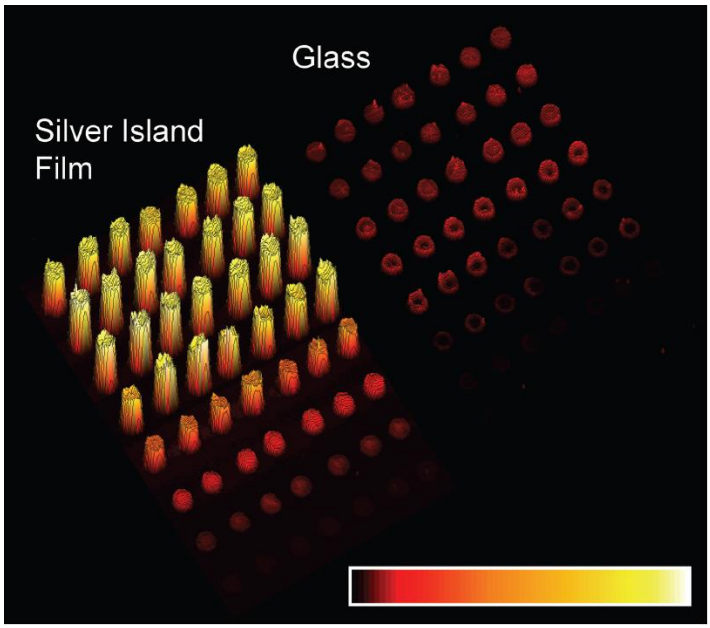

FIGURE 3.11: Fluorescence image of labeled oligonucleotide targets hybridized to MEF and glass DNA arrays. Probe oligonucleotides (23 mer) were arrayed onto the substrates at different spotting concentrations: each row represents seven replicate spots at a given concentration; the rows are 2-fold serial dilutions starting with 50 mM (upper row). The image shows the Cy5 fluorescence as a result of co-hybridization with complementary Cy5- and Cy3-labeled targets (23 mer), adopted from [70].

fluorophores in the cell nuclei are beyond the region of metal-enhanced fluorescence.

3.4.4 Metal-enhanced solution assay

Nearly all of the work pertaining to MEF to date, has dealt with fluorophores in close proximity to planar surfaces. However, it might also be desirable to use metals as colloidal suspensions for medical imaging, as they are potentially injectable and silver and gold colloids are already widely used in medicine. For example, such approaches are used in retinal angiography and could benefit from an enhanced indocyanine green and fluorescein quantum yield and from increased photostability [57].

In 2004, Geddes group made the first attempt to utilize silver nanoparticles in a solution-based enhanced fluorescence sensing platform [78], where we typically observed a 3-5 fold enhancemen in fluorescence from the biotinylated silver core-silica shell nanoparticles and by their aggregation with Cy3-labeled streptavidin in suspension. The thrust of that study was geared towards fluorescence-based aggregation assays, where the aggregating silver nanoparticles resulted in enhanced fluorescence

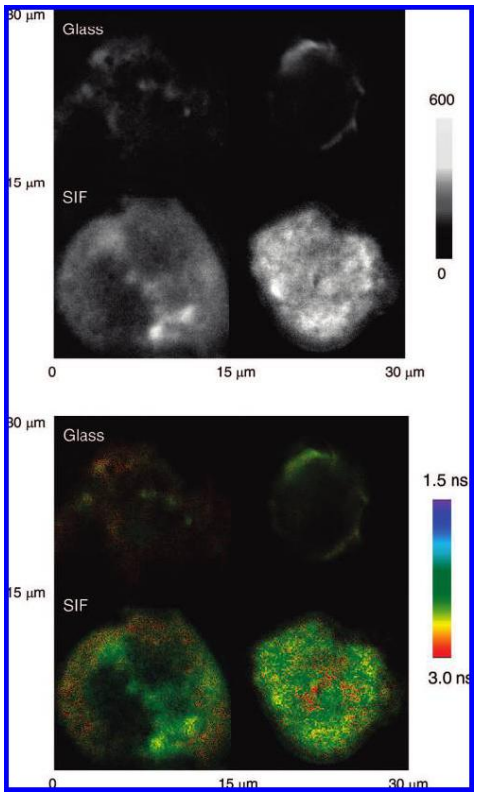

Figure 3.12: Upper panel: Representative emission intensity images of PM1 cells labeled with Alexa Fluor 680-dextran conjugates adhered to the cell membranes on a glass coverslip and on SiFs. Lower panel: Corresponding lifetime images of the intensity images in the upper panel, adopted from [77].

emission due to enhanced electric fields between the nanoparticles. Later, the same group developed the new monodisperse core-shell (silver core-silica shell) nanoparticles with various shell thicknesses featuring a fluorophore, named MEF nanoballs [79]. MEF nanoballs consist of a ≈130 nm silver nanoparticle core, a silica shell with up to 35 nm thickness and fluorophores doped within the silica shell (see Fig. 6.14). A model near infrared fluorophore, Rhodamine 800 (Rh800), was embedded into the shell to show the possible utility for cellular imaging. The emission intensity from the MEF nanoballs was ≈20-fold larger than that of the nanobubbles, where the silver core was removed from the MEF nanoballs by chemical etching (see Fig. 6.15). It needs to be emphasized that these core-shell nanocomposites can be further functionalized with ease, and this facilitates their utilization in bioassays and bioimaging with strong emission signals. These results demonstrated the flexibility of formats the MEF substrates

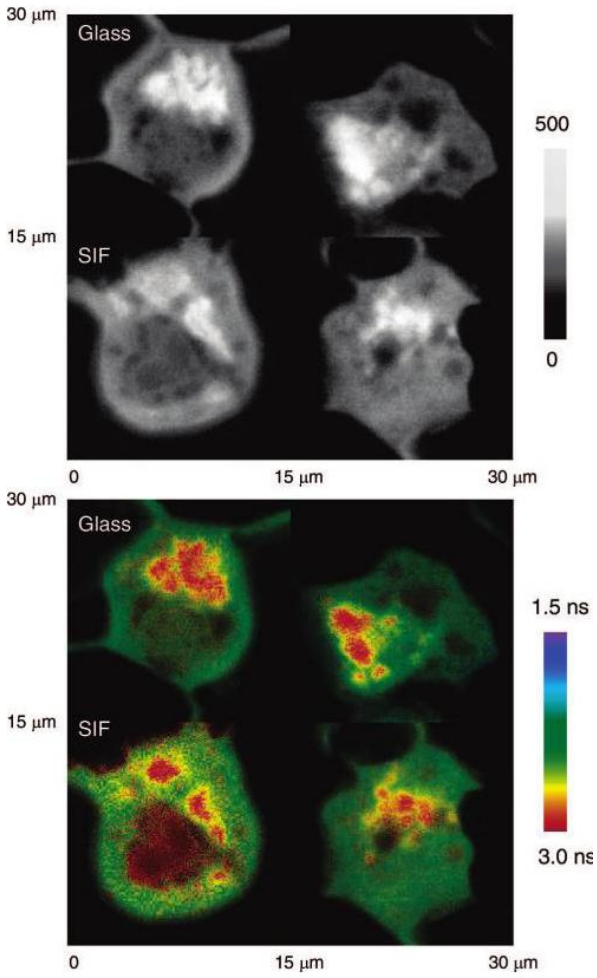

FIGURE 3.13: Upper panel: Representative emission intensity images of PM1 cells labeled with YOYO bound in the cell nucleus on a glass coverslip and on SiFs. Lower panel: Corresponding lifetime images of the intensity images in the upper panel, adopted from [77].

could take, which is important for their potential applications in a variety of biological settings.

In addition, other groups also present this metal-enhanced solution-based platform using another method [80]. In this method, oligonucleotide-modified silver particles and a fluorophore-labeled complementary oligonucleotide were employed (see Fig. 6.16). An increased emission from the fluorophore-labeled complementary oligonucleotide after hybridization in the presence of silver particles has been observed. They also provided some fundamental facts about displacement of oligonucleotide on the organic monolayer-protected silver particle, hybridization of complementary oligonucleotide on the oligonucleotide-displaced particle, and fluorescence enhancement with aggregation

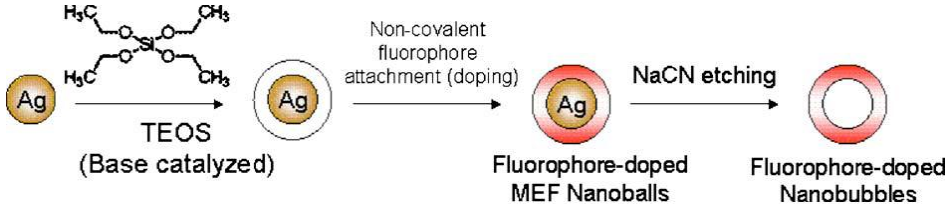

Figure 3.14: Schematic for the preparation of fluorescent core-shell $Ag@SiO_2$ (MEF) nanoballs and fluorescent nanobubbles, adopted from [79].

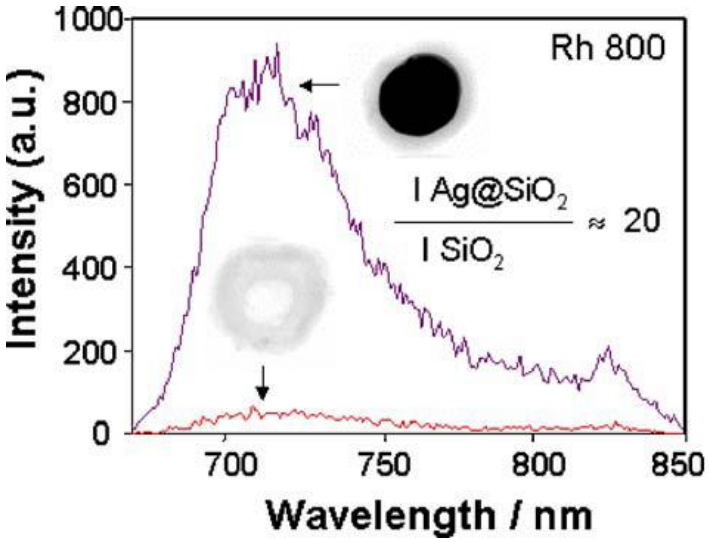

Figure 3.15: Fluorescence emission spectrum of Rh800-doped MEF nanoballs and from the corresponding fluorescent nanobubbles (control sample, cyanide etched), Rh800-doped nanobubbles, adopted from [79].

of the oligonucleotide-displaced or hybridized particle in KCl buffer solution. This result suggests the possible application of surface-enhanced fluorescence from metallic nanoparticle aggregation for DNA detection.

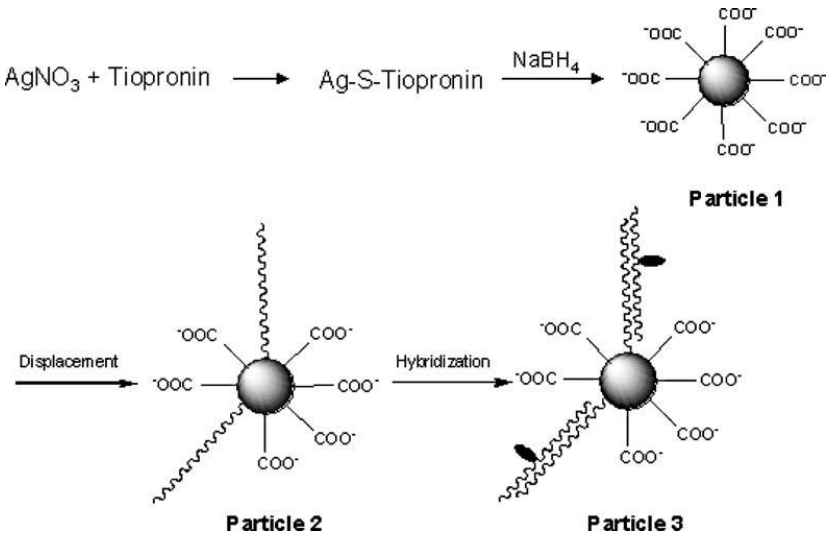

FIGURE 3.16: Preparation, displacement by thiolate oligonucleotides, and hybridization with fluorescein-labeled complementary oligonucleotides of tiopronin-monolayer protected silver nanoparticle, adopted from [80].

4

Enhanced Flow Cytometry-Based Bead Immunoassays Using Metal Nanostructures

Introduction

Bead-based technologies have widespread applications across a whole spectrum of chemical and biological sciences. Among those, bead assays, also known as suspension arrays play a prominent role [81–88]. Suspension arrays are ensembles of specially coated microspheres that are mixed with a sample such as patients′ blood or some other complex, biological fluid. The coating on the microspheres is then allowed to react with the target molecules or cells. Combining chemically-specific binding with the fluorescent label makes it possible to identify molecular species. Once the reaction has occurred, the microspheres are analyzed, one by one by using flow cytometry, or by other techniques. Such assays offer significant advantages over alternative planar

microarrays including rapid assay times and readout, extremely small sample volumes, and compatibility with high dilution [89, 90]. They are also able to read multiple components of a complex mixture at once (multiplexing) by using optically encoded microspheres with unique combinations of fluorescent dyes. These exceptional features and the fact that they are amenable to combinatorial chemistry approaches have been recognized by the industry with recently introduced technologies such as Luminex [91], or UltraPlex MicrosphereChip arrays from Illumina and Bioarray Solutions [92].

The bead assay technology has not yet reached its full potential, and one of the outstanding challenges is their limited detection sensitivity. However, as we show in this paper, it is possible to endow the microspheres with the capacity to amplify the analyte fluorescence (whether it is labeled or shows intrinsic fluorescence). Moreover, this can be done in a way compatible with flow cytometry detection.

Our approach is based on the application of metal amplification of fluorescence [2–5, 51, 59]. This effect is due to interactions of the excited fluorophores with surface plasmon resonances in metals, and it is particularly prominent in metal nanostructures. These have been shown to produce desirable effects such as increased quantum yields of fluorophores, their decreased lifetimes, increased photostability, and potential for improved energy transfer [51]. Owing to these advantages there has been a significant interest in using surface-based enhanced fluorescence immunoassays, either based on simple binding of labeled antigens or a sandwich format where secondary antibodies (Abs) have been labeled [51, 59, 93, 94]. However, up to now flow cytometry-based immunoassays on beads with surface-enhancing properties have not been demonstrated.

This work describes the preparation of silver-coated silica microspheres, their characterisation and application in an enhanced fluorescence immunoassay compatible with flow cytometry readout. In our method, a seed Au colloid is first covalently bound to (3-aminopropyl)-trimethoxysilane (APTMS) modified silica beads (400 nm and 5 μm in diameter), followed by silver shell over coating. To test the ability of such nanostructured surfaces to enhance fluorescence we used a model immunoassay, rabbit IgG-IgG rabbit antibody, labeled with AlexaFluor 430. The enhancement factor was determined as the ratio of the corrected fluorescence intensity on the silvered surface to one

on the surface of unmodified beads based on the fluorescence spectra. Laser scanning microscopy at 405 nm excitation wavelength was used to show the enhancement of fluorescence emission for the samples with the Ag layer. Furthermore, we demonstrated the flow cytometry readout of this immunoassay and we have shown that it was enhanced, by examining the fluorescence-intensity histograms of beads with and without Ag nanostructures.

Experimental section

Materials

The following materials were purchased from Sigma-Aldrich and used as received: gold (III) chloride trihydrate, trisodium citrate, sodium borohydride, (3-aminopropyl) trimethoxysilane (APTMS), ethanol, concentrated H_2SO_4, silver enhancing solution A, silver enhancing solution B (enhancing kit), Rabbit and goat IgG, AlexaFluor 430-labeled anti-rabbit IgG, PBS buffer, BSA, poly-L-lysine. 30% H_2O_2 was obtained from VWR. Glass microscope slides were obtained from Fisher Scientific. Nanopure water (>18.0 MΩ) purified using the Millipore Milli-Q gradient system, was used in all the experiments. 400 nm and 5 μm silica microspheres were purchased from Bangs Laboratories Inc.

Synthesis of Au colloid

The Au colloid was synthesized according to the Jana method with slight modifications [95]. In a typical Au colloid synthesis, a 20 mL aqueous gold solution containing 0.25 mM $HAuCl_4$ and 0.25 mM trisodium citrate was prepared. Then 0.6 mL of a 0.01 M $NaBH_4$ solution was added at once into the gold solution under constant stirring. Stirring was continued for another 1 min. The solution turned a wine red colour indicating particle formation. The solution was used as a stock gold seed solution 4 h after preparation, allowing all the excess borohydride to degrade.

Preparation of silica-Au assemblies

Silica-Au assemblies were prepared using a modified Westcott method [96]. In a typical reaction, about 50 μL of APTMS was added to 100 mL of silica nanoparticle solution in ethanol. After reacting overnight, the solution was held at a low boil for 1 h to promote covalent bonding of APTMS to the surface of the silica nanoparticles.

The final solution was centrifuged and washed with nanopure water 3 times. Next, 0.5 mL, 1 mL and 2 mL of the gold seed solution were, respectively, added to 40 μL of resuspended silica nanoparticles with APTMS coating. The mixed solutions were stirred for 30-90 min to allow gold particles binding to silica beads surface, followed by centrifuging and washing as previously described.

Deposition of silver layer on silica beads

This deposition was performed using protocol previously reported by our group. The equal amounts of the silver enhancer solutions A (2.0 mL) and B (2.0 mL) were well mixed using a vortex. Then equal amounts of mixed silver enhancer solution A and B were added into the 100 μL of silica-Au solution and allowed to react for different periods: 10 sec, 1 min, 3 min and 5 min. The silver deposition procedure was carried out with constant shaking and in the dark as the silver enhancer kit is light sensitive. The reaction between the nanoparticles and the enhancer solution was terminated by washing. The final silica-core, silver shell nanoparticles were dried in air for characterization and further experiments.

Model immunoassay

The glass slides were cleaned by soaking in the piranha solution for at least overnight and then rinsed with nanopure water and dried in air before use. (Caution: piranha solution is extremely caustic. Use only with extreme care.) The slides were then dip coated with poly-L-lysine solution (freshly prepared solution: 8 mL of water +1.0 mL of 1% poly-L-lysine solution + 1.0 mL PBS buffer, pH 7.4). After drying in air, each slide was covered with tape containing 8 punched holes to form wells on the surface. Each well was filled with 20 μL of suspension of beads: the first slide with Ag-coated 400 nm silica beads, the second with 400 nm uncoated silica beads, the third with 5 μm Ag-coated beads and the fourth with uncoated 5 μm beads, and all were air dried. Two sets of samples were prepared. Such prepared slides were noncovalently coated with rabbit IgG (first set, referred to as the sample slide) or with goat IgG (second set, acting as the control slide). To this aim, a coating solution of IgG (40 μg/mL of rabbit IgG dissolved in PBS buffer, 50 mM, pH 7.4) was added to each well (20 μL/well), and slides were incubated for 2 to 4 h at room temperature in a humid chamber. This

procedure leads to spontaneous binding of albumin proteins (goat and rabbit IgG) to the glass and silver surface to form a complete monolayer, in agreement with earlier reports 24. The slides were then rinsed with PBST (PBS with 0.05% Tween 20) and PBS, which were used in all washing procedures. Blocking was performed by adding the blocking solution (1% BSA in PBS solution) and incubation for 1 h in a humid chamber. After rinsing, each well was filled with 20 μL per well of anti-rabbit IgG AlexaFluor 430 conjugate (diluted to 40 μg /mL with PBS buffer, 50 mM, pH 7.4) and incubated for 2 hours at room temperature in humid chamber. After that samples were rinsed and stored at 4^oC before measurement.

Characterization

The extinction spectra of Au-silica and Ag-silica assemblies were measured using a Cary spectrophotometer (Cary 5000 UV-Vis-NIR, Varian Inc.). Transmission Electron microscopy (TEM) images were taken on a PHILIPS CM10 system at an accelerating voltage of 100 kV. Scanning electron microscopy (SEM) images were taken by using a JEOL-JEM-6480 LA at an accelerating voltage of 200 kV. Fluorescence spectra were obtained using a Fluorolog-Tau-3 system with 450W Xe lamp excitation. In this measurement, the glass slides were maintained at 45 degree illumination in an upright position in the solid sample holder. The spectral width was set to 8 nm. The emission spectra were respectively excited at 430 nm and 488 nm, recorded over a range of 460-750 nm and a range of 500-750 nm. Simultaneous fluorescence images and lifetime measurements were taken at the same experimental conditions on the Leica SP2 confocal laser scanning microscopy system with Fluorescence Lifetime Imaging (FLIM) based on time-correlated single photon counting (SPC-830) module with 256 by 256 channels from Becker and Hickl. The excitation was provided by a 405 nm pulsed laser diode modulated at 40 MHz and with power of 0.9 μW, and the emission was collected over a range of 500-600 nm. The fluorescence signal passing through an Airy pinhole (114 micrometers) was detected by the PMC-100-0 detector. This system makes it possible to reliably measure lifetimes in excess of 100 ps. The BD FACSAria^{TM} flow cytometery (BD Biosciences) with 488 nm excitation wavelength was used to examine both fluorescence intensities of the beads and their scattering signals. The sheath

fluid consisted of undiluted Osmosol (Lab Aids Pty Ltd, Narrabeen, NSW, Australia). Two different bead sizes were examined (400 nm and 5 μm) in a single-cell mode. To increase the accuracy analysis for the 5 μm beads, a gate (R1) was defined around the single beads populations within plot of Side Scatter (SSC) versus Forward Scatter (FSC), and the events detected in R1 were analysed by using a fluorescence intensity histogram. Due to the difficulty for the flow cytometry to discriminate 400 nm beads, no gate was applied for the relevant fluorescence histogram. In order to quantify the fluorescence enhancement factor, the integration of fluorescence intensity from individual beads was required. To this aim we used a "FCSEXTRACT.EXE" program (http://research.stowers-institute.org/efg/ScientificSoftware/Utility/FCSExtract/index.htm) to extract the flow cytometry data into the spreadsheet.

Results and discussion

The first step towards producing silver nanostructures on silica beads is the synthesis of a highly uniform gold colloid, which enables controlled growth of uniform silver nanoparticles attached to the beads surface. The synthesized gold colloid was characterized by absorption spectroscopy (data not shown). The extinction spectra had a maximum at 519 nm, indicating the absence of aggregation and the particle size of 8 nm as estimated by the Mie theory. The narrow (1.6 nm) full width half maximum (FWHM) of the peak suggested that the Au colloid solution is practically monodisperse.

In order to bind the gold colloid to the silica beads, we used APTMS whose amine group shows strong affinity to gold. Consequently, when an aqueous solution of gold nanoparticles is mixed with APTMS-functionalized silica beads, the gold nanoparticles become immobilized on the surfaces of the silica beads. We noticed a color change of the silica beads solution (after centrifuging and washing) from white to grey red as a result of Au coating. By varying the amount of gold colloid solution from 0.5 to 2 mL, we were able to observe varying gold coverage on their surface (see Fig. 7.1). Another evidence that the gold colloids were attached to the silica beads was observed in the extinction spectra (see Fig. 7.2). In these measurements the concentrations of Au coated and uncoated silica beads in solutions were the same.

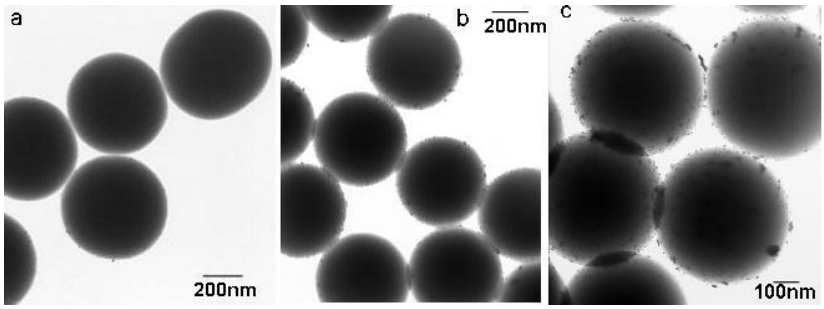

FIGURE 4.1: TEM images of Au-coated silica beads produced using different amounts of gold colloid solution: (a) 0.5 mL, (b) 1 mL, (c) 2 mL.

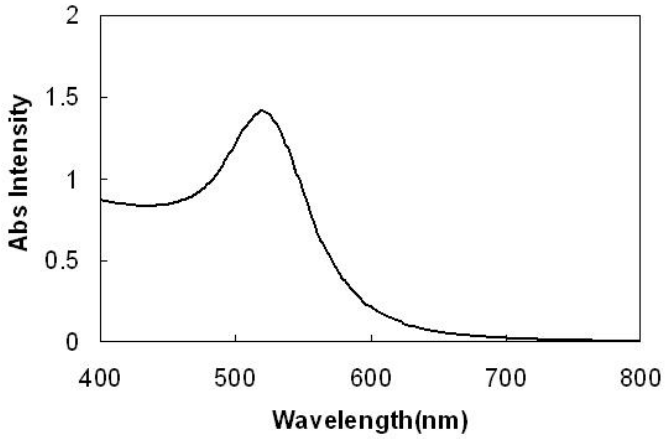

FIGURE 4.2: Absorption spectra of the pure silica beads and samples at different Ag enhancing times, as indicated in the graph.

The silver deposition was done by applying the silver enhancer solution to Au colloids attached to the silica beads. The thickness of the silver layer overcoating was controlled by the duration of the silver enhancing step. The process of silver enhancement can be understood as follows. A silver enhancer solution consists of silver ions and a reducing agent, buffered at an acidic pH. The reaction between silver ions (in silver nitrate) and the reducing agent, hydroquinone, is explained by the following reaction:

$$2AgNO_3 + C_6H_4(OH)_2 \rightarrow CO(CHCH)_2CO + 2HNO_3 + 2Ag \downarrow$$

When the Au colloids are placed in such solution containing the reducing molecules, hydroquinone and silver ions, they will attract both. After attaching to the Au crystal, the hydroquinone molecule releases two electrons into the valence cloud of the Au

crystal lattice. These extra electrons eventually cause two silver ions to be included into the lattice by reducing them to metallic silver atoms. At the same time, hydroquinone molecules are oxidized to quinine and physically released from the growing silver deposit.

Fig. 7.3 shows several extinction spectra of Ag-coated silica beads at different Ag exposure times. The extinction coefficient at the peak wavelengths were increased at longer Ag enhancement times and a very small shift toward longer wavelengths (from 375 nm to 381 nm) of the extinction maximum was observed. The shape of the absorption spectrum suggests that light incident on the beads is scattered by silver particles adhering to the silica surface. The SEM images of beads prepared with 10 sec, 1 min, 3 min and 5 min silver enhancing time, respectively are shown in Fig. 7.4. As expected, silica beads with 3 min silver enhancing had a much higher and more even silver coverage compared to beads with a shorter silver enhancing time. On the other hand, longer enhancing times were causing the formation of nanoparticle clusters. In such clusters, where particles are in close proximity the coupling of the neighboring particles plays an important role, and it modifies the dipole-dipole interaction between the dipole moments of the coupled particles. This dipole coupling concept has been successfully applied to the modeling of the optical properties of the silver fractal clusters, and our spectra at longer enhancing times very closely resemble the published results [97, 98].

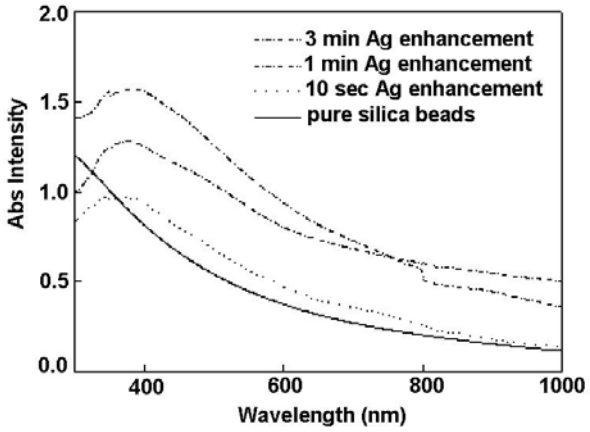

Figure 4.3: Absorption spectra of the Ag layer on the surface of silica beads

In order to assess the effect of silver nanostructures on fluorescence amplification

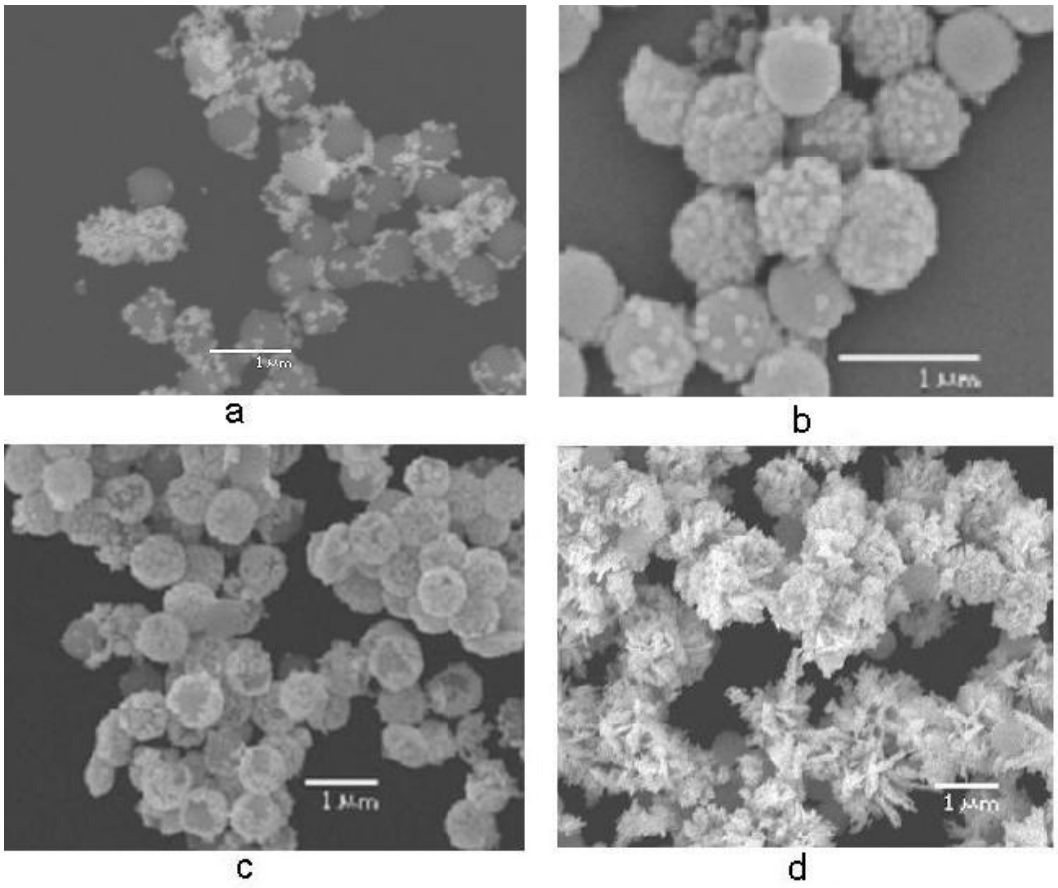

FIGURE 4.4: SEM images of silica beads with silver deposition for (a) 10sec, (b)1 min, (c)3 min and (d)5 min

we carried out a model immunoassay with a fluorescently labeled antibody. The experiment was designed to ensure that fluorophore coverage of the surfaces with and without silver nanostructures has been accurately corrected. The standard approach to determine the fluorescence amplification factor on metal nanostructures is simply to divide the fluorescence intensity of fluorophore on metal-coated surface by the intensity of the fluorophore on the uncoated surface. However this approach is directly applicable only to planar surfaces and not to collections of beads, where it is impossible to maintain the same number of beads. We emphasize that in this study, after the immunoassay was performed, the beads were placed on plain glass surfaces in the wells and dried for the measurement of fluorescence. This process tends to produce nonuniform coverage, and gives no guarantee that the number of beads will be exactly the same in both samples. We have accounted for the above factors by correcting the

observed fluorescence intensities in the following fashion. We firstly measured the fluorescence intensities from the wells on our glass slides with deposited Ag-coated and uncoated silica beads but without immunoassay as a background scatter control samples. Then we measured the samples of supernatants of AlexaFluor 430 IgG antibody collected from each well after immunoassay binding period and before washing and compared their fluorescence intensity with the original AlexaFluor430-labeled protein solution under the same experimental conditions (see Fig. 7.5 for 400 nm beads and Fig. 7.6 for 5 nm beads). These measurements were done for 8 wells on each type of samples, for improved accuracy and the results and standard deviations are presented in the Table 1.1. Subsequently, we estimated how much protein was attached to the silica beads with and without the Ag layer, respectively, by the following calculation. By subtracting the fluorescence intensity from supernatant of each sample from one of the original AlexaFluor 430-labeled protein solution, we estimated how much protein was bound to each sample. This value was divided by the fluorescence intensity of the original AlexaFluor 430-labeled protein solution. We thus obtained the corresponding binding efficiency for each sample (see Table 4.1), indicating the amount of protein remaining on the silica beads surface. Then we divided the observed fluorescence intensity from the wells for each sample by its corresponding binding efficiency and thus obtained the corrected fluorescence intensity. This value was equivalent to fluorescence intensity for the uniform coverage on each glass slide for the different samples. Finally, we compared the corrected fluorescence intensities from the model immunoassay on beads with Ag enhancement and on unmodified beads. The average enhancement factors for the samples with 10 sec, 1 min and 3 min Ag enhancing time for 400 nm silica beads were: 3.4, 4.9 and 8.5, respectively. In the case of large 5 μm silver-coated silica beads, the enhancement factor for the sample with silver enhancing of 3 min was about 10.1. (see Table 4.1)

To evaluate the level of non-specific binding of AlexaFluor 430-labeled anti-Rabbit antibody we used goat-IgG instead of rabbit IgG in our immunoassay protocol. Goat IgG was non-covalently bound on the surface of each type of samples with deposited silica beads: 400 nm Ag-coated and uncoated and 5 μm Ag-coated and uncoated. The

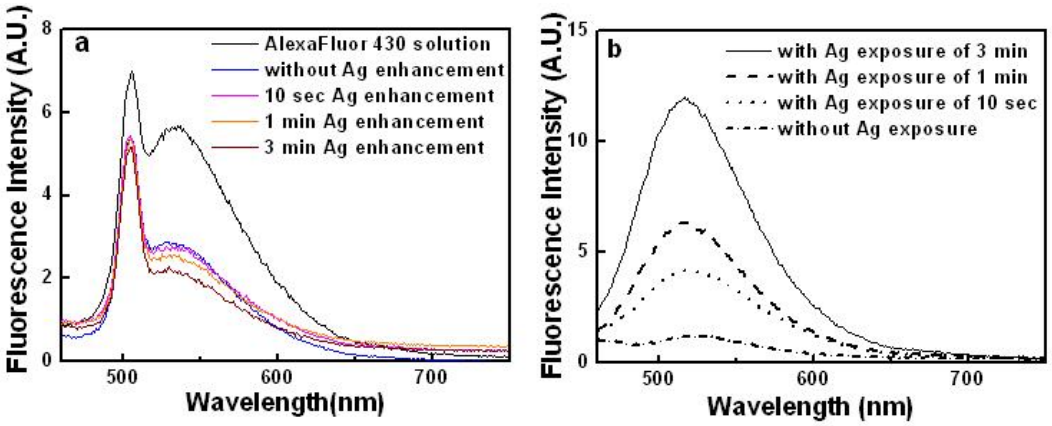

FIGURE 4.5: Fluorescence intensities observed from the supernatant (a)(from top to bottom: original AlexaFluor 430 solution, without Ag enhancement, 10sec, 1 min and 3 min Ag enhancement)and the glass surfaces(b) (from top to bottom: 3 min, 1 min, 10 sec and without Ag enhancement) for different samples with silica beads of 400nm.

TABLE 4.1: Binding efficiencies and corrected enhancement factors for 400 nm and 5 μm silica beads at different silver enhancing times. The data marked with a * were taken on 5 μm silica beads. Measurements taken at 430 nm excitation.

	without Ag	10sec	1 min	3 min	3 min*
binding effiency	0.6±0.03	0.6±0.03	0.7±0.04	0.7±0.05	0.7±0.04
enhancement factor	1.0±0.02	3.4±0.02	4.9±0.04	8.5±0.04	10.1±0.03

level of non-specific binding was calculated by comparing the maximum fluorescence intensity from AlexaFluor 430 labeled antibody in a non-specific immunoassay to the maximum fluorescence intensity in a specific immunoassay for the same type of samples (same type of beads) The results indicated a very low level of about 2% of non-specific binding for each type of samples irrespectively of the bead size and whether they were Ag-coated or uncoated.

The laser scanning microscopy images of the immunoassay of the beads with and without Ag enhancing have also been recorded. As shown in Fig. 7.7, when the silver enhancing time was increased up to 3 min, the fluorescence signal observed from the silvered area was much greater than that from the pure silica beads surface, demonstrating fluorescence enhancement. The beads showed non-uniform enhancement, reflected in the intensity histogram.

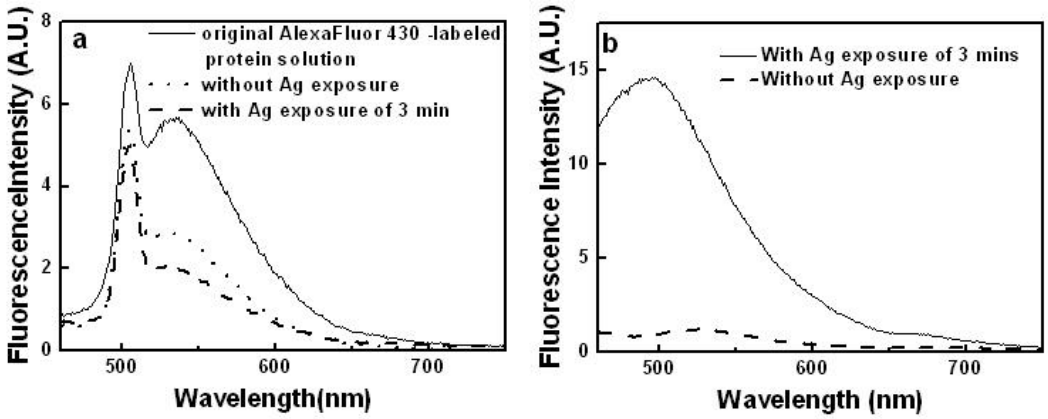

FIGURE 4.6: Fluorescence intensities from the supernatant (a) (from top to bottom: original AlexaFluor 430 solution, glass surface without Ag enhancement and glass surface with 3 min Ag enhancement) and from the glass surfaces (b) (from top to bottom: 5 μm silica beads with 3 min Ag enhancement and without Ag enhancement.)

For a more complete characterization of the effect of metal nanostructures on the fluorescence we carried out the measurements of fluorescence lifetimes. As discussed in the literature, metal enhanced fluorescence is accompanied by an increase in the quantum yield and a decrease in the lifetime of a fluorophore located in the proximity of the metallic nanoparticles. The fluorescence lifetime provides unambiguous distinction of the metal-induced fluorescence enhancement. In order to confirm the enhancement mechanism, we measured the lifetime of AlexaFluor 430 on the silica surface with and without silver layer. The decay curves shown in Fig. 7.8 show a reduction of fluorescence lifetime due to the silver nanostructure on the silica beads surface. These decay curves were fitted by a double exponential function with two characteristic lifetime components. Their values and the average lifetimes for different samples are shown in Table 4.2. In the sample without silver enhancing, the AlexaFluor 430 had an average lifetime of about 2.50 ns. In the remaining samples, with Ag enhancement, the AlexaFluor 430 average lifetimes were 0.78, 0.79 and 0.70 ns for 10 sec, 1 min and 3 min silver enhancing, respectively; these values were lower compared to the control sample without Ag enhancement. Such reduced lifetime has two major implications, higher photostability and a higher number of emitted photons per unit time under the same excitation conditions. Both of these properties make it possible to use shorter exposure

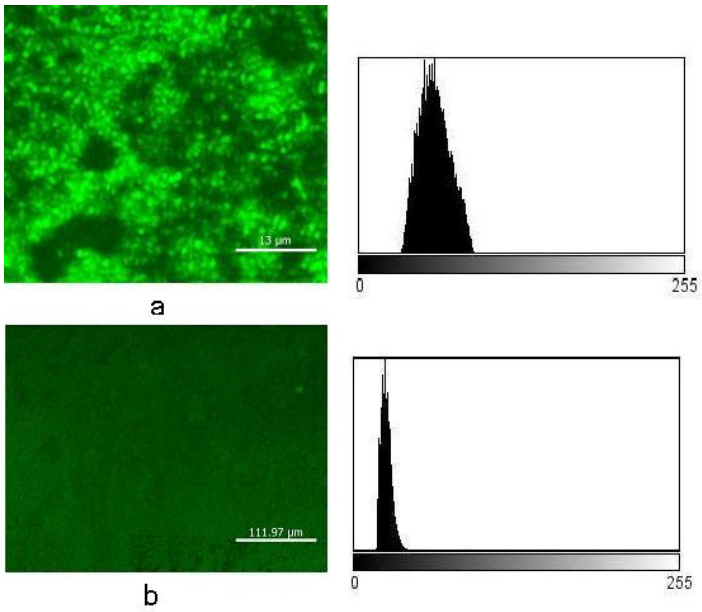

FIGURE 4.7: Laser scanning microscopy images and corresponding histograms of samples with 3 min Ag enhancement (a) and without Ag enhancement (b). The horizontal axis of the histogram shows brightness in arbitrary units.

time or obtain higher signal to noise for comparable exposure times, thus increasing sensitivity and detectivity in any fluorescence measurements, including flow cytometry.

TABLE 4.2: Fluorescence intensity decay analysis. $\tau_{1,2}$ denotes decay times of the two lifetime components, τ is the average lifetime.

	τ_1	τ_2	τ
10 sec Ag enhancement	0.78±0.09	2.99±0.10	0.78±0.10
1 min Ag enhancement	0.46±0.08	2.33±0.08	0.79±0.08
3 min Ag enhancement	0.51±0.10	2.26±0.10	0.70±0.10
without Ag enhancement	1.89±0.08	3.90±0.09	2.50±0.09

To confirm this we carried out flow cytometry experiment on our bead immunoassay with and without Ag nanostructures. Fig. 7.9 shows flow cytometry scanning results for 5.0 μm diameter fluorescence beads. This figure shows that Ag surface modification affects both forward scattering (FSC) and side scattering (SSC). This result is consistent with the highly non-uniform surface coverage, where denser Ag nanostructure on

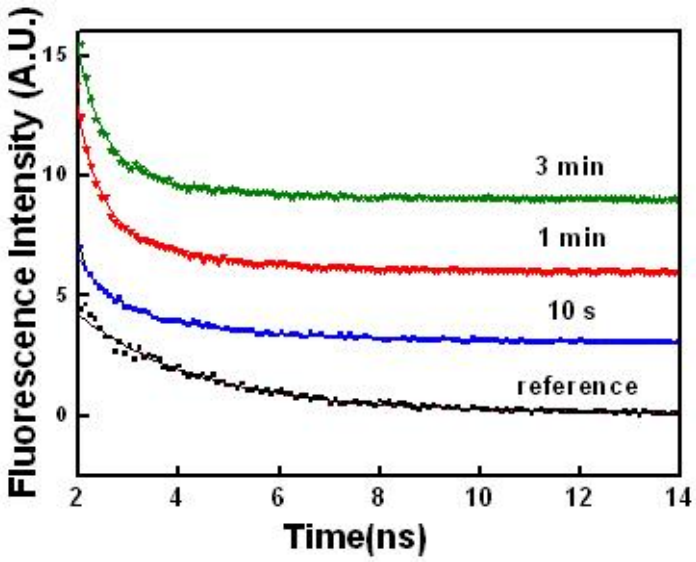

Figure 4.8: Representative fluorescence lifetime decay curves of AlexaFluor 430-labelled immunoassay measured on samples with different Ag enhancing times.

the silica beads surface resulted in stronger 90^o angle scattering. The flow cytometry results show that the Ag deposition for 3 min produced most uniform and highly fluorescence enhancing silica beads, with the enhancement factor of 3.7 compared to silica beads with the same immunoassay but without Ag nanostructures. The coefficients of variation (CV) calculated for these samples (defined as the ratio of standard deviation (σ) of the fluorescence intensity of a population of beads to the mean (μ) itensity (CV=σ/μ)) are: 0.61, 0.69, 2.1, 0.7 for fluorophores deposited on 5 μm silica beads uncoated, and Ag-coated with 10sec, 1 min and 3 min silver deposition , respectively. Very similar CV values for the uncoated, 10 sec and 3 min Ag coated beads indicate that in these samples the fluorophore and metal coverage is relatively uniform. The Ag deposition time of 1 min produced some beads with very sparse Ag nanostructures, since the SSC spread was observed over a large region in Fig. 7.9c left, and this resulted in a broader fluorescence histogram (Fig. 7.9c right) and a higher CV value. We did not observe aggregation for 5 μm beads used in these experiments. Fig. 7.10 shows the flow cytometry results for the immunoassay on 400 nm diameter silica beads both uncoated and Ag-coated for 3 min. These smaller beads are, in principle, outside of the preferred flow cytometry detection region where the highest sensitivity is achieved, and

gated FSC and SSC detection is practically impossble with these beads. Similarly to the 5 μm beads, the uncoated 400 nm beads, preferentially scatter in forward direction. Likewise, in 400 nm beads with Ag layer deposited for 3 min a comparatively stronger 900 angle scattering was observed. The CV values for 400 nm uncoated beads is high: 11.2, indicating a significant fraction of aggregated beads. In 400 nm beads with 3 minute Ag deposition the CV value of 1.38 was obtained. The fluorescence histogram of 400 nm beads with Ag deposition for 3 minutes (see Fig. 7.10b) was used to derive the fluorescence enhancement factor of 3.0 for the immunoassay (see Table 4.3).

TABLE 4.3: Calculated enhancement factor for samples with different Ag enhancing times by using flow cytometry.

		enhancement factor
	without Ag enhancement	1.0±0.02
5 μm silica beads	10 sec Ag enhancement	0.9±0.04
	1 min Ag enhancement	2.0±0.03
	3 min Ag enhancement	3.7±0.06
400 nm silica beads	without Ag enhancement	1.0±0.02
	3 min Ag enhancement	3.0±0.05

The average enhancement factors achieved for 5 micrometer and 400 nm beads in flow cytometry experiments (3.7 and 3.0) were lower than previously observed for the same beads deposited on glass slides (10.1 and 8.5). We propose the following explanation of this difference. The excitation wavelengths in the spectroscopy/microscopy and flow cytometry experiments were slightly different: 405 nm and 430 nm for immunoassay on the beads on glass slides and 488 nm in flow cytometry measurements. The absorption spectra of Ag enhanced silica beads at various silver enhancing times measured on dried slides showed the plasmon resonance band maximum in 375 -380 nm range. These peak wavelengths are expected to slightly shift towards longer wavelength in water medium used in our immunoassay experiments. The plasmon resonance within

this wavelength range is expected to enhance the excitation/emission of our model fluorophore AlexaFluor 430 more strongly at 405 or 430 nm excitation wavelength than at the 488 nm excitation wavelength used in flow cytometry experiments. Thus we attribute the observed differences to stronger enhancement combined with the much stronger excitation efficiency of this fluorophore in the absence of metal nanostructure at 405/430 nm as compared with 488 nm excitation.

To confirm that the discrepancy between the results is due to the different excitation wavelength used in fluorimetry and flow cytometry, we repeated the immunoassay experiment with 400 nm and 5 micrometer silica beads with and without Ag enhancement under the same experimental conditions as previously except that the excitation of 488 nm instead of 430 nm was used. Fig. 7.11 shows the observed fluorescence intensities for different samples. By calculation, the fluorescence enhancement factors of 3.3 for 400 nm silica beads and 4.1 for 5 μm were achieved. Such results were similar to those in flow cytometry experiments, indicating that the consistent enhancement factors can be achieved by using these two measurement systems. At the same time we have also demonstrated that the enhancement observed in flow cytometry can be further optimized, by bringing closer the plasmon resonance frequency in the metal nanostructures to the excitation wavelength available in the flow cytometry system. With appropriate strategies for such optimization, enhancement factors as high as 100 and beyond should be achievable.

Conclusions

In this work, we have demonstrated the use of silver nanostructures on the silica beads surface as an amplification mechanism for a flow cytometry bead immunoassay. The Ag-coated silica beads after 3 min silver enhancing time produced strong (8.5-fold and 10.1-fold) enhancement factor of emission intensity of Alexa 430 fluorophore excited at 430 nm for 400 nm and 5 um beads respectively. This enhancement was mediated by plasmon resonance in clustered silver nanoparticles. The emission intensity increase was accompanied by 3.5 times reduction in the lifetime of a fluorophore confirming the MEF mechanism of enhancement. Both 400 nm and 5 um beads were compatible with flow cytometry readout at 488 nm, although lower enhancement factors of 3.0 and

3.7 were obtained, which were consistent with less favourable overlap of the plasmon resonance with 488 nm excitation wavelength used in the flow cytometry experiment.

Although this work focuses on application of silvered beads for flow cytometry bead immunoassays, we emphasise that such beads should have much broader applicability. Firstly, silver nanoparticles are excellent biocompatible surfaces for the immobilization of enzymes and nucleic acids, and extension of the present work to, for example amplified DNA and RNA assays should be straightforward. These have implications not only for the detection of disease biomarkers and genes, but also microbial assays. Moreover the electromagnetic mechanisms behind fluorescence enhancement have a common core with those behind surface enhanced Raman scattering (SERS), and it is likely that our approach will lead to improved SERS substrates - for those assays where SERS detection is preferred. Other advantages of the beads such as the ability to be used with various enrichment and filtering systems to concentrate the analyte are further enhanced by our fluorescence amplification approach. Taking these factors into account, we anticipate that the beads coated with metal nanostructures will be useful as templates and separation tools in a variety of bio-assay systems and biosensors and that lead to significant improvement of their performance.

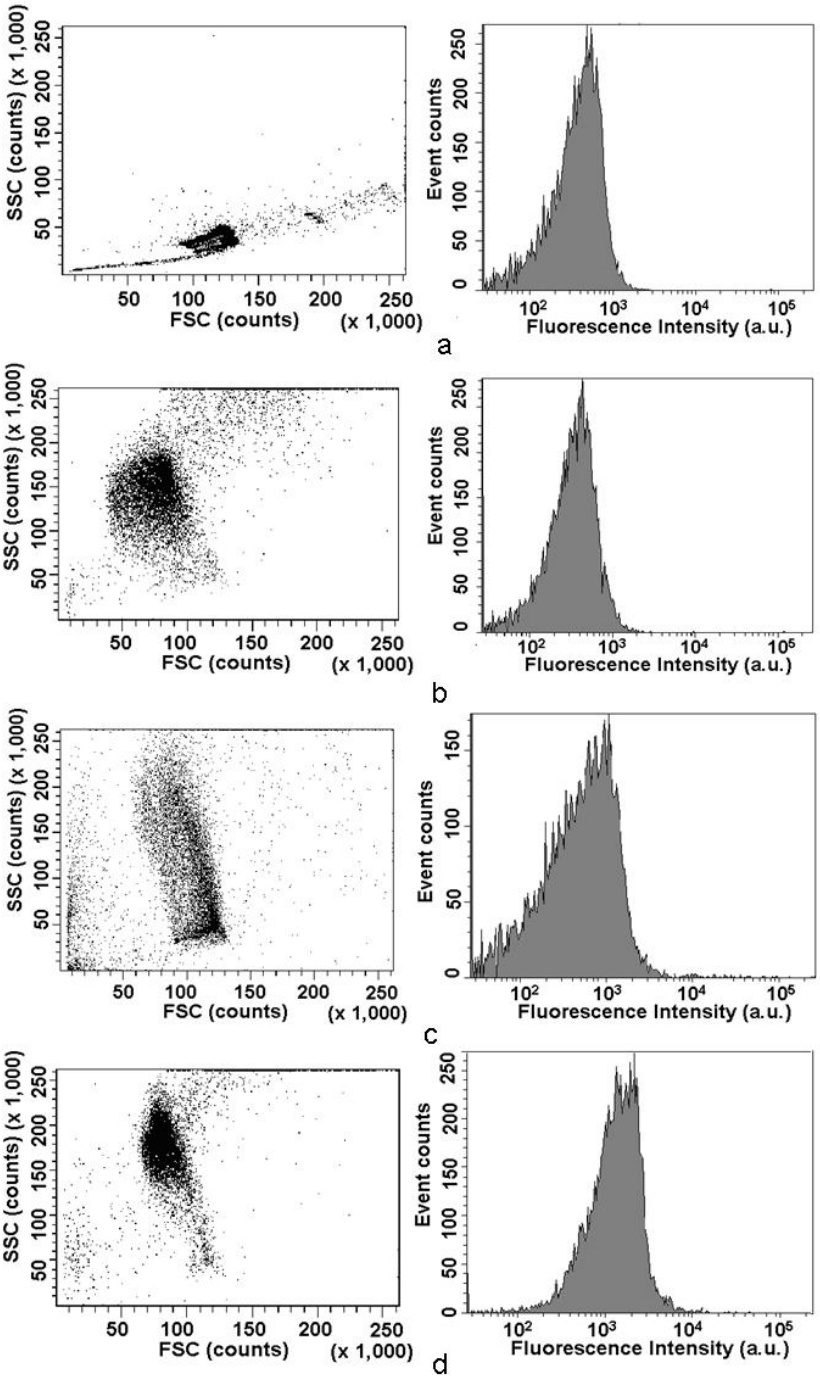

Figure 4.9: Flow cytometry results for 5 μm silica beads: AlexaFluor 430-antibody on the silica beads without Ag enhancing (a), with 10 sec Ag enhancing (b), with 1 min Ag enhancing (c) and with 3 min Ag enhancing (d). Left, forward scattering (FSC) versus side scattering (SSC); Right, fluorescence histograms.

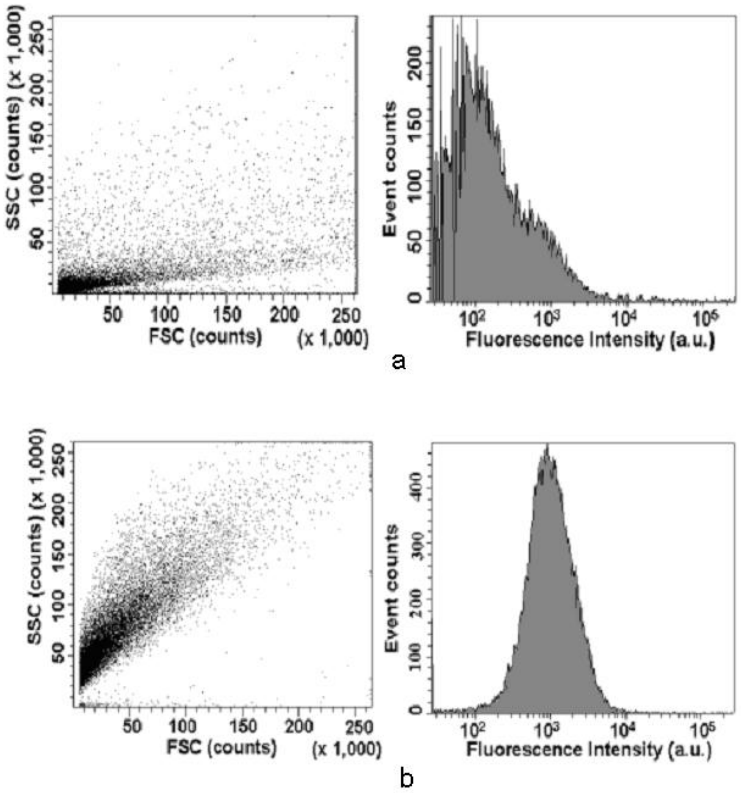

FIGURE 4.10: Flow cytometry scanning for AlexaFluor 430 labelled -silica beads (400nm) without Ag enhancement (a) and with 3 minutes Ag enhancement (b). Left, forward scattering vs. side scattering; Right, fluorescence histogram.

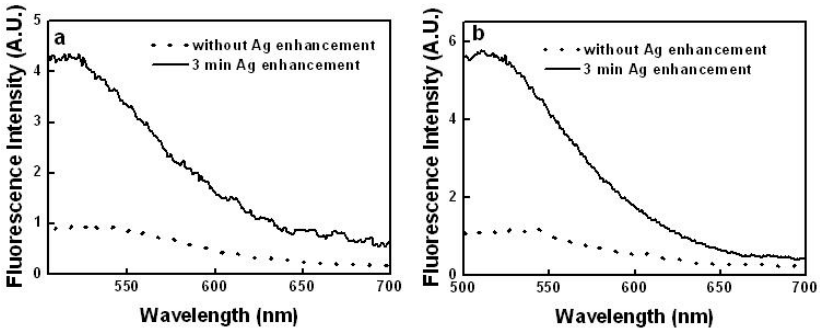

FIGURE 4.11: Fluorescence intensities from the glass surfaces for 400 nm (a) and 5 μm (b) silica beads under the 488 nm excitation. (from top to bottom: with 3 min Ag enhancement and without Ag enhancement)

5

Metal Nanostructure Enhanced Fluorescence of Europium Chelate BHHCT – Eu^{3+} applied to Bioassays and Time-gated Bioimaging

Introduction

Upon chelation with suitable light-absorbing ligands, lanthanides exhibit luminescence characterized by exceptionally long decay times. In addition to long luminescence lifetimes, the chelates of lanthanide ions such as Eu(III), Sm(III), Tb(III) and Dy(III) possess some unusual chemical and spectroscopic characteristics compared with conventional organic fluorescence dyes, such as large Stokes shift and ion-specific emission

spectra [99]. The lanthanide chelates are gaining widespread acceptance in fluorescence labeling as a result of expanding applications in a wide variety of bioanalytical assays, in diagnostics, sensing and in imaging, especially with time-gating that offers exceptionally high background rejection [100–104]. However a direct consequence of long lifetimes is limited fluorophore brightness. This work is designed to address the issue of lanthanide brightness, by employing the approach of metal-enhanced fluorescence (MEF) [105, 106].

The MEF effect is due to interactions of the excited fluorophores with surface plasmon resonance in metals, and it is particularly prominent in metal nanostructures. Such nanostructures are able to produce desirable effects including increased quantum yields, decreased lifetimes, increased photostability, and potential for improved energy transfer [105–108]. The surface plasmon resonances in metal nanostructures lead to increased radiative rates and may create regions of enhanced local electromagnetic field. At present MEF are obtained with mostly Ag nanostructure [2–5, 46, 47] with occasional use of gold [52] and aluminium [109]. Silvered surfaces performed well in MEF applications based on silver nanoscale structures of various shapes, including silver island film (SiFs) [46], silver colloids [2, 4], silver nanorods [5], silver triangles [47], and silver fractal-like nanostructures [3]. The fluorescence enhancement can be increased up to several thousand fold when using Ag nanostructures [110, 111] compared to that using gold and aluminum nanostructures. In the literature the conventional dyes were among the most intensely studied including fluorescein [112], rhodamin B [113], indocyanine green [114], Cy3, Cy5 [115], Pacific blue, lissamine and Texas red [116]. Although some studies of metal enhancement of lanthanides were recently published [117–119], to our knowledge, there were no earlier studies of silver-enhanced fluorescence of lanthanide chelates and their bio-imaging applications.

In this work, we examined the effects of silver nanostructures on a tetradentate β-diketone ligand, $4,4'-bis(1",1",1",2",2",3",3"-heptafluoro-4",6"-hexanedion-6"-yl)chlorosulfo-o-terphenyl$ (BHHCT), which forms a very stable complex with Eu^{3+} with desirable fluorescence properties (see Fig. 8.1) [100, 120]. BHHCT has one chlorosulfonyl group that is useful for coupling with proteins, where covalent bonds

are formed between the −SO2Cl group of BHHCT and amino groups of proteins, producing −SO2 − NH−bonds [100]. Consequently its soluble Eu(III) complex can be easily coupled to proteins. Two methods were developed for preparation of Ag nanostructures, Ag nanostructures deposited on glass slides and on silica beads. In the second method Ag-coated silica beads were also deposited on glass slides and used as the substrates. The first approach is simple and produce a MEF substrate leading to good uniformity [94]. The second approach is relatively complicated but the Ag-coated beads offer the advantage of reduced reaction time in suspension, important in immuno- and nucleic acid assays as well as the possibility of the flow cytometry readout.

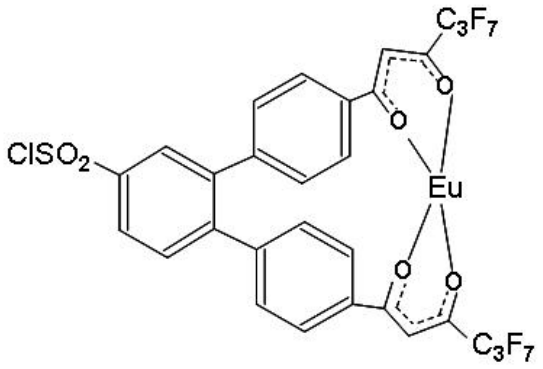

FIGURE 5.1: Structure of BHHCT − Eu^{3+} chelate.

To examine the effect on the fluorescence intensity and lifetime induced by silver nanostructures near BHHCT − Eu^{3+} complexes, we developed an assay, where the SA-labeled BHHCT − $Eu^{3+}$was bound to the biotin-conjugated anti-mouse IgG antibody on glass slides or on silica beads. This assay was carried out with and without Ag enhancement. The enhancement factor was determined as the ratio of the corrected fluorescence intensity (as defined in Measurements section of this article) on the silvered surface to the intensity on the surface of unmodified glass slides or silica beads based on the fluorescence spectra. Further we demonstrated that metal enhanced fluorescence can also be employed for improving brightness in a bioimaging experiment of BHHCT − Eu^{3+} labeled environmental microorganisms, Giardia cysts. These 6 μm wide, 9 μm long and ∼0.5 μm thick pathogens were imaged using 365 nm wavelength UV LED

excitation in a time-gated fluorescence microscope.

Experimental section

Materials

The following materials were purchased from Sigma-Aldrich and used as received: gold (III) chloride trihydrate, trisodium citrate, sodium borohydride ($NaBH_4$), (3-aminopropyl) trimethoxysilane (APTMS), ethanol, methanol, concentrated H_2SO_4, silver enhancing solution A, silver enhancing solution B (enhancing kit), strepavidin (SA), glutaraldehyde, bovine serum albumin (BSA), europium (III) chloride ($EuCl_3 \cdot 6H_2O$), sodium carbonate ($NaHCO_3$), sodium azide, phosphate buffered saline (PBS, pH 7.4) and poly-L-lysine. Biotinylated goat anti-mouse IgG antibody was purchased from Millipore Co. Giardia lamblia and its mouse monoclonal antibody were purchased from Biotech Frontiers Pty. Ltd. Silica microspheres, 400 nm in diameter, were purchased from Bangs Laboratories, Inc. The ligand BHHCT was prepared as previously reported [100]. 30% H_2O_2 was obtained from VWR. Glass microscope slides were obtained from Fisher Scientific. Nanopure water (>18.0 MΩ) purified using the Millipore Milli-Q gradient system, was used in all experiments.

Conjugation of SA-BSA with BHHCT-Eu

Conjugation of SA-BSA with BHHCT – Eu^{3+} was performed by using the method developed in Reference [121] with modifications (see Fig. 8.2a). First, 1 mg of SA and 1 mg of BSA were dissolved in 2 mL of 0.01 M PBS, at pH 7.4, and 0.1 mL of 1% glutaraldehyde was added. The reaction was maintained at 4^oC for 24 h, subsequently 0.4 mg of $NaBH_4$ was added, and the solution was reacted at room temperature for 2 h. The solution was dialyzed against saline solution at 4^oC by centrifugation and diluted to 1.5 mL with water, with 12.6 mg of $NaHCO_3$ added. The solution was then adjusted to pH 9.1 with 1 M NaOH. Further, 0.3 mL of dry ethanol containing 2 mg of BHHCT was added dropwise to the solution with continuous stirring. After 1 h of stirring, the undissolved residue was removed by centrifugal filters. Following that, 1.8 μL of 0.04 M $EuCl_3$ was added to the collected solution. The solution was reacted at room temperature for 12 hours followed by adding BSA (0.2%), NaN_3 (0.1%), and NaCl (0.9%). The reaction product was used for the assays described here.

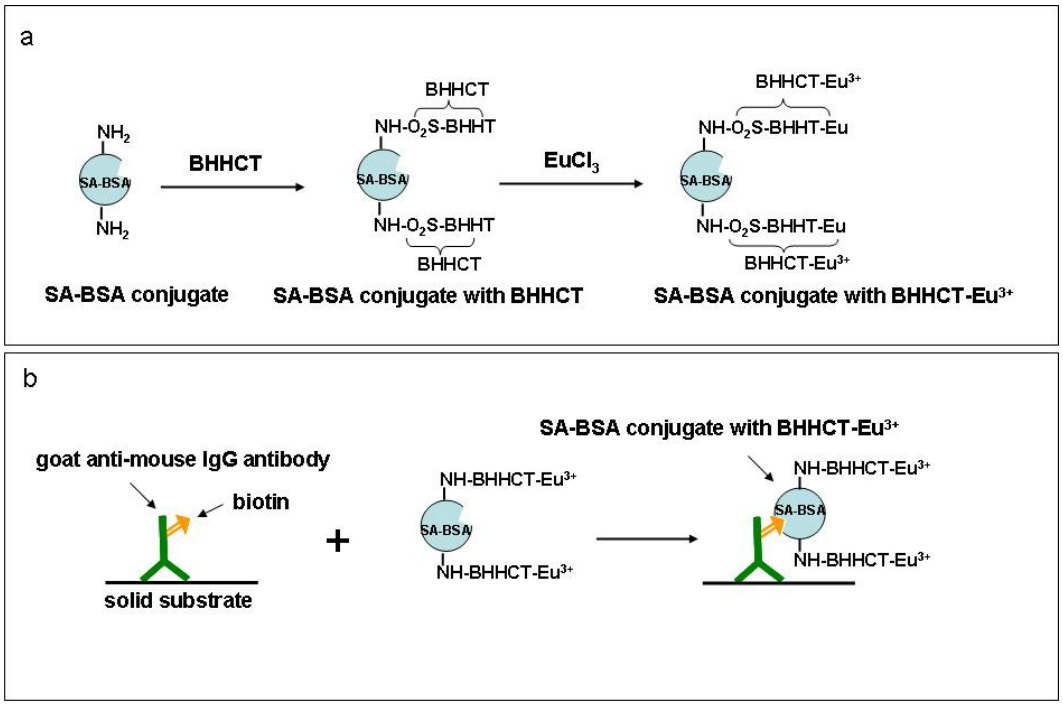

FIGURE 5.2: Schematic representation of conjugation of SA-BSA with BHHCT – Eu^{3+} chelate (a) and the bioassay using BHHCT – Eu^{3+} as a label (b).

Preparation of metal nanostructures (Au core-Ag shell) on glass slides and silica beads

The deposition of Ag nanostructures on the glass slides was performed using a protocol previously reported by our group [94]. The microscope glass slides were first cleaned by a piranha solution consisting of 4 parts of H_2SO_4 to 1 part of 30% H_2O_2 at 60^{o}C. (Caution: piranha solution is extremely caustic. Use only with extreme care.) The glass surface then was derivatized with APTMS by immersing it into 10 mM methanolic solution of this organosilane. After 2 h, the substrate was removed and the slide was rinsed with methanol and water to remove unbound monomers from the surface. Subsequently, the slides were immersed in the Au colloid solution to form a monolayer of Au nanoparticles on the glass surface. A final rinse with water and drying in air concluded the derivatisation process. Equal amounts of the silver enhancer solutions A and B were mixed using a vortex. The glass slides modified by Au colloid were then immersed in the mixed solution to react for different periods: 10 sec, 1 min and 3 min. The silver deposition procedure was carried out in the dark as the silver

enhancer kit is light-sensitive. Glass substrates were thoroughly washed with nanopure water to terminate the reaction between nanoparticles and the enhancer solution. The preparation of Ag nanostructures on the silica beads was carried out in a similar fashion. Firstly, APTMS was added to the silica nanoparticles solution with stirring overnight. Secondly, the Au colloids solution was added to the silica nanoparticles with APTMS coating 30-90 min to allow gold particles binding to silica surface, followed by washing with nanopure water. The deposition of Ag nanostructures on the silica beads was the same as that on the glass slides.

BHHCT – Eu^{3+}-based assay on the glass slides and silica beads

Following the Au colloid self-assembly and silver deposition steps, the glass slides were coated with the poly-lysine solution (freshly prepared solution: 8 mL water +1.0 mL poly-L-lysine + 1.0 mL PBS buffer, pH 7.4) for better protein adsorption and incubated for 30 min, followed by rinsing with water. After drying in air, the slides were covered with a tape containing punched holes to form wells on the surface. Further, 20 μL of biotin-labeled goat anti-mouse IgG antibody solution (40 μg/mL of biotin-labeled goat anti-mouse IgG antibody dissolved in PBS buffer, pH 7.4) was added to each well. The slides were incubated overnight in a humid chamber and rinsed with PBST (PBS with 0.05 % Tween 20) and PBS, which were used in all washing procedures. Blocking was performed by adding the BSA solution and incubation for 1 hour in a humid chamber. After rinsing, each well was incubated for 1 h with 20 μL per well of the BHHCT – Eu^{3+}-labeled SA-BSA (original solution was diluted in PBS at 1:10), followed by a rinse and stored at 4^{o}C before measurement (see Fig. 8.2b). All operations were performed at room temperature. The control experiment for non-specific binding was similar, except that pure goat anti-mouse IgG antibody was used instead of biotin-labeled one. In the case of silica beads, the glass slides were first cleaned by a piranha solution and coated with poly-lysine solution using the same protocol described above. After drying in air, these slides were covered with a tape containing punched holes to form wells on the surface and each well was filled with Ag-coated silica beads, and again, dried in air. The same bioassay as described above was carried out on these bead-based substrates.

Fluorescence imaging of Giardia lamblia

In the fluorescence imaging experiment, Giardia lamblia was immunostained with the BHHCT $-$ Eu^{3+}chelate. In the staining protocol, 10 μL of Giardia lamblia solution (2×10^6 cysts/mL) was mixed with 10μL of mouse anti-Giardia antibody (40 μg/mL), 20 μL of biotinylated goat anti-mouse IgG antibody (40 μg/mL) and 20 μL of SA-BSA conjugate labeled with BHHCT $-$ Eu^{3+}($\sim$50 μg/mL) in a tube (see Fig. 8.3). After incubation for 24 h at room temperature, the cysts were separated by centrifugation at 500 rpm and washed with distilled water several times to remove the unreacted conjugates. At the same time, the wells on the glass slide were filled with solutions of uncoated and Ag-coated silica beads. After silica bead solution dried in air, the Giardia cysts were added to each well and covered with a cover slip for fluorescence microscopy imaging.

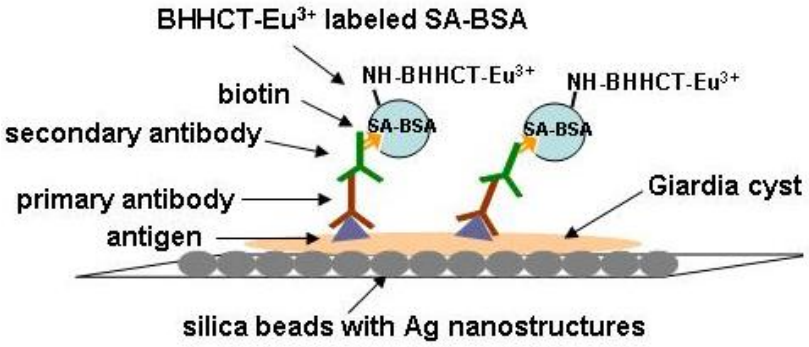

FIGURE 5.3: Schematic representation of immunostaining Giardia lamblia cells with BHHCT $-$ Eu^{3+}.

Characterization

The absorption spectra of BHHCT and SA-BSA conjugates were measured using a Cary spectrophotometer (Cary 5000 UV-Vis-NIR, Varian Inc.). Scanning electron microscopy (SEM) images were taken by using a JEOL-JEM-6480 LA at an accelerating voltage of 200 kV. Fluorescence spectra were obtained using a Fluorolog-Tau-3 system with 450W Xe lamp excitation. In this measurement, the glass slides were maintained at 45 degree illumination in an upright position in the solid sample holder. The spectral width was set to 8 nm. The emission spectra were excited at 350 nm and recorded over a range of 560-670 nm. The spectra were corrected for background

scattering. The fluorescence from each substrate used was measured before performing BHHCT$-Eu^{3+}$-based assay on the glass slides and silica beads and subtracted from the fluorescence after the assay protocol was carried out for that particular substrate. Fluorescence lifetime was measured using purpose-built UV epi-fluorescence microscopy system (10 objective; dichroic beam splitter (Zeiss, FT395)). A high-power UV LED (NCCU033A; Nichia Corp. Japan) with ∼250 mW power at 365 nm ($\Delta\lambda$=10 nm) was used for excitation. In this work the UV LED was operated in a pulsed mode (1 kHz, 100 μs, 10% duty cycle) [122]. In the lifetime measurements, a pair of filters (excitation band pass filter FF01-355/40-25 and emission bandpass filter FF01-607/36-25 BP, from Semrock, http://www.semrock.com/) was employed to suppress the long decaying noise generated from UV LED as reported in our previous work [123]. A silicon photomultiplier (SPMT) detector (SPMMini100, SensL, www.sensl.com) was positioned after the eyepiece, so that the long decaying luminescence could be recorded as previously described [124, 125]. The values of lifetime were derived by a bi-exponential curve fitting (Origin 6.0 software) with the residual error function X^2 value of less than than 1.0. In the time-gated fluorescence bioimaging application, the images of cells labeled with europium chelate were recorded using a NIS-Elements BR 300 CCD camera (Nikon Instruments Inc. USA) at 1 second per frame. The imaging was performed using 20 times (NA-numerical aperture=0.40) and 40 times (NA=0.65) objectives and the time-gating was achieved by using mechanical chopper (C995 Optical Chopper from Terahertz Technologies) operating at 2.5 kHz and positioned before CCD camera. This chopper was also acting as a trigger for the pulsed UV LED. The collected colour images were analyzed using only red channel whose spectral width overlaps with the 615 nm emission of BHHCT$-Eu^{3+}$. All measurements were performed in the dark at room temperature.

Results and discussion

As with any new fluorophores, it is informative to quantify their labeling efficiency. To this aim we took the absorption spectrum of the conjugates of SA-BSA with BHHCT (see Fig. 8.4). It has one peak at a wavelength of about 342 nm which is almost identical in pure BHHCT (dotted line in Fig. 8.4), and another peak at about 284

nm wavelength that results from absorption in SA-BSA (dashed line in Fig. 8.4). The absorbance at 342 nm was used to determine how much BHHCT was bound to SA-BSA by using the following equation:

$$A_{342BHHCT} = \varepsilon b C_{BHHCT} \tag{5.1}$$

where $A_{342BHHCT}$ is the absorbance of BHHCT at 342 nm, ε is the molar extinction coefficient for BHHCT, b is the optical path length (cuvette size) and C is the molar concentration of BHHCT during the measurement. This relationship made it possible to determine the labeling ratio between proteins and BHHCT. In our experiment, we achieved the labeling ratio between BHHCT and SA-BSA of about 28:1. Such labeling ratios, as high as 20:1 or more are highly desirable to achieve sufficiently bright immunoconjugates, however high labeling ratio may compromise the binding affinity. However we were able to confirm that despite the high labeling ratio, BHHCT – Eu^{3+} labeled immunoconjugate prepared by this protocol retained sufficient activity and non-specific binding was very limited, as shown in further experiments.

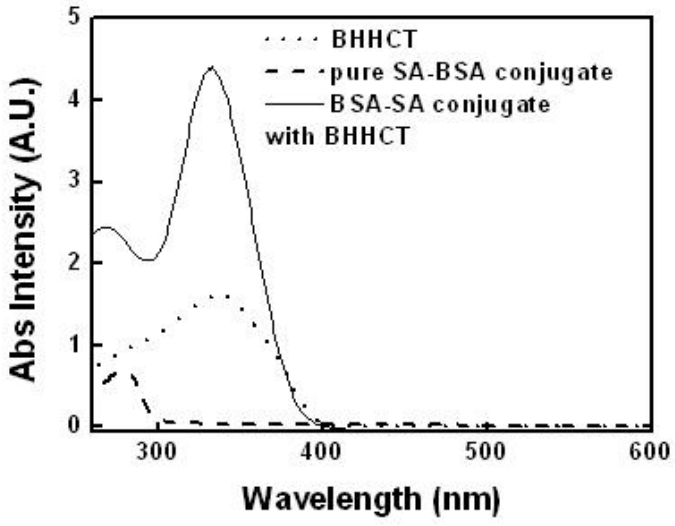

FIGURE 5.4: Absorption spectra of pure BHHCT, SA-BSA conjugates and SA-BSA conjugates with BHHCT (from top to bottom).

The SEM images of beads prepared with 10 sec, 1 min, 3 min and 5 min silver enhancing time, respectively are shown in Fig. 8.5. As expected, silica beads with 3

min silver enhancing had a much higher and more even silver coverage compared to beads with a shorter silver enhancing time. On the other hand, longer enhancing times were causing the formation of nanoparticle clusters. In such clusters, where particles are in close proximity the coupling of the neighboring particles plays an important role, and it modifies the dipole-dipole interaction between the dipole moments of the coupled particles. This dipole coupling concept has been successfully applied to the modeling of the optical properties of the silver fractal clusters.

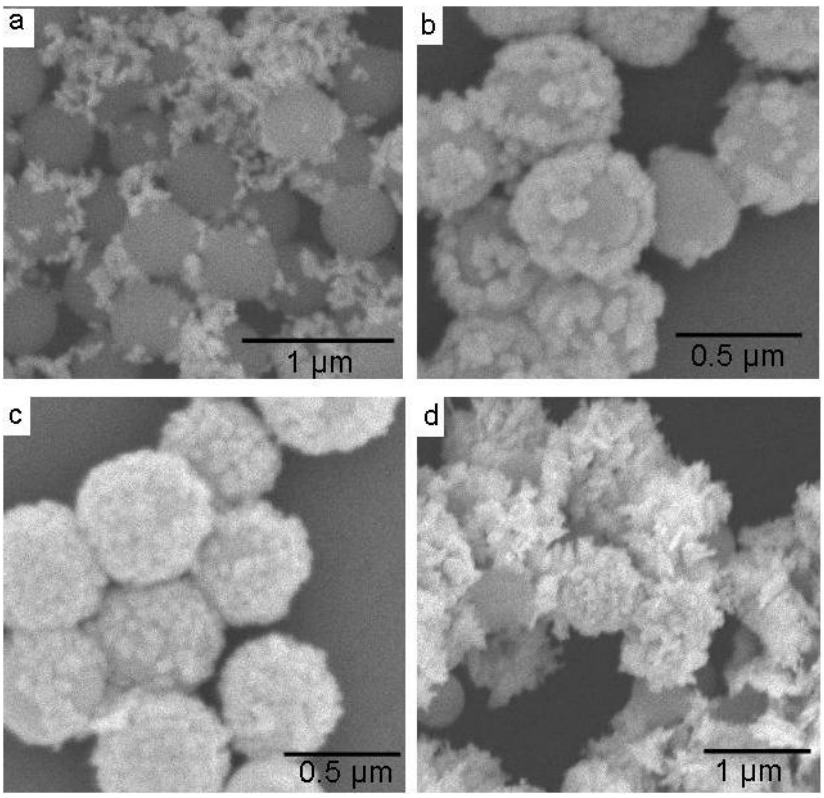

FIGURE 5.5: SEM images of silica beads at different Ag enhancing times (a) 10sec, (b) 1 min, (c) 3 min and (d) 5 min.

Now we discuss the first of our key results, the demonstration of fluorescence enhancement of BHHCT – Eu^{3+} by using metal nanostructures in an IgG assay. We checked that the metal nanostructures do not change the spectral shape of the emission. Indeed, in the samples with and without the Ag nanostructures as shown in Fig. 8.6, we were able to observe a very similar spectrum, with the emission maximum typical of Eu^{3+} centered around 615 nm. The metal nanostructures clearly enhance

fluorescence, and we observed a slightly different enhancement factor for glass slides with Ag nanostructures (see Fig. 8.6a) and silica beads with Ag nanostructures (see Fig. 8.6b) as substrates. For the Ag-coated glass slides, the average enhancement factors with 10 sec, 1 min and 3 min Ag enhancing time were about 1.73, 4.81 and 9.08, respectively. These values were obtained by dividing the fluorescence peak fluorescence intensities for samples with silver nanostructures after background subtraction (fluorescence from the silvered structures without immunoassay) by the fluorescence intensity on glass slides without silver but with the same assay. For the Ag-coated silica beads, the calculation process of enhancement factors was more complicated. We firstly measured the fluorescence intensities from BHHCT $-$ Eu^{3+} on the silica beads and in the supernatant for each sample as well as the original BHHCT $-$ Eu^{3+}-labeled SA-BSA solution under the same experimental conditions (see Fig. 8.7). This measurement was repeated 8 times for each sample, for improved accuracy of the results. Subsequently, we estimated how much SA-BSA was attached to the silica beads with and without the Ag nanostructures, respectively, by the following calculation. By subtracting the fluorescence intensity from supernatant of each sample from one of the original BHHCT $-$ Eu^{3+}-labeled SA-BSA solution, we estimated how much SA-BSA was bound to each sample. This value was divided by the amount of the original BHHCT $-$ Eu^{3+}-labeled SA-BSA solution. We thus obtained the corresponding binding efficiency for each sample, indicating the amount of SA-BSA remaining on the silica beads surface. Then we divided the observed fluorescence intensity from the wells for each sample by its corresponding binding efficiency and thus obtained the corrected fluorescence intensity. This value was equivalent to fluorescence intensity for the uniform coverage on each glass slide for the different samples. Finally, we compared the corrected fluorescence intensities from BHHCT $-$ Eu^{3+} on silica beads with Ag enhancement and on unmodified beads and obtained the corresponding enhancement factors for the different Ag enhancement times.

Since silica beads in the well tend to produce non-uniform coverage and the number of measured beads in each of the well may not be exactly the same in each of the sample studied. In this case, the average enhancement factors with 10 sec, 1 min and 3 min Ag

enhancing time were about 2.70, 7.04 and 11.27, respectively. It is interesting to note that the enhancement factors for the sample with 3 min Ag enhancement using glass slides as substrates was somewhat lower compared to the corresponding sample with the silica beads. The possible reason is that the larger surface area of silica beads and its curvature leads to an increased density of deposited Ag nanostructures as compared to deposited on glass slides and this effect results in observed stronger enhancement of BHHCT – Eu^{3+} emission for slides with silvered beads.

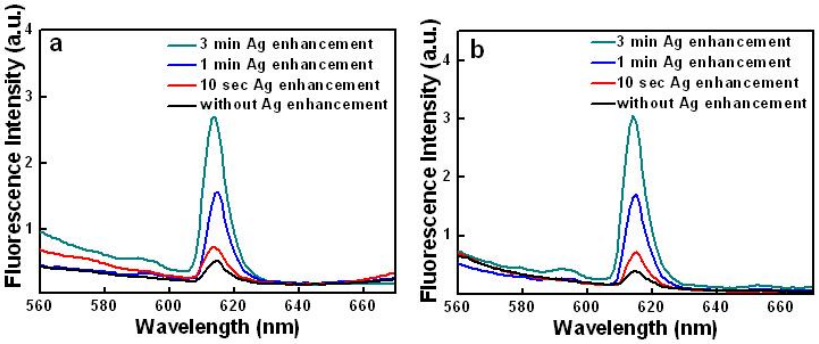

FIGURE 5.6: Fluorescence intensities measured from the glass slides (a) and silica beads (b) with different Ag enhancing time and without Ag (from top to bottom: 3 min, 1 min, 10 sec and without Ag enhancement).

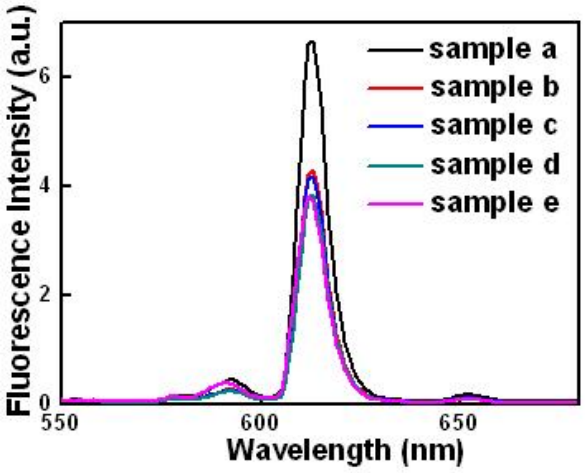

FIGURE 5.7: Fluorescence intensities measured in supernatants (sample a: original BHHCT – Eu^{3+}-labeled SA-BSA solution; sample b: without Ag enhancement; sample c: 10 sec Ag enhancement; sample d: 1 min Ag enhancement; sample e: 3 min Ag enhancement).

To evaluate the non-specific binding of BHHCT – Eu^{3+} labeled SA-BSA conjugates

on Ag-coated silica beads, a control experiment was carried out where pure goat anti-mouse IgG antibody instead of a biotin-labeled one was added to each well coated with silica beads with Ag nanostructures (for each Ag deposition times: without Ag deposition, 10sec, 1 min and 3 min, respectively). By comparing the maximum fluorescence intensity from $BHHCT-Eu^{3+}$ in the assay described in the experimental section and a control experiment, we established that the level of non-specific binding was very low, of about $4.0 \pm 0.3\%$ for each sample (see Fig. 8.8).

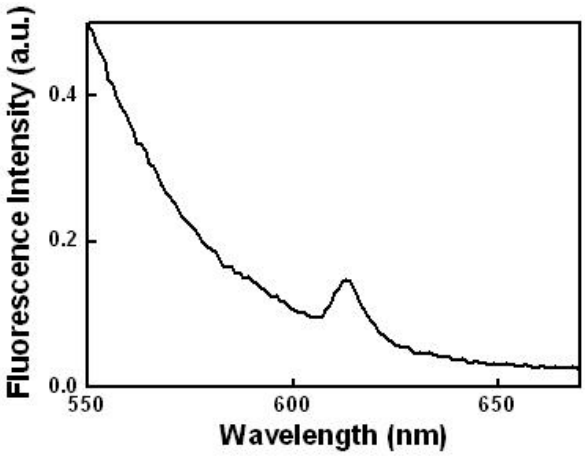

FIGURE 5.8: Fluorescence spectrum from $BHHCT - Eu^{3+}$on the silica beads with 3 min Ag enhancement after non-specific binding under the same experimental conditions.

For a more complete characterization of the effect of metal nanostructures on the fluorescence we carried out the measurements of fluorescence lifetimes. As discussed in the literature [108], metal enhanced fluorescence is characterized by an increase in the quantum yield and a decrease in the lifetime of a fluorophore located in the proximity of the metallic nanostructures. The fluorescence lifetime provides unambiguous confirmation of the metal-induced fluorescence enhancement. The measured decay curves of $BHHCT - Eu^{3+}$ on the glass slides (Fig. 8.9a) and glass slides with silica beads (Fig. 8.9b) with silver enhancement for 10s, 1 min and 3 min and control samples without silver indicate a clearly decreased fluorescence lifetime observed in the presence of the silver nanostructures near $BHHCT - Eu^{3+}$. These decay curves were fitted by a double exponential function with two lifetime components. Their values and the average lifetimes for different samples are shown in Table 5.1. The table shows that in

the case of the planar format where Ag nanostructures were formed on the glass slide, the lifetime was reduced from 382 μs without Ag enhancement to 232 μs with 3 min Ag enhancement. On Ag-coated silica beads the lifetime of BHHCT – Eu^{3+}complex is reduced from 380 μs without Ag enhancement to 196 μs with 3 min Ag enhancement.

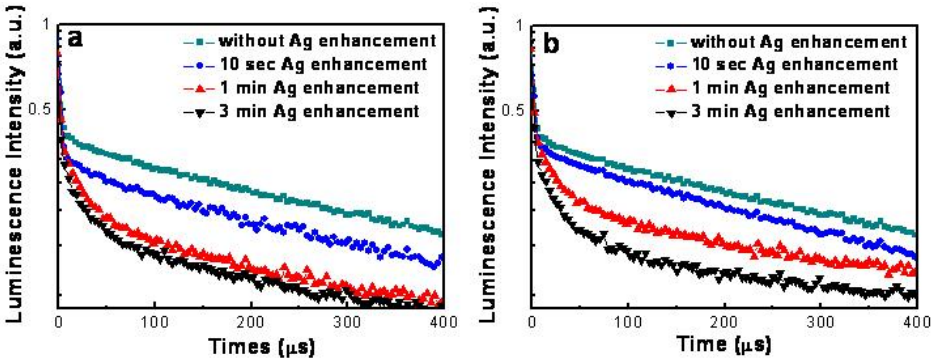

FIGURE 5.9: Representative fluorescence lifetime decay curves of BHHCT – Eu^{3+}-labelled assay measured on the glass slides silica beads (a) and silica beads (b) with and without Ag enhancement steps.

TABLE 5.1: Fluorescence intensity decay analysis. $\tau_{1,2}$ denotes decay times of the two lifetime components, τ is the average lifetime.

substrate	sample	$\tau_1(\mu s)$	$\tau_2(\mu s)$	$\tau(\mu s)$
	without Ag	382±4	45±2	382±2
glass slides	10 sec Ag	372±3	37±3	372±3
	1 min Ag	245±2	38±4	240±3
	3 min Ag	232±3	23±3	227±3
	without Ag	380±2	36±2	380±2
silica beads	10 sec Ag	363±2	26±2	363±2
	1 min Ag	253±1	22±2	250±1
	3 min Ag	196±3	23±3	192±3

The lifetime results make it possible to investigate the impact of silver nanostructures on the excitation and emission enhancements individually. These two contributors are important because the enhancement of fluorescence observed on the nanostructured

silver surfaces is a result of two effects: an increase of a local electromagnetic field near silver nanoparticles, leading to increased excitation rate of fluorophores and an increase of the radiative decay rate Γ of fluorophores close to metal nanostructures, reflected both in the fluorescence lifetime and quantum yield [1]. The local electromagnetic field enhancement produces a higher excitation rate but it does not change the lifetime of the fluorophore; this effect is referred as excitation enhancement (E_{ex}). The second effect referred as emission enhancement (E_{em}), increases the quantum yield and reduces the lifetime of the fluorophore [126]. The lifetime (τ) of the fluorophore in the free-space condition is given by [1]:

$$\tau = \frac{1}{\Gamma + k_{nr}} \tag{5.2}$$

where Γ and k_{nr} are the radiative and nonradiative decay rate, respectively. The value of k_{nr} is typically affected by a fluorophore's environment, which may induce quenching or fluorescence resonance energy transfer (FRET) [1], whereas the radiative decay rate Γ is an intrinsic property of a fluorophore. These allow us to calculate the fluorescence quantum yield (Q), which is the ratio of the radiative rate to the total decay rate

$$Q = \frac{\Gamma}{\Gamma + k_{nr}} \tag{5.3}$$

The proximity of fluorophore to metals results in an increase in the total radiative decay rate by addition of a new rate Γ_m to the emission rate Γ_m applicable to the free space conditions [1]. The modified fluorescent lifetime (τ_m) and quantum yield (Q_m) are then given by

$$\tau_m = \frac{1}{\Gamma + \Gamma_m + k_{nr}} \tag{5.4}$$

$$Q_m = \frac{\Gamma + \Gamma_m}{\Gamma + \Gamma_m + k_{nr}} \tag{5.5}$$

The effect of proximity of the metal on k_{nr} is negligible [126]. By using the measured fluorescence lifetime ratios of BHHCT $-$ $Eu^{3+}$with and without Ag enhancement (Eqs

(5.2) and (5.4)) and using the quantum yield of BHHCT – Eu^{3+} in free-space conditions of 0.27 [127]) (Eq (5.3)), we were able to obtain the value of Γ_m/Γ and hence the emission enhancement, defined as $E_{em} = Q_m/Q$, for each sample. These are listed in Table 5.2. The excitation enhancement for each sample is calculated by dividing the (total) fluorescence enhancement factor (E_t) by the emission enhancement. It is given by

$$E_{ex} = \frac{E_t}{E_{em}} \tag{5.6}$$

The values are listed in Table 5.3.

TABLE 5.2: Lifetime measurements for each sample and the calculated values of rate (Γ/Γ_m), yield ratios (Q_m/Q), and modified quantum yield (Q_m); τ is the average lifetime value of the control sample (380 ms for the silica beads and 382 ms for the glass slides); τ_m is the modified lifetime; Q is the average quantum yield of the control sample (0.27).

substrate	sample	τ_m	τ/τ_m	Γ/Γ_m	$Q_m/Q = E_em$	Q_m
	10 sec Ag	372± 3	1.03± 0.4	0.11± 0.2	1.08 ± 0.2	0.29 ± 0.02
glass slides	1 min Ag	240± 3	1.59± 0.4	2.19± 0.3	2.01 ± 0.2	0.54 ± 0.03
	3 min Ag	227± 6	1.68± 0.6	2.53± 0.2	2.10 ± 0.3	0.57 ± 0.03
	10 sec Ag	363± 2	1.05± 0.4	0.19± 0.2	1.13 ± 0.2	0.30 ± 0.03
silica beads	1 min Ag	250± 1	1.52± 0.2	1.93± 0.3	1.92 ± 0.3	0.52 ± 0.04
	3 min Ag	192± 3	1.98± 0.5	3.63± 0.3	2.34 ± 0.4	0.63 ± 0.04

The results shown in the Table 5.2 indicate τ/τ_m values increase from 1.03 to1.68 with increasing Ag enhancing time. Consequently, with increasing Ag enhancement time the emission enhancement and excitation enhancement factors increase from 1.08 to 2.1 (see Table 5.2) and from 1.60 to 4.33 (see Table 5.3), respectively, and are highest for 3 minutes of Ag deposition time. For the silica beads with and without Ag nanostructures, we obtained similar results (Table 5.2 and Table 5.3). Specifically, τ/τ_m, E_{em} and E_{ex} increase from 1.05 to 1.98, 1.13 to 2.34 and 2.39 to 4.82, respectively. The data show that both the emission and excitation enhancement increase, but to a

TABLE 5.3: Values of the excitation enhancement (E_{ex}) and emission enhancement (E_{em}) for each sample. E_t is the calculated enhancement factor for each sample.

substrate	sample	E_t	E_{em}	E_{ex}
	10 sec Ag	1.73± 0.4	1.08± 0.2	1.60± 0.2
glass slides	1 min Ag	4.81± 0.5	2.01± 0.2	2.40± 0.3
	3 min Ag	9.08± 0.7	2.10± 0.3	4.33± 0.3
	10 sec Ag	2.70± 0.5	1.13± 0.2	2.39± 0.2
silica beads	1 min Ag	7.04± 0.6	1.92± 0.3	3.66± 0.4
	3 min Ag	11.27± 0.4	2.34± 0.4	4.82± 0.4

different extent. The extent of the excitation enhancement is much larger than that of the emission enhancement, which we attribute to the following effect. When the interparticle distances are reduced, the enhancement of local electromagnetic fields becomes strong [128], which magnifies the excitation enhancement induced by these nanostructures. In our previous studies, the silver nanostructures on both the surface of glass slides and silica beads were very close to each other, resulting in the strong coupling effect between nanostructures. This coupling effect has a strong effect on the exciting electromagnetic filed.

The photostability of fluorophores is a primary concern in many applications of fluorescence, particularly for bio-imaging and single-molecule studies [110, 129, 130]. Fortunately, both decrease in the fluorescence lifetime and increase in the quantum yield lead to a significant reduction of photodegradation. First, a reduced lifetime in the presence of silver leads to a greater fluorophore photostability, as fluorophores spend less time in an excited state (reduced lifetime) and are therefore less prone to photooxidation, the major photodestruction pathway for fluorescent probes [110]. Second, the increase in quantum yield diminishes bleaching because it allows a decrease of the excitation light intensity needed to maintain the same signal intensity. A comparison of photostabilities observed in BHHCT$-$Eu^{3+} on the silica beads with and without Ag enhancement is shown in Fig. 8.10. During the photobleaching experiments the

fluorescence intensity was measured at 5 min intervals for 1 h. We found that under intense illumination with 350 nm light for 1 h (from a 450W Xe lamp through a monochromator with 8 nm spectral width) the fluorescence intensity of BHHCT – Eu^{3+} without Ag enhancement was reduced by 65%, while BHHCT – Eu^{3+} with Ag enhancement was bleached just by 20%, indicating that photostability for BHHCT – Eu^{3+} is improved by at least 3.2-fold by silver nanostructures. This extends the time available for signal acquisition by over three times, offering improved imaging conditions for the cells or tissues.

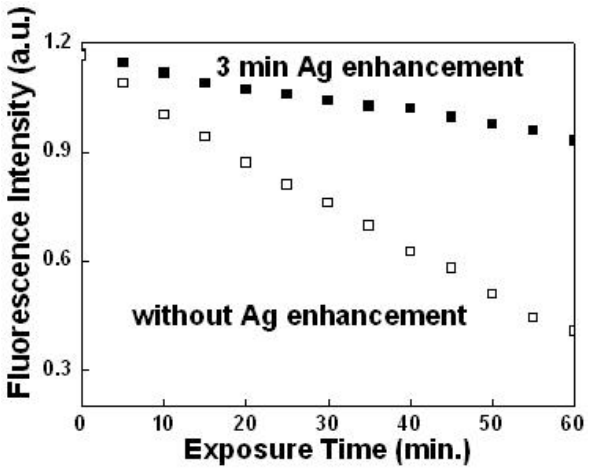

FIGURE 5.10: Photostability comparison of BHHCT – Eu^{3+}-labelled assay with and without Ag enhancing step with power adjusted to provide the same initial fluorescence intensity.

To demonstrate beneficial effects of enhanced fluorescence by silver nanostructures for cell imaging, we used a model microorganism Giardia lamblia where BHHCT – Eu^{3+} labeled SA-BSA conjugate was attached to the cell surface. Based on our earlier finding that the enhancement factor for the silica beads with Ag nanostructures was higher compared to that for the glass slides with Ag nanostructures, we used silica beads (with and without Ag nanostructures) to evaluate the signal enhancement factor in the imaging experiment. This requires an appropriate approach as the cells have different sizes and shapes and also the labeling of each cell tends to be nonuniform. We have therefore collected signals from a number of cells to obtain statistically meaningful results. In order to eliminate the effect of variability of cell shapes, sizes and

local variations of labeling efficiency, the image pixel intensity distribution was investigated on both Ag-coated and uncoated regions using the ′histogram′ function of ImageJ (W.S. Rasband, ImageJ, U.S. National Institute of Health, Bethesda, MD, http://rsb.info.nih.gov/ij/). From the corresponding intensity histogram, we found the mean image signal is enhanced by a factor of 2. The representative cell images with and without Ag enhancement were also respectively recorded (see Fig. 8.11).

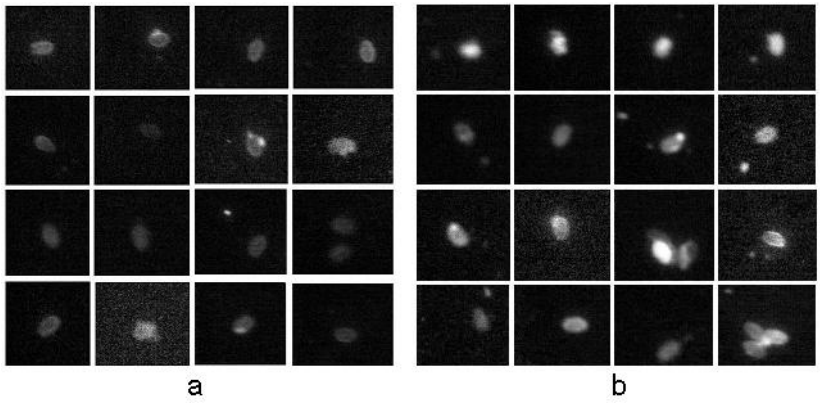

FIGURE 5.11: Representative images of Giardia lamblia stained by BHHCT$-Eu^{3+}$ without Ag enhancement as reference (a) and with 3 min Ag enhancement (b). All the images were collected under the same experimental conditions.

We now discuss the reasons for the lower enhancement factor obtained from the cell imaging in this study than that obtained in immunoassay. It is known that the fluorescence enhancement is most pronounced only when the fluorophore is localized at an optimal distance close to the surface of metal nanostructures that is in the range of 5-30 nm [51, 131]. However, when a fluorophore was labeled on the biological cell the distances of fluorophore molecules to metal nanostructures covered a much wider range. The excitation enhancement is thus averaged over the cell thickness, resulting in the lower enhancement. In addition, emission enhancement plays an important role for the very thin samples. However, the strength of emission enhancement decreases as the distance from the metal nanostructures increases [132]. Therefore, the observed signal enhancement for cell imaging is mainly caused by the increase of the fluorophore excitation rate. Another important issue for cell-imaging is the fluorescence collection efficiency. The emission distribution is much larger at wide angles when a thick sample is employed. The collection efficiency is thus limited when light is collected through

an objective lens of low NA. Despite these challenges we believe the fluorescence enhancement in imaging can be further optimized to achieve higher values. This will be reported separately.

Conclusions

The fluorescence enhancement of the europium chelate (BHHCT – Eu^{3+}) induced by silver nanostructures was observed and investigated. The fluorescence spectra of BHHCT – Eu^{3+}-labeled SA-BSA on the silver nanostructures show a varying level of fluorescence enhancement depending on silver deposition times. The origin of the observed enhancement is attributed to an increased excitation rate from the local field enhanced by the interaction of incident light with nanostructures and higher quantum yield from the increase of the intrinsic decay rate of the fluorophore. Both the emission and excitation enhancement contributed the total enhancement values on the order of 11 for the silica beads and 9 for the glass slide demonstrated here, which was respectively accompanied by 2 times and 1.7 times decrease of the lifetime. From the application point of view, both substrates have the potential for fluorescence enhancement assays, including the solution-based assays analyzed by flow cytometry. Moreover, we have also shown that silica beads with Ag nanostructures were able to produce brighter fluorescence images of cells labeled by BHHCT – Eu^{3+}, suggesting that such substrates are applicable in the time-gated fluorescence bio-imaging. These important features will pave the way for application of such enhanced lanthanide chelates in many areas of life sciences and biotechnology such as fluorescence-based biological assays and bio-imaging.

6

Upconversion Phosphor Nanoparticles and its Application in Bioassays (review)

6.1 Introduction

Phosphors that emit lower energy photons when excited by higher energy photons can be described as down-conversion phosphors. For example, ZnS : Mn and Y_2O_3 : Eu, are well-known down-conversion phosphors. On the other hand, phosphors that emit higher energy photons after absorbing lower energy excitation photons are referred to upconversion phosphors (UCP). They absorb two or more pump photons via intermediate long-lived energy states followed by the emission of the output radiation at a shorter wavelength than the pump wavelength, which is referred to as upconversion. This general concept was first recognized and formulated independently by Auzel, Ovsyankin, and Feofilov [133, 134]. Different rare earth ions can produce upconversion

luminescence at various emission wavelengths characteristic to the lanthanide ion with a single near-infrared excitation wavelength. Due to the fact that several photons participate in the upconversion process, the photoluminescence response to excitation is nonlinear and strongly enhanced by higher excitation intensity until saturation is observed [135, 136]. In general, when n photons are involved in the upconversion process, an n-th order dependence of the emission intensity on the excitation power is observed. The real upconversion mechanism, however, is slightly more complex, involving several competing processes, such as sequential energy transfer, excited state absorption, and phonon interaction [136–138].

Upconversion photoluminescence is exceptional in that no biological material produces anti-Stokes photoluminescence at visible wavelengths under conventional near-infrared excitation light intensity, and thus, upconversion luminescence can be measured entirely free of autofluorescence [139]. The observed background is from dark current of the detector (e.g., dark counts in photomultiplier tube). In addition, an upconversion process is much more efficient in comparison to two-photon absorption because of an existing intermediate energy level due to which upconversion process is sequential, as opposed to a virtual intermediate level in the case of two-photon absorption, where the process is simultaneous. Thus an upconversion process requires much lower excitation intensity that allows the use of inexpensive and readily available continuous wave (CW) laser diodes against expensive femtosecond pulsed lasers needed for simultaneous two-photon excitation [140, 141]. UCP as such are also relatively inexpensive to manufacture, but their production as nanosized water-dispersible particulates and further conjugation provides yet considerable challenges similar to those encountered with fluorescent nanocrystals(quantum dots) [142]. The shelf life of UCP is essentially infinite, and because the up-conversion occurs within the inorganic host lattice, their optical properties are rather insensitive to environmental conditions. UCP also withstand repeated high-intensity laser excitation, as they are not susceptible to photobleaching [141, 143, 144]. Due to their extraordinary photoluminescence characteristics, UCP have become the attactive reporters for sensitive detection of biomolecules recently [145–152].

6.2 UC materials and upconversion mechanism

6.2.1 UC materials

Inorganic cystals in most cases do not exhibit upconversion luminescence at room temperature. Therefore, research is mainly directed to systems that are composed of a crystalline host and lanthanide dopants added to the host lattice in low concentrations [153]. The dopants are usually in the form of localized luminescent centers. The host lattice is typically composed of a transparent crystalline material involving fluorides, oxides, chlorides, and bromides, as well as oxysulfides, or oxyhalides, all capable of incorporating significant amounts of dopants, for example, Pr^{3+}, Nd^{3+}, Dy^{3+}, Ho^{3+}, Er^{3+} and Tm^{3+} [154–156]. Such dopant ions are typically trivalent lanthanides with the advantage of having multiple, long-lifetime excited states, which is the basic requirement for generating upconversion photoluminescence. UCP containing only one type of rare earth ion as the dopant, such as Er^{3+} or Tm^{3+}, are capable of anti-Stokes photoluminescence, but the upconversion processes can be more efficient when Yb^{3+} is also present [133]. Typically, Yb^{3+} serves as the absorber ion due to its higher absorption coefficient, that is, it absorbs the incoming low-energy photons, and the other dopant, such as Er^{3+}, Tm^{3+}, Ho^{3+}, Tb^{3+}, or Pr^{3+}, acts as the emitter ion, emitting the single, higher-energy photon after the up-conversion process. The most efficient upconversion materials known to date are $NaYF_4 : Er^{3+}/Yb^{3+}$ and $NaYF_4 : Tm^{3+}/Yb^{3+}$ [137, 157]. Although upconversion can be expected in principle from most lanthanide-doped crystalline host materials, efficient up-conversion only occurs by using a small number of well selected dopant-host combinations (see Table 6.1).

6.2.2 Upconversion mechanism

A variety of different upconversion mechanisms are well established and several review articles have appeared in the literature [158–160]. The majority of these involve absorbtion and nonradiative energy transfer steps. Here we mainly focus on the the two prominent and basic ones. The simplest single-ion up-conversion mechnism is the so-called ground-state absorption/excited-state absorption (GSA/ESA) mechanism, shown in Fig. 9.1(a). In the GSA step, the ion is excited into the intermediate metastable state $|1>$. Subsequently, an ESA step promotes the ion to the higher-lying

excited state $|2>$, from which light is emitted. Since both steps must occur within the (short) laser pulse, the time dependence of the luminescence intensity directly after the excitation pulse will show a single exponential decay corresponding to the lifetime of the emitting level, as can be seen in Fig. 9.1(b).

The second well-known upconversion mechanism is referred to as energy-transfer upconversion, or ETU, and is schematically indicated in Fig. 9.1(c). In the GSA step two ions are excited into their intermediate excited levels $|1>$, by the sequential absorption of two photons. The upconversion step is based on a nonradiative energy-transfer between the two ions: one ion is promoted to its upper excited state $|2>$, while the other one simultaneously relaxes to the ground state $|0>$. Overall in both these schemes, two excitation photons are converted into one emitted photon of higher energy. A feature of an ETU process is a rise in the upconversion transient after short-pulse excitation, see Fig. 9.1(d). The population of the emitting level rises after the short excitation pulse as the typical time associated with the ETU step is much longer than the 10 ns excitation pulse. The upconversion rise and decay times are correlated with the decay rate constants of the intermediate state, the upper excited state and the energy transfer rate constant.

In most cases upconversion is a two-photon process which can be identified by a quadratic dependence of the number of upconverted photons on the excitation power. However, three-photon or higher-order upconversion processes also occur [162]. Fig. 9.2 typically illustrates a two-photon up-conversion process in which the absorber (Yb) sequentially absorbs two photons of IR. The two-photon upconversion excitation mechanism can be described here in detail. A Yb^{3+} ion in ground state $^2F_{7/2}$ absorbs a photon and transits to excited state $^2F_{5/2}$, and then it drops back to the ground state while transferring the energy to an adjacent Er^{3+} ion. This Er^{3+} ion is excited to $^4I_{11/2}$ and can rise to the $^4F_{7/2}$ state by absorption of a second IR photon from a surrounding Yb^{3+} ion ($^2F_{5/2}$). After phonon relaxation, the excited (double pumped) Er^{3+} ion transit to the ground state and emit red light. This is two-photon process. Other emitter ions (dopants) such as Tm^{3+} undergo a mechanism of upconversion that is fundamentally different than the one illustrated in Fig. 9.2a. This is a three-photon upconversion

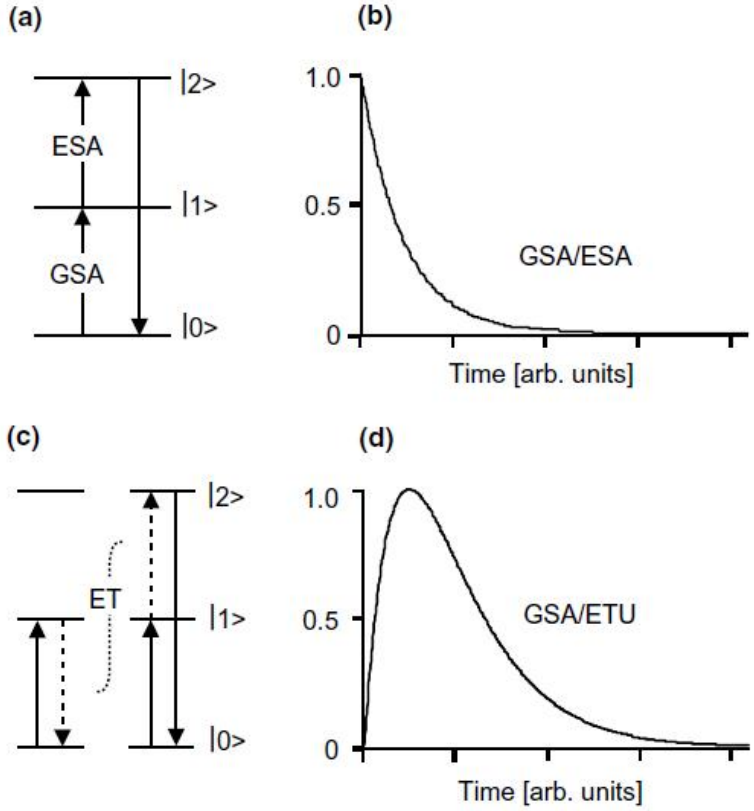

FIGURE 6.1: Schematic representation of the most prominent upconversion mechanisms: ground-state absorption (GSA), excited-state absorption (ESA) and energy transfer upconversion (ETU), respectively. The dotted arrows represent nonradiative energy transfer (ET) processes. The straight arrows indicate radiative transitions. The transients indicated in (b) and (d) describe the time-evolution of the emission of the upconversion luminescence after a short excitation pulse, adopted from [161]

illustrated in Fig. 9.2b. The Yb^{3+} ion sensitises the IR light in a $^2F_{7/2} \rightarrow {}^2F_{5/2}$ transition, and then transfers an IR photon to a nearby Tm^{3+} ion, exciting it from $^3H_6$ to $^3H_5$ in a phonon-assisted energy transfer. Following a phonon relaxation to $^3H_4$, the excited Tm^{3+} ion receives the second photon by another phonon-assisted energy transfer, reaching to $^3F_3$. With the second phonon relaxation to $^3F_4$, the Tm^{3+} ion is further excited with the third phonon-assisted energy transfer to $^1G_4$, and subsequently transit to the ground state and emit blue light. There exist multiple relaxation states and series of radiative and non-radiative energy transfers that are possible in the case of three-(or more) photon upconversion.

6.3 Synthesis and surface mordification of UC nanoparticles

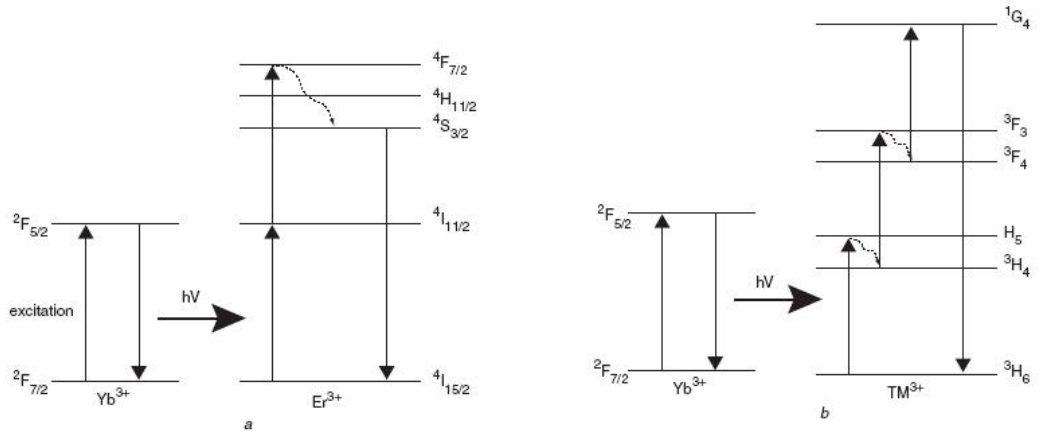

Figure 6.2: Principal of the two-photon up-conversion process (a) and three-photon up-conversion (b), adopted from [163]

6.3.1 Synthesis of UC nanoparticles

During the last years, as the interest in utilizing UCP as reporters in bioanalytical assays has increased, nanosized phosphors have been synthesized using different methods: for example by combustion synthesis [164, 165], a sol-gel method [166–168], a hydrothermal method [169], co-precipitation [170, 171] or a thermal decomposition [172–175]. Combustion synthesis can be referred to as a controlled explosions in reactions, with which the UC nanomaterials can be produced in mintues. Once intiated by a heat source, highly exothermic reactions with temperatures ranging typically from 500 to 3000^{o}C occur in the form of a combustion wave that propagates through the reaction materials in a self-sustained manner without requiring additional heat. This method represents one of the attractive techniques to synthesize a wide variety of oxide and oxysulfide upconversion nanomaterials reported by the groups of Capobianco, Luo, and Zhang [176–178].

The sol-gel process provides UC nanoparticles for applications such as thin film coating or glass materials. It is characterized by the hydrolysis and polycondensation of metal alkoxide (or halide) based precursors. Although it shows some advantages such as high homogeneity of material, low processing temperature and using simple equipments, this method derived nanoparticles are not particularly suitable as luminescent probes for biological assays due to lack of partile size control and considerable

aggregation of the particles when dispersed in aqueous solutions.

The hydrothermal method usually involves mixing a rare-earth precursor with a fluoride precursor in aqueous solution, heating it and then separating out the precipitated product [179, 180]. This approach was allows for the preparation of highly crystalline material at much lower temperatures and without the need for a heat treatment. In order to obtain a product with improved crystality, the reagents are placed in an autoclave (often Teflon-lined to prevent fluoride ions attacking glass) and then sealed and heated. Most groups, when using the hydrothermal method to synthesise lanthanide fluoride nanoparticles, use lanthanide nitrates as precursors, often synthesising the nitrate precursor in situ from oxides and nitric acid. Some groups used chlorides and fewer still the oxides directly. The choice of fluoride precursor varies much more than lanthanide precursors. Groups mainly use HF, NH_4F and NH_4HF_2 when preparing fluorides of the type LnF_3 and NaF or KF for fluorides of the type $MLnF_4$. Other, less frequently used, precursors include $NaBF_4$, KBF_4 and 1-butyl, 2-methylimidazolium tetrafluoroborate (an ionic liquid).

Co-precipitation is simple and convenient, and permits UC nanoparticles to be prepared in tunable size and narrow size distribution. Compared to other techniques, there is no need for costly equipment, stringent reaction conditions, and complex procedures, resulting in less time consumption. This method was refined by Chow and co-workers [181], who synthesized upconversion LaF_3 nanoparticles with smaller particle size ($\sim$5 nm) and narrower size distribution from simple water soluble inorganic precursors. In their studies, synthetic ammonium di-noctadecyldithiophosphate was used as a capping ligand to control particle growth and to stabilize the nanocrystals against aggregation. These sub-10 nm nanoparticles can be redispersed in solutions, offering promising applications as luminescent probes for biomolecules with dimensions from several nanometres to tens of nanometres.

In addition, a more interesting route to generate UC nanoparticles is based on the decomposition of rare-earth trifluoroacetate salts (LnTFA). Possible advantages of this method over other types of synthetic methods include the ability to create nanoparticles with controlled crystal sizes and good dispersibility in solutions. Disadvantages

of the method include the safety concerns brought up from high temperature and the enviromental issues caused from by-products (HF, NH_4F, NH_4HF_2 et al). To the best of our knowledge the first group to use the trifluoroacetate-based precursor to synthesis rare-earth fluoride nanoparticles was Yan's group [172]. Using lanthanum trifluoroacetate and a mixture of oleic acid and octadecene as solvent, the group made trigonal LaF_3 triangular nanoplates which were highly monodisperse and had the tendency to self-align both side-down and face-down. The nanoparticles were also highly crystalline and dispersible in organic solvents. The reaction temperature and time were 280 ^{o}C and 1 h. Not long after Yan's group published the use of trifluoroacetate salts as precursors for rare-earth fluoride nanoparticles, another group from Moscow State University published the synthesis of europium fluoride [182, 183]. This synthesis used trioctylphosphine oxide (TOPO) as the solvent and capping ligand and so gave different morphologies to Yan's method. These particles were small and were approximately spherical in shape, although not as crystalline as those produced by Yan's group. In 2007, another group also attempted to use TOPO as the solvent when synthesising $NaYF_4$ using trifluoroacetate precursors [173]. The resulting particles were not only crystalline and monodisperse but also in the hexagonal phase. The particles were also small enough to be used as biological labels (around 11 nm). TOPO has a higher boiling point than the usual three solvents used in trifluoroacetate syntheses so it has the potential to produce the hexagonal phases of this class of material with much more ease.

In conclusion, lanthanide-doped upconversion nanoparticles with controlled size and morphology can be prepared by one or a combination of these methods. Optimization of the synthesis or fabrication procedure is critical to obtain nanocrystals with tailored crystal size, morphology, chemical composition, surface functionalization, and optical properties.

6.3.2 Surface modification and functionalization of UC nanoparticles

The UC nanoparticles usually are applied to biological applications requiring the aqueous solution. Additionally, the lack of toxicity is another important issue if these UC nanoparticles are used in *vivo*. Moreover, there are no functional groups on these

UC nanoparticles surface, where biomolecules could be covalently coupled using standard conjugation chemistries [184]. Therefore, different strategies for surface modification and functionalization were widely investigated by several groups, which enable these nanoparticles a kind of promising biolabels in biological applications.

The surface silanization technique was one of widely used methods so far. This can be performed in either of the following ways: firstly, direction reaction between a silaning reagent and the particles to form a silane-modified surface, or secondly, coating the surface with tetraethoxysilane (TEOS) to first produce a layer of silica and coating this layer with a silaning reagent [185, 186]. The merits of this coating method are as follows [187, 188]:

1) Silica layer does not affect the optical property of nanoparticles since it is translucent

2) Dispersing and stability of nanoparticles in the solution will be greatly improved after coating with silica

3) Silica coating the particles provides a surface that can be functionalized in several ways, utilizing well-known techniques. Amino-, carboxyl-, and sulthvdryl functional groups can be incorporated during the silication process using the silane derivatives.

As an alternative to silanization, ligand attraction was another way for the surface mordification. This involves absorption of an additional amphiphilic block copolymer onto the nanoparticle surface through the hydrophobic attraction between the original ligand and hydrocarbon chain of the polymer [189–191]. The hydrophilic outer block of the polymer permits aqueous dispersion and further bioconjugation. For example, amphiphilic copolymers such as poly(acrylic acids)and poly(allyamine)are used to replace the original hydrophobic ligands on the surface of nanoparticles at an elevated temperature in a glycol solvent and eventually render the nanoparticles highly water soluble [192, 193]. What's more, these amphiphilic copolymers usually contain free amino or carboxyl groups and therefore allow for further functionalization of the particle surface with proteins or other biomolecules.

The third method is based on a ligand exchage technique [194, 195]. It utilized

bifunctional organic molecules that replace the oleylamine ligand to provide a water-soluble carboxyl-functionalized surface, which is also capable of immobilization to biological assemblies via bioconjugate chemistry. Gan Moog Chow et al [196] employed polyethylene glycol 600 diacid (HOOC-PEG-COOH) to replace the capping ligand on the surface of nanoparticles (oleylamine in this case) and they found nanoparticles remained as a clear colloid in deionized water without any noticable settling or precipitation after two weeks. Kamimura *et al.* used electrosatic immobilization of negatively charged poly(ethylene glycol)-co-poly(acrylic acid) to generate water-dispersible Y_2O_3 UC nanoparticles. Streptavidin was then attached to the surface, resulting in the functionalization of these particles [197].

Moreover, some groups employed ligand oxidation method for surface modification [198, 199]. In this method,the carbon-carbon double bond of the ligand can be oxidized by Lemieux-von Rudloff reagent to generate a pendant carboxylic functional group. Li et al [198] have demonstrated conversion of oleic acid-stabilized hydrophobic $NaYF_4$: Yb/Er nanoparticles into water-dispersible nanoparticles with Lemieux-von Rudloff reagent. One drawback of this method is that it is only applicable to a limited number of ligands containing unsaturated carbon-carbon bonds.

Finally, layer-by-layer (LBL) assembly strategy is also used for the surface mordification [200, 201]. It is of the electrostatic type rather than of the covalent type. Upon sequential adsorption of positively charged poly(allylamine hydrochloride) (PAH) and negatively charged poly(sodium 4-styrenesulfonate) (PSS) onto the surface of nanoparticles, Li et al [200] successfully modified $NaYF_4$: Yb/Er nanoparticles with stable amino-rich shells. The LBL assembly technique offers many advantages such as simplicity, universality, and thickness control in nanoscale. More importantly, the high stability and biocompatibility of these polyions make them attractive as coating materials for a wide range of fundamental and technological applications. Drawbacks include the required washing steps and the limitation of this process to hydrophilic nanoparticles.

6.4 Application of UC nanoparticles as labels in bioassays

As luminescence probes, the main advantage of UC nanoparticles is that the interference of background noises with luminescence detection can be avoided, since they have an excitation wavelength at 980 nm and short emission wavelengths in the visible light range, while no biological matrix upconverts in the infrared range. The properties of some commercially available UC nanoparticles have been evaluated [202].

In 1999, Zijlmans et al. reported the first bioassay application of UC particles (200-400nm) [146]. Two kinds of UC nanoparticles green-emitting $Yb^{3+}/Er^{3+} - Y_2O_2S$ particles and blue-emitting $Yb^{3+}/Tm^{3+} - Y_2O_2S$ particles, were used for avidin labeling. The labeled avidins were then used for immunohistochemical detection of prostate-specific antigen in paraffin-embedded sections of human prostate tissue, and immunocytochemical staining of human lymphocytes. Fig. 9.3a shows the labeled tissue section after double exposure to both blue light and UCP activating IR light; the (non-specific) green autofluorescence signal clearly overlaps with the specific blue phosphor signal. In contrast the PSA-specific signal is distinctively visible (Fig. 9.3b) after IR exposure only. Autofluorescence can be a significant problem when the labeling efficiency is low and/or the number of targets is minimal. It is a consequence of the higher energy blue or ultraviolet light required for excitation of commonly-used fluorescent dyes and the fact that many biological materials also fluoresce. Moreover, fluorophores suffer from photodecomposition (bleaching) upon excitation, thereby limiting the number of photons emitted. By contrast, UCP reporters do not bleach and can be repeatedly examined at high excitation energy levels without deterioration and UCP labeled tissue sections can be conveniently stored as a permanent record.

UC nanoparticles that are silica-coated and functionalized are readily conjugated to biomolecules such as antibodies. This creates a sensitive probe-reporter pair that has been successfully adapted to a standard lateral flow format, scannable by either a benchtop or handheld instrument [149]. As seen in Fig. 9.4, a lateral flow(LF) strip of plastic-backed nitrocellulose is mechanically impregnated (e.g. striped by an ink jet) with both test and control lines. The test line typically consists of antibodies specific for the analyte of interest, in a buffered solution. The control line is a buffered solution of either a generic antibody-binding protein (e.g. protein G) or an antibody that is

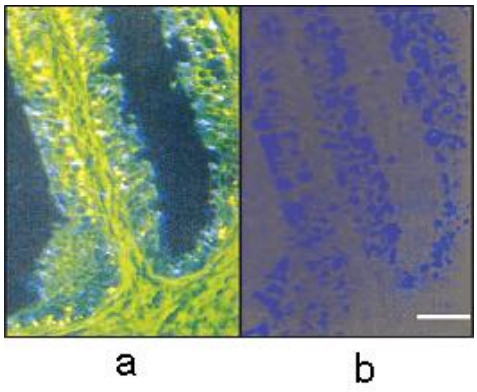

Figure 6.3: Detection of PSA in paraffin-embedded sections of human prostate tissue with biotinylated antibodies and neutravidin blue phosphors. a) Tissue section after exposure to both blue and IR excitation light. The green autofluorescence coincides with the PSA specific blue phosphor luminescence; b) IR excitation of the blue phosphor labelled PSA, adopted from [146]

specific for the species from which UCP conjugated antibodies were derived (e.g. goat anti-mouse). UC particles conjugated with analyte-specific antibodies are dried into a fleece attached to the nitrocellulose strip and in physical contact with both the strip and an overlying absorbent pad. Distal to the UCP fleece is a wicking fleece that acts as a sink to assist in driving capillary flow during the assay. Once all reagents have been applied, the test strip can be dried and assembled into a protective cassette housing. These strips have a shelf life on the order of months to years under appropriate storage conditions. In a $'$sandwich$'$ assay format, 10^3 org/mLE.coliO157 : H7 organisms were detectable in a negative control background of 10^9 other organisms per milliliter of culture medium. Coefficients of variation in concentrations tested from 0 to 10^7 org/mL were all $\leq 10\%$. In a competitive inhibition assay format, a multiplexed test simultaneously detected amphetamine, methamphetamine, phencyclidine, and opiates in saliva.

Molecular biological strategies, in particular enzymatic nucleic acid amplification methods [203], have greatly increased the sensitivity and speed of several diagnostic assays. However, these amplification methods have limitations, ranging from amplification artifacts that can result in false positives, as well as the need for complex

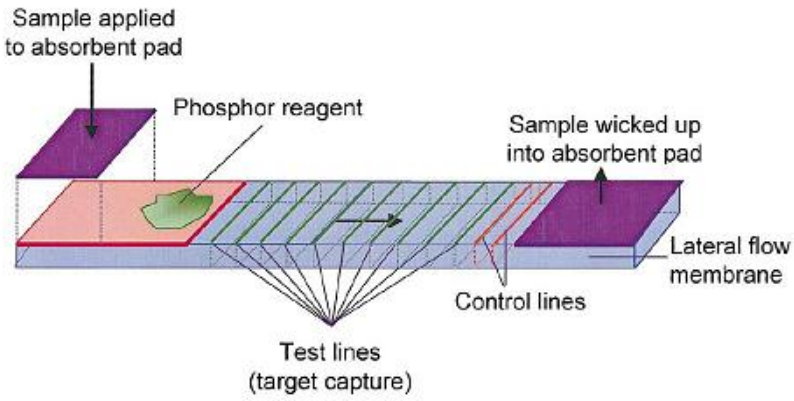

FIGURE 6.4: UCP lateral flow format. The architecture of the UCP lateral flow strip is designed to accommodate up to 12 distinct test lines. In addition, each strip also contains two control lines, adopted from [148]

equipment and expensive enzymes. The most commonly utilised amplification technique is the polymerase chain reaction (PCR). Theoretically, one target molecule can be amplified by PCR up to 10^9 times. However, procedures requiring such extreme high amplification rates (number of cycles) are often plagued by the production of PCR artifacts. In combination with a sensitive reporter such as UCP, the demand on the amplification process is reduced. Paul Corstjens et al [204] reported the use of UC particles in detection of the prescence of human papilloma virus type 16 (HPV-16) in DNA samples from a selection of cervix carcinoma. In this particular test a lateral-flow (LF) assay was used to capture haptenized DNA molecules and hybrids, which were immunolabeled (before LF) with 400-nm UC particles. These particles emit green light (550 nm) and are composed of ytterbium and erbium as respective absorber and emitter ions embedded in a preceramic matrix. The use of the UC reporters in LF assays, as compared with colloidal gold, improved the detection limit at least 100-fold. UC LF-DNA tests were successfully applied to detect (in a blind test) the presence of HPV16 in DNA extracts obtained from cervical carcinomas. Test results matched 100% with previous characterization of these carcinomas. In addition, the potential of amplification-free sandwich-hybridisationbased UCP-LF assays was determined with a test developed to identify the bacterial pathogen *Streptococcus* pneumoniae [205].

Using a sandwich hybridization format, the presence of pathogen *Streptococcus* pneumoniae was detected by means of LF and UC particles (see Fig. 9.5) The result confirmed that it is possible to identify bacterial genomes (based on the presence of a specific single-copy gene sequence) from as little as 1 ng of genomic DNA, which is in the low atto mole range and equivalent to DNA extracted from $10^5 - 10^6$ bacterial cells. When analyzing samples for the presence of viral sequences, presumably only around 1 pg of viral DNA would be required. This level of sensitivity is exceptional for a rapid nondemanding hybridization-based assay not requiring any form of target amplification.

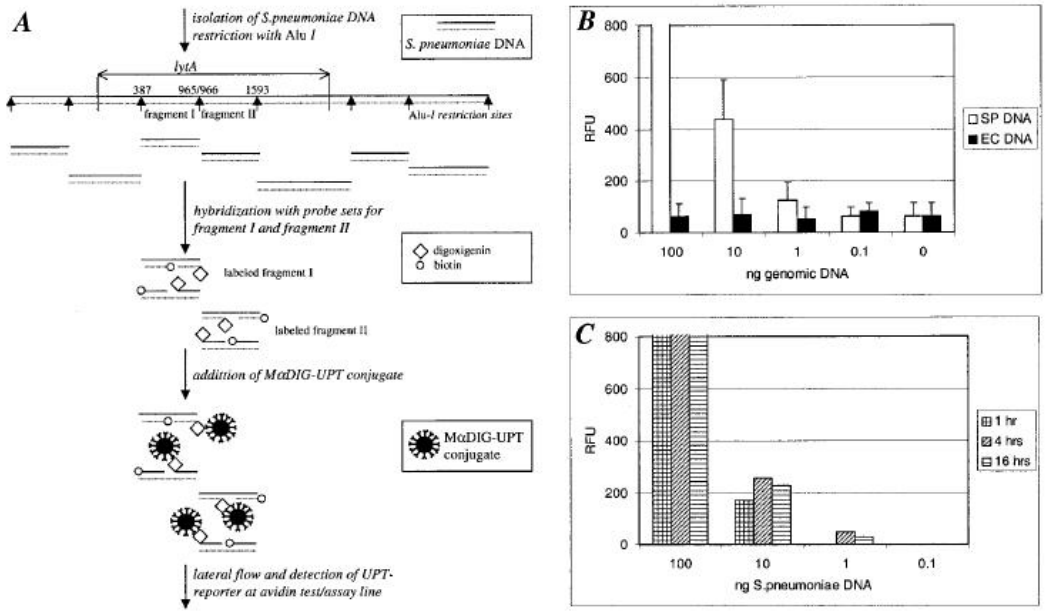

Figure 6.5: Detection of Streptococcus pneumoniae DNA, lytA fragments. A) Sandwich hybridization and lateral flow assay applying UC nanoparticles to detect lytA hybrids. B) Dilution series of digested genomic DNA of S. pneumonia(SP) and E. coli (EC) in 10 μg of fish sperm DNA to analyze detection sensitivity. C) A single-test result, showing the effect of the hybridization time on the sensitivity of detection of S. pneumoniae DNA, adopted from [205]

UCP are very attractive reporters for fluorescence resonance energy transfer (FRET)-based bioanalytical assays. The large anti-Stokes shift and capability to convert near-infrared to visible light via sequential absorption of multiple photons enable complete elimination of autofluorescence, which commonly impairs the performance of

fluorescence-based assays. UCP are ideal donors for FRET, because their very narrow-banded emission allows measurement of the sensitized acceptor emission, in principle, without any crosstalk from the donor emission at a wavelength just tens of nanometers from the emission peak of the donor. In addition, acceptor dyes emitting at visible wavelengths are essentially not excited by near-infrared, which further emphasizes the unique potential of up-conversion FRET (UC-FRET). Although, UC-FRET is a relatively new technology, first described in 2005, the potential versatility of the novel label technology has been demonstrated in multiple papers from separate research groups: applications range from ligand binding assays [206–208] and competitive immunoassays in whole blood [209] to enzyme activity [210] and nucleic acid hybridization assays [211]. The assays are based on either the measurement of sensitized acceptor emission or quenching of the up-conversion fluorescence signal. In all of the assays mentioned above, the lower limit of detection has been below subnanomolar concentrations, demonstrating the potential sensitivity of the UC-FRET-based assays.

The biotin assay, which was based on the use of a streptavidin-coated UCP and a biotinylated fluorescent phycobiliprotein, B-phycoerythrin (BPE), can be considered as a proof-of-principle to demonstrate the feasibility of resonance energy transfer from a UCP donor to a fluorescent acceptor protein and measurement of the sensitized acceptor emission at red wavelengths (600 nm) without any directly excited acceptor emission [212]. Further development has resulted in a competitive immunoassay for E2, utilizing a UCP coated with anti-E2 antibody Fab fragments and an E2-conjugated small-molecular-weight fluorescent dye, Oyster-556 [213] (see Fig. 9.6). The assay was performed both in buffer and in serum, not only to demonstrate the applicability of a small-molecular-weight dye as an acceptor, but also to verify that no autofluorescence or absorption of excitation light disturbed the measurement in the presence of biological sample material.

Fluorescence imaging is a very important technique for biological studies and clinical applications due to its high temporal and spatial resolutions and has been used for in vivo imaging [214]. Conventional fluorescence imaging is based on single-photon excitation, emitting low energy fluorescence when excited by high energy light. Using high

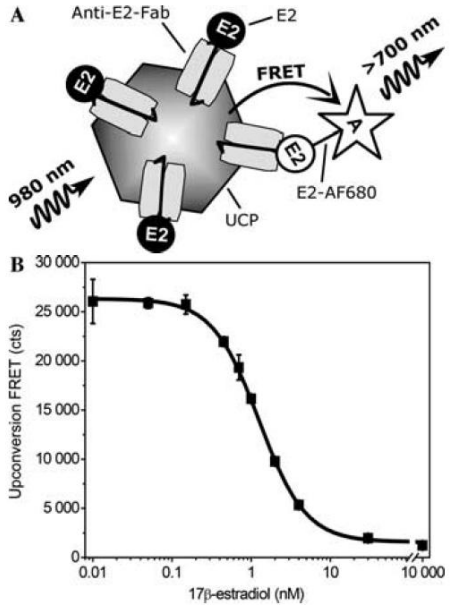

Figure 6.6: (A) Immunoassay principle and (B) standard curve of UC-FRET-based competitive immunoassay for 17β-estradiol (E2) in 20% (vol/vol) anti-coagulate whole blood, adopted from [213]

energy excitation light has some limitations like DNA damage and cell death caused by long-term irradiation, significant auto-fluorescence from biological tissues resulting in low signal-to-background ratio, and short penetration depth in biological tissues [215]. Up-conversion photoluminescence(PL) imaging, on the other hand, involves conversion of two or more low energy photons-usually near infrared (NIR)-to higher energy visible emissions [216]. Therefore, its advantage is absence of autofluorescence and decreased light scattering, which is an ideal case for deeper tissue penetration. Moreover, because of the quasiquadratic dependence of the PL intensity on the power of excitation of the UCP [217], there is an inherent 3-D localization of PL, similar to two-photon induced fluorescence, which can be used in the development of 3-D imaging systems. Based on the advantages mentioned above, UC particles doped with Er^{3+} have been widely used for bioimaging [152, 195, 218, 219]. Recently, Dev K. Chatterjee et al [195] delivered polyethyleneimine (PEI) coated $NaYF_4$: Yb/Er nanoparticles with a mean diameter of about 50 nm and a relatively narrow size distribution into specific cell lines or injected intradermally and intramuscularly into specific tissues either near the body surface or deep in the body of rats showed visible fluorescence, when exposed to

a 980nm NIR laser. Both Fig. 9.7 and Fig. 9.8 show up-conversion photoluminescence was clearly observed from both cells and tissues, demonstrating that the nanoparticles are useful for live cell and tissue imaging. In addition, Lim et al [220] described an up-conversion imaging case *in vivo*. Y_2O_3 : Yb/Er particles with high Er^{3+} concentration favored red emission, while less Er^{3+} doped particles mainly unveiled green fluorescence. For tracing the digestive system of the nematode Caenorhabditis elegans, 150 nm uncoated particles were directly transferred to the growth medium used to feed the worms. Both NIR laser and electron radiation were used to illuminate the UCP in the worm's intestines (Fig. 9.9). Neither degradation of phosphors nor damage to worms were observed, and this suggested the biocompatibility of Y_2O_3 : Yb/Er.

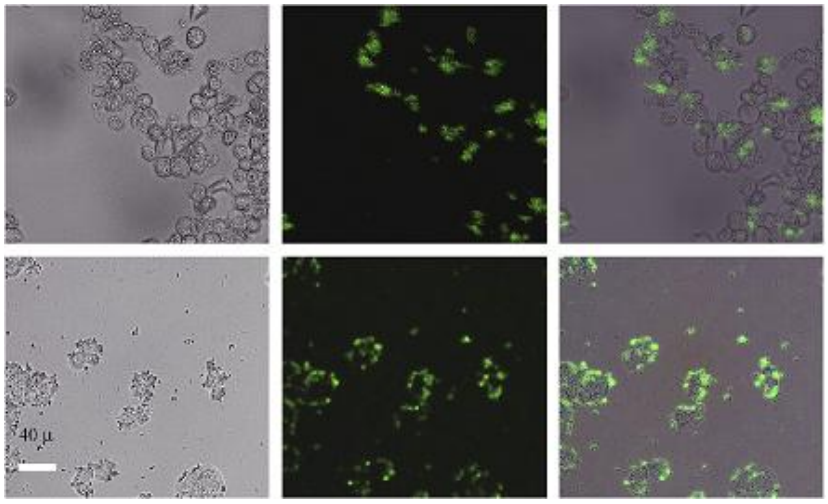

FIGURE 6.7: Bright field, confocal, and superimposed images of live human ovarian carcinoma cells (OVCAR3, top row) and human colonic adenocarcinoma cells (HT29, bottom row), with PEI/$NaYF_4$ nanoparticles attached, adopted from [195]

6.5 Equipment for UCP analysis

Microscope

UCP emissions on tissue, cells, or nucleic acid microarrays on glass slides is readily monitored using a Leica DM epifluorescence microscope with a xenon lamp adapted to use IR light excitation and detect the emitted light (Fig. 9.10a) [144, 221]. The microscope modifications included the placement of three filters: (i) an excitation filter with a 900 to 1000 nm band pass; (ii) an 800 or 725 nm short-pass dichroic mirror; and (iii) a 750nm short-pass emission barrier or narrow 515 to 585 nm band-pass emission

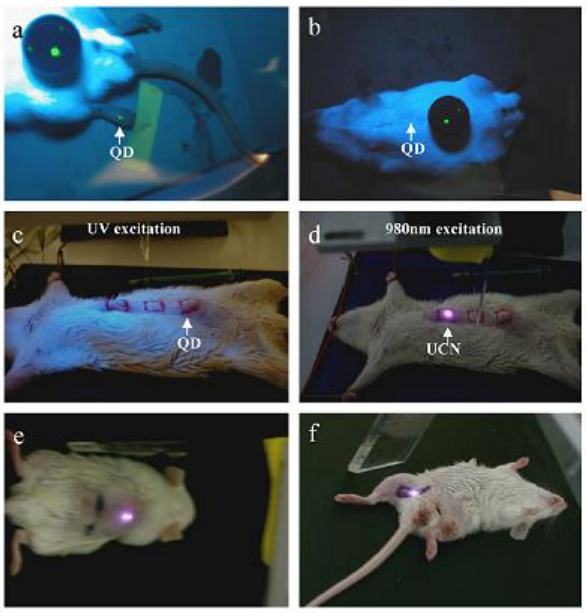

Figure 6.8: In vivo imaging of rat: quantum dots (QDs) injected into translucent skin of foot (a) show fluorescence, but not through thicker skin of back (b) or abdomen (c); PEI/$NaYF_4$ nanoparticles injected below abdominal skin (d), thigh muscles (e), or below skin of back (f) show luminescence, adopted from [195]

filter, and removal of the ′hot-mirror′ and ′red-blocking′ filters from the epi-illumination light path.

Benchtop scanner

For the detection of UCP signals in microtiter plate wells, a 96-well Packard FluoroCount fluorescence microtiter plate reader was modified (Fig. 9.10b) [149, 222]. The instrument was equipped with an external 980nm IR laser (1.2 W, SpectraPhysics/Opt-Power Corp.). IR light is guided using a fibre bundle through an 850 nm long pass filter and focusing lens. The same fibre bundle is used to pick-up light emitted by IR-excited UC particles. The emission signal is guided through a specific band-pass filter appropriate for the emission wavelength of the used UC particle. The signal is processed by a photomultiplier and is reported as relative fluorescence units.

To facilitate accurate scanning of lateral flow and transdot strips (as well as the whole surface of microtiter plate wells), the reader was equiped with microstepper motors for accurate control of x- and y-axis movement that allow scanning of a 7- by 11 cm area with a resolution of approximately 0.09 mm [149]. Several plastic guides

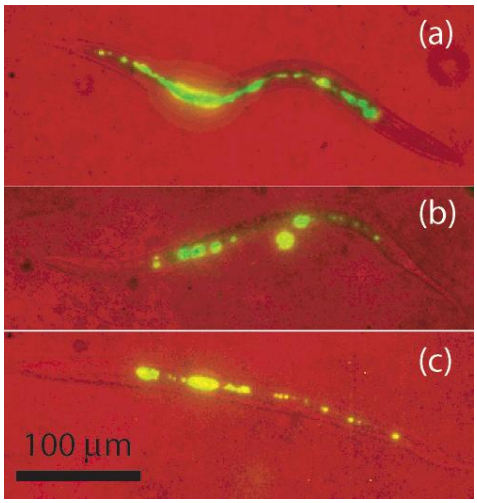

FIGURE 6.9: False color two-photon images of C. elegans at 980 nm excitation with red representing the bright field and green for the phosphor emission. The worms were deprived of food over a period of 24 h, showing little or no change at (a) 0 h, (b) 4 h, and (c) 24 h, adopted from [220]

were fabricated and the software customised to allow scanning and recording data from different nitrocellulose strip formats.

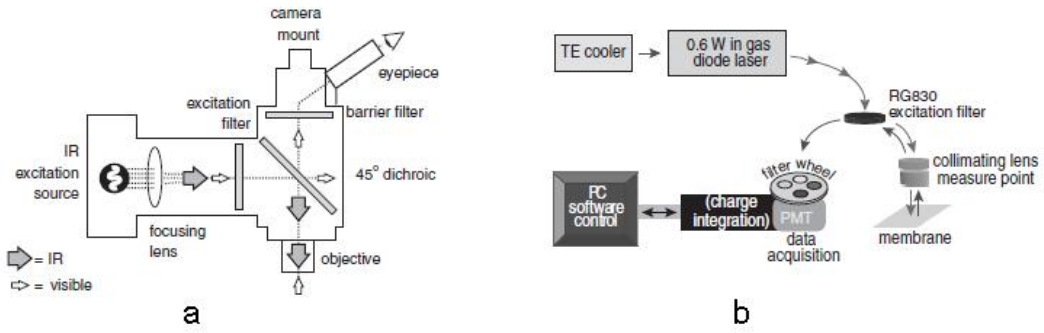

FIGURE 6.10: UCP Instrumentation. a) Schematic representation of a Leica DM epifluorescence microscope modified to excite UC particles with 980nm light from a xenon XBO 75W lamp and to visualise blue, green or red phosphor luminescence. b) Schematic representation of a modified Packard FluoroCount reader, adopted from [143, 222]

Table 6.1: Composition of Upconversion Phosphors

Host material	Absorber ion	Emitter ion	Emission(s)
Oxysulfides(O_2S)			
Y_2O_2S	Yb	Er	Green
Y_2O_2S	Yb	Tm	Blue
Gd_2O_2S	Yb	Er	Red
La_2O_2S	Yb	Ho	Green
Oxyhalide(OX_y)			
YOF	Yb	Tm	Blue
Y_3OCl_7	Yb	Tb	Green
Fluorides(F_x)			
YF_3	Yb	Er	Red
GdF_3	Yb	Er	Green
LaF_3	Tb	Ho	Green
$NaYF_4$	Yb	Tm	Blue
Gallates(Ga_xO_y)			
$YGaO_3$	Yb	Er	Red
$Y_3Ga_5O_{12}$	Yb	Er	Green
Silicates(Si_xO_y)			
YSi_2O_5	Yb	Ho	Green
YSi_3O_7	Yb	Tm	Blue

7

Upconversion in $NaYF_4 : Yb, Er$ Nanoparticles Amplified by Metal Nanostructures

Introduction

Lanthanide-doped upconverting nanocrystals have recently emerged as an area of intense research activity, due to their potential applications in life sciences research and security [223–226]. In contrast to the conventional inorganic fluorophores [227, 228], organic dyes [229, 230], and semiconductor quantum dots [231, 232], these nanoparticles use inexpensive and high-power near-infrared (NIR) diode lasers as the excitation source to produce visible luminescence. Under continuous-wave excitation at 980 nm, these nanoparticles exhibit superior photostability and unique upconversion

(UC) luminescence that has many attractive features, such as sharp absorption and emission lines with a full width at half maximum of ≤ 15 nm [233]. Moverover, the use of NIR excitation can minimize the possible photodamage in biological systems and autofluorescence of some biological samples, permitting deeper tissue penetration and bioimaging. Despite the above advantages, these nanoparticles typically have low emission efficiency due to surface quenching, particularly strong in small nanoparticles with large surface area/volume ratio and a relatively small photon absorption cross section. Intense research effort is currently oriented towards maximizing UC quantum yield [158, 234], where a typical approach is to search for optimum combinations of different host matrices and rare-earth (RE) atoms.

Here we chose an alternative strategy to enhance UC luminescence which relies on metallic nanostructures to favourably modify the properties of close fluorophores and to alleviate some of their classical photophysical constraints. The nanoscale fluorophore-metal interactions give rise to the process known as metal-enhanced fluorescence (MEF) [1, 2, 4, 46]. The MEF effect is due to excited fluorophores interacting with surface plasmon resonances in metals, and this effect is particularly well pronounced in metal nanostructures. It has been shown to produce desirable effects such as increased quantum yield of fluorophores, their decreased lifetimes, increased photostability, and potential for improved energy transfer [1]. Due to the above advantages, the MEF has been widely used for fluorescence enhancement from organic dyes [114, 115], RE complexs [235, 236] and quantum dots [237, 238]. Among different MEF substrates, silver and gold are the most widely investigated materials due to their unique plasmonic properties. Recently, the coupling of UC materials with metal nanomaterials has been reported, mainly focusing on glass composites and films [239–241]. However, to the best of our knowledge, there were no reports demonstrating metal-enhanced UC luminescence by using both silver and gold nanostructures with different morphologies.

In this study we demonstrated the metal-induced enhancement of the UC luminescence of $NaYF_4 : Yb, Er$ nanoparticles in two different experimental systems. In the first system the nanoparticles were conjugated to silver nanostructures deposited on

silica beads. The conjugation was achieved by using a simple bioassay, where streptavidin (SA)-labeled UC nanoparticles were bound to the biotinylated anti-mouse IgG antibody. This assay was carried out on silica beads with and without Ag nanostructures at the same experimental conditions, for comparison. In the second system, the $NaYF_4 : Yb, Er$ nanoparticles were coated with gold shells. The $\sim$5 nm gold shell coating on the surface of these nanoparticles was achieved via a robust method [242]. Such gold nanoshell has a strong absorbance in the green region of the visible spectrum and does not inhibit emission from Er^{3+} centered around 525 and 545 nm, in direct contrast to the case of quantum dots, where the fluorescence emission from the quantum dots is quenched by the gold shell in the core-shell architecture [243].

Experimental section

Materials

The following materials were purchased from Sigma-Aldrich and used as received: YCl_3 (99.9%), $YbCl_3$ (99.9%) , $ErCl_3$ (99.9%), oleic acid (OA, 90%), octadecene (ODE, 90%), methanol, NaOH, NH_4F, ethanol, acetone, chloroform, CO-520, cyclohexane, hexane, tetraethyl orthosilicate (TEOS), ammonia (wt 30%), NaF ($\geq$ 99%),HCl(36.5$-$38.0%),$HAuCl_4$, trisodium citrate, $NaBH_4$, (3$-$aminopropyl) trimethoxysilane (APTMS), concentrated H_2SO_4, silver enhancing solution A, silver enhancing solution B (enhancing kit), biotinylated rabbit anti-mouse IgG antibody, streptavidin (SA), glutaraldehyde, bovine serum albumin (BSA), phosphate buffered saline (PBS, pH 7.4), Tween 20 and poly-L-lysine. 400 nm silica beads were purchased from Bangs Laboratories, Inc. Glass microscope slides were obtained from Fisher Scientific. Nanopure water (>18.0 MΩ), purified using the Millipore Milli-Q gradient system, was used in all the experiments.

Preparation of gold shell-coated $NaYF_4 : Yb, Er$ **nanoparticles**

Synthesis of the gold shell-coated nanoparticles was done by employing a facile one-pot technique [242]. Briefly, 0.2 M solution of YCl_3, $YbCl_3$ and $ErCl_3$ was mixed with 0.2 M sodium citrate and 1 M NaF solution in a 1: 2: 4 volume ratio and heated to 90^oC. Then 380 nmoles of 0.1% $HAuCl_4$ were added to the formed solution, and the heating was continued for two and half hours. The pink colored nanoparticles were

centrifuged and dried at 80-100^{o}C. The resulting product was crushed and heated to 450^{o}C for 12 h in N_2 flow furnace, followed by suspension in water.

Preparation of SiO_2-coated nanoparticles

The SiO_2-coated $NaYF_4 : Yb, Er$ nanoparticles were firstly synthesized by thermal decomposition of rare-earth/sodium chloride precursors in oleic acid and octadecene and then coated with the SiO_2 shell via the hydrolysis of TEOS in a basic solution [244]. Firstly, YCl_3, $YbCl_3$ and $ErCl_3$ were mixed with OA and ODE, and this solution was heated to 160^{o}C to form a homogeneous solution. After cooling down to room temperature, 10 mL methanol solution containing NaOH and NH_4F was slowly added with stirring for 30 minutes. The solution was then heated to 300^{o}C for 1h under Argon protection and cooled down to room temperature. The $NaYF_4 : Yb, Er$ nanoparticles were precipitated with ethanol and washed with ethanol/water (1:1 v/v) for three times. These as-prepared nanoparticles were dispersed in cyclohexane, and then CO-520 and ammonia were added to form a water-in-oil microemulsion. After sonicating for 20 min, TEOS was then added into the microemulsion with stirring for two days, resulting in SiO_2-coated nanoparticles. They were precipitated by adding acetone, and were washed with ethanol/water (1:1v/v) twice.

Preparation of Ag nanostructures on silica beads

The deposition of Ag nanostructures on the silica beads was performed using a protocol previously reported by our group [245]. Firstly, APTMS was added to the silica beads solution with stirring overnight. Secondly, the ∼10 nm as-prepared Au colloids were added to the above solution with stirring for 30-90 min to allow them binding to silica surface, followed by washing with nanopure water 3 times. The deposition of Ag nanostructures on the silica beads was carried out as follows. Equal amounts of the silver enhancer solutions A and B were mixed using a vortex, followed by adding into Au-silica solution and allowing to react for 3 min. This process was carried out in the dark as the silver enhancer kit is light-sensitive. The resulting Ag nanostructure-coated silica beads were centrifuged and washed with nanopure water 3 times to terminate the reaction between silica beads and the enhancer solution.

Conjugation of SA with SiO_2-coated $NaYF_4 : Yb, Er$

5 μL of APTMS and 400 μL of ammonia (wt 30%) were added to 20 mL ethanol solution containing 1 mg of SiO_2-coated $NaYF_4 : Yb, Er$ nanoparticles. After stirring for 24hrs at R.T, nanoparticles were centrifuged and washed twice with ethanol and 3 times with nanopure water to completely remove unreacted materials. These nanoparticles were then added to 2 mL of PBS buffer containing 0.5 mg SA and 0.3mL of 1% glutaraldehyde (see Fig.11.7a). After stirring again for 22 hrs at 4^oC, 1.0 mg of $NaBH_4$ was added and the solution was incubated for 2 hr at R.T. The nanoparticles were centrifuged and washed with PBS buffer 3 times. The SA-UC nanoparticle conjugates were stored at 4^oC before use.

SA-biotin-based assay

The glass slides were cleaned by soaking in the piranha solution for at least overnight and then rinsed with nanopure water and dried in air before use. Caution: Piranha solution is extremely caustic. Use only with extreme care. The slides were then dip coated with poly-L-lysine solution (freshly prepared solution: 8 mL of water + 1.0 mL of 1% poly-L-lysine solution + 1.0 mL of PBS buffer, pH 7.4). After drying in air, each slide was covered with tape containing punched holes to form wells on the surface. Each well was filled with a 20 μL suspension of silica beads: the first slide with Ag-coated silica beads and the second with uncoated silica beads. After drying in air, each well was filled with 20 μL of 40 μg/mL biotinlyated rabbit anti-mouse IgG antibody solution. The slides were incubated overnight in a humid chamber and rinsed with PBST (PBS with 0.05% Tween 20) and PBS, which were used in all washing procedures. Blocking was performed by adding the BSA solution and incubation for 1 hr in a humid chamber to minimize non specific binding. After rinsing, each well was incubated for 1 hr with 20 μL per well of SA-UC nanoparticle conjugates, followed by a rinse and stored at 4^oC before measurement (see Fig. 11.7b).

Characterization

The extinction spectra of silica beads with and without Ag nanostructures were measured using a Cary spectrophotometer (Cary 5000 UV-vis-NIR, Varian Inc.). Transmission Electron microscopy (TEM) images were taken on a PHILIPS CM10 system at an accelerating voltage of 100 kV. The samples were prepared by placing a drop

of dilute ethanol dispersion containing samples on the surface of a copper grid. UC luminescence spectra were obtained using a Fluorolog-Tau-3 system. In this measurement, the glass slides were maintained at a 45^o illumination in an upright position in the solid sample holder. The spectral width was set to 8 nm. The emission spectrum was recorded over a range of 550-750 nm. The UC luminescence lifetime was measured using purpose-built epi-fluorescence microscopy system ($\times$10 objective; dichroic beam splitter (Zeiss, FT395)). In the measurements, a pair of emission filters (FF01-543/22-25 BP Filter from Semrock (http://www.semrock.com/) for green emission and 5915-A clarity BP filter (640nm, 30nm bandpass) from Newfocus (http://www.newfocus.com) for red emission) were employed to obtain green and red emission, respectively. The samples were measured dry. The values of lifetime were derived by a bi-exponential curve fitting (Origin 8.0 software) with the residual error function X^2 value of less than 1.0. A diode laser (980 nm, maximum 1 Watt in CW mode) (Beijing Viasho Technology Co., Ltd., http://www.viasho.com/) with 1 m fiber (N.A: 0.22 and ϕ 200 μm core) was used as the excitation source in both UC spectrum and lifetime measurements (500 μs pulses at 1 kHz triggered by TTL signals).

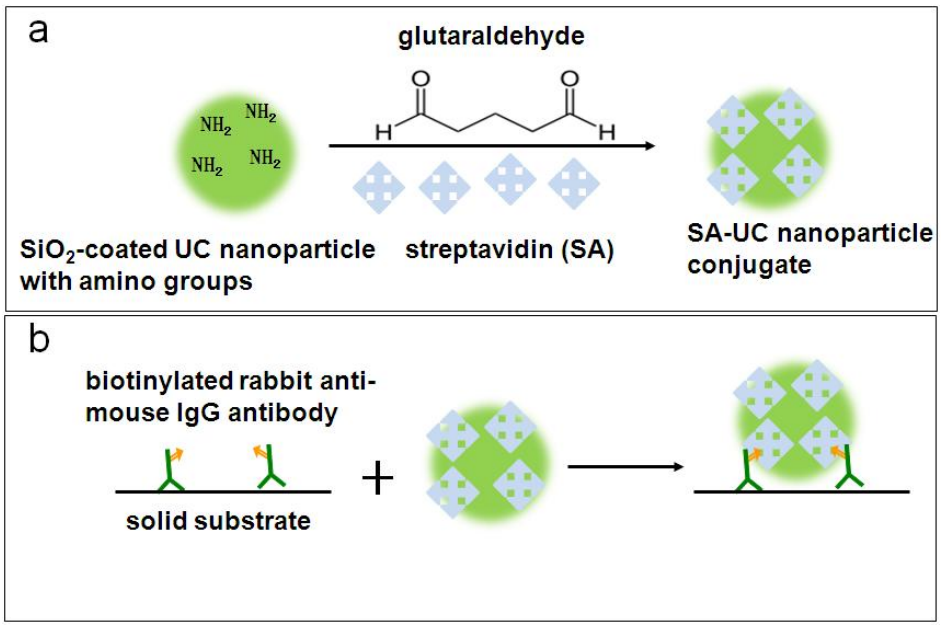

FIGURE 7.1: Schematic representation of conjugation SiO_2-coated nanoparticles with streptavidin (SA)(a) and a SA-biotin-based assay (b).

Results and discussion

The surface modification of these nanoparticles in the first experimental system was achieved using silica coating which protects the core from the environment and can be modified with amines, thiols and carboxyl groups. The uniformity of pure and silica-coated nanoparticles was confirmed by TEM images (Fig. 10.2a and b). The average size of nanoparticles was ∼20 nm and thickness of silica shell was ∼8 nm. The corresponding UC luminescence spectrum exhibits 3 distinct Er^{3+} emission bands around 526 nm, 545 nm and 660 nm which correspond to $^2H_{11/2} \rightarrow ^4I_{15/2}$, $^4S_{3/2} \rightarrow ^4I_{15/2}$ and $^4F_{9/2} \rightarrow ^4I_{15/2}$ transitions, respectively (Fig. 10.2c) [246]. The green and red emissions were observed in the spectrum. In the second system, gold nanoshell-coated $NaYF_4 : Yb, Er$ nanoparticles were prepared via co-precipitation of rare-earth/sodium chlorides. At the same time, deposition of the gold nanoshell was carried out via a redox reaction between a reducing agent (sodium citrate) and gold ions in the solution. This process can be understood as follows. After attaching the UC crystals, sodium citrate molecules released the electrons that can reduce gold ions to metallic gold atoms, resulting in the gold shell on the surface of $NaYF_4 : Yb, Er$. The presence of this gold shell was confirmed by the TEM image, as shown in figure 10.3. In addition, heat treatment of dry nanoparticles after gold coating (annealing to 450^oC for 12 h) was also carried out in order to obtain high UC efficiency. The mechanism reponsible for the upconversion luminescence is shown in figure 10.4.

The TEM image and extinction spectra of Ag nanostructure-coated silica beads were taken to check the size and surface plasmon band (Fig. 10.5). Fig. 10.5a shows the TEM image of Ag nanostructure-coated silica beads. As expected, Au-decorated silica beads were used as nucleation sites for growth of silver nanostructures, resulting in a much higher and more even silver coverage. On the other hand, the formation of silver nanostructure clusters was also observed. In such clusters, where particles are in close proximity, the coupling of the neighbouring particles plays an important role and modifies the dipole-dipole interaction between the dipole moments of the coupled particles. This dipole coupling concept has been successfully applied to the modeling of the optical properties of the silver fractal clusters [247]. Fig. 10.5b shows the

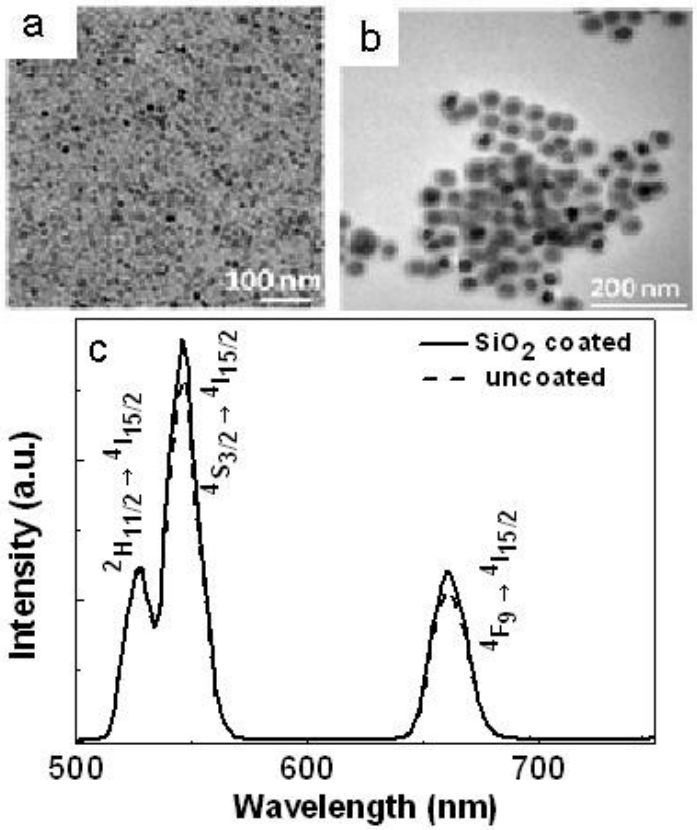

FIGURE 7.2: TEM images of pure (a) and SiO_2-coated $NaYF_4 : Yb, Er$ (b). (c) The UC luminescence spectra of SiO_2-coated and uncoated $NaYF_4 : Yb, Er$ nanoparticles.

corresponding extinction spectra of silica beads with and without Ag nanoastructures. The obvious Ag plasmon peak at around 400 nm was observed with Ag nanostructures adhering to the silica surface compared to that from pure silica beads. Moreover, the shape of such extinction spectrum suggests that light incident on the silica beads is scattered by silver nanostructures.

We first assessed the effect of silver nanostructures on UC luminescence amplification using SA-biotin binding system. The glass slide was firstly coated with Ag-silica beads and biotinylated IgG antibody molecules and SA-UC nanoparticle conjugates were then bound to silica beads via the avidin-biotin recognition mechanism. Now we discuss the first of our key results, the demonstration of UC luminescence enhancement induced by Ag nanostructures. We checked that these nanostructures do not change the spectral shape of UC emission. Indeed, in the samples with and without Ag nanostructures as shown in Figure 10.6a, we were able to observe a very similar

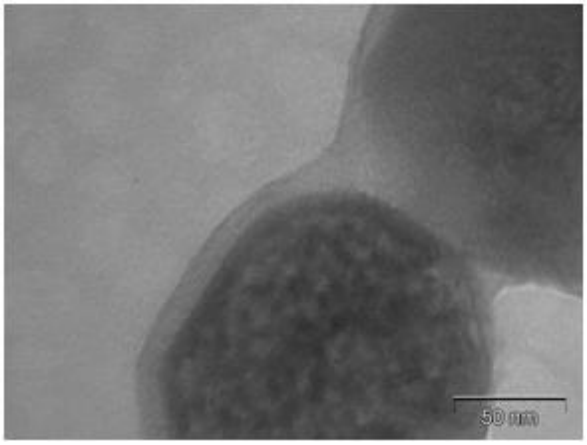

FIGURE 7.3: The TEM image of gold shell-coated $NaYF_4 : Yb, Er$ nanocrystals.

spectrum, with the emission bands typical of Er^{3+} around 525 nm, 545 nm and 660 nm. Ag nanostructures clearly enhanced UC luminescence with enhancement factors of ∼4.4 and ∼3.5 for green and red emission, respectively, compared to those from the control sample without Ag nanostructures. These values were obtained by dividing the integrated luminescence intensities for samples with Ag nanostructures after background subtraction (integrated luminescence intensities around 525 nm, 545 nm and 660 nm wavelengths only, from Ag nanostructures without the bioassay) by those without Ag nanostructures. For a more complete characterization of the effect of Ag nanostructures on UC luminescence we also carried out the lifetime measurements. As discussed in the literature [128], MEF is characterized by an increase in the quantum yield and a decrease in the lifetime of a fluorophore located in the proximity of the metallic nanostructures. The fluorescence lifetime provides unambiguous confirmation of the metal-induced fluorescence enhancement effect. The measured decay curves of UC luminescence from samples with and without Ag nanostructures indicate a clearly decreased lifetime observed in the presence of the silver nanostructures near these nanoparticles (Fig. 10.7), which was reduced from 240 μs to 120 μs for green emission and from 279 μs to 126 μs for red emission, respectively. Such reduced lifetime has two major implications, higher photostability and a higher number of emitted photons per unit time under the same excitation conditions. Both these properties make it possible to use shorter exposure time or obtain higher signal to noise for comparable exposure

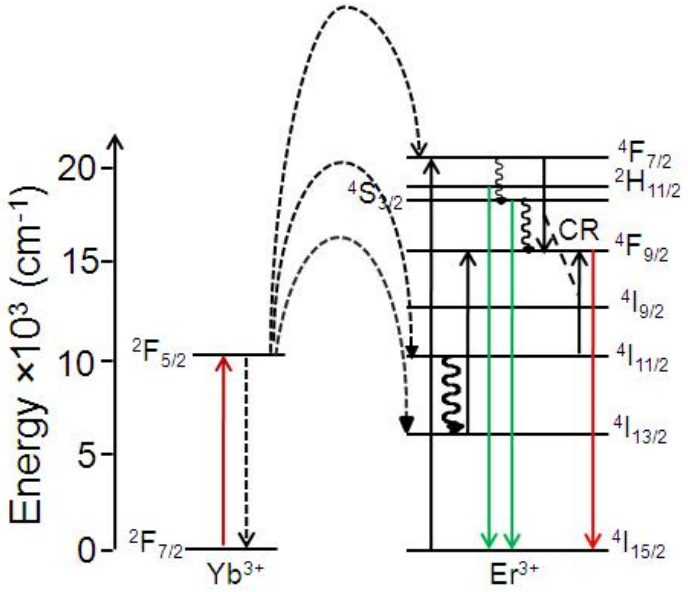

FIGURE 7.4: Schematic illustration of the UC process of Er^{3+} in $NaYF_4 : Yb, Er$ under 980 nm excitation. CR: cross relaxation.

times, thus increasing sensitivity and detectivity in luminescence measurements.

In general, MEF arises from the enhancement of the local electromagnetic field (referred as excitation enhancement) and also from that of the radiative decay rate (referred as emission enhancement). The distinction of these two contributions is usually not simple but rough estimation of relative contributions is possible from data in Fig. 10.6a and 10.7. Excitation enhancement produces a higher excitation rate but it does not change the lifetime of the fluorophore. When the interparticle distances are reduced the enhancement of local electromagnetic fields becomes strong [128], which magnifies the excitation enhancement induced by these nanostructures. In our case, the silver nanostructures on the surface of silica beads were very close to each other, resulting in the strong coupling effect between nanostructures. This coupling effect has a strong effect on the exciting electromagnetic field [131, 241, 248]. We also found the enhancement was not equal for both emission bands. Compared to the red band, the larger luminescence enhancement for green band was obtained as the Ag plasmon has better overlap. This wavelength-dependent enhancement can be attributed to emission enhancement [240]. Therefore, we found both excitation and emission enhancement contribute to the strong UC luminescence enhancement in our case. In addition, the

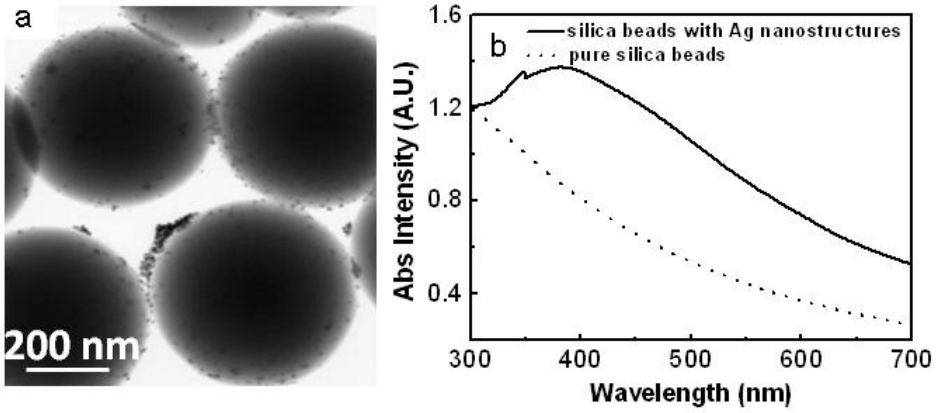

FIGURE 7.5: TEM image of Ag nanostructure-coated silica beads (a) and absorption spectra of the pure and Ag nanostructure-coated silica beads (b).

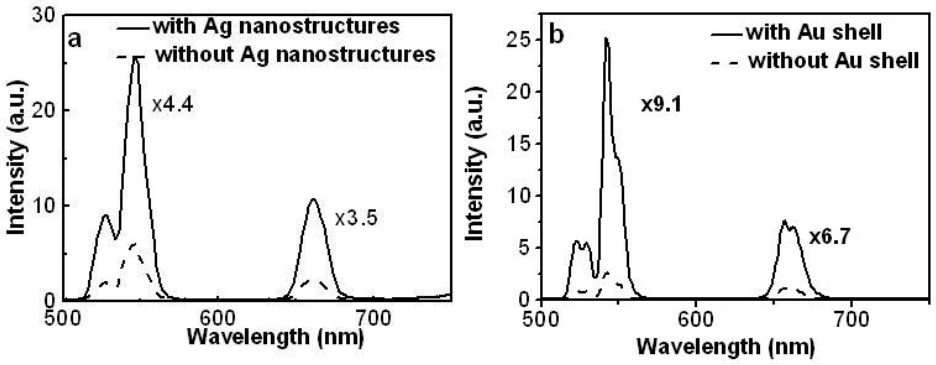

FIGURE 7.6: The UC luminescence spectra observed from samples with and without Ag nanostructures (a) and with and without gold nanoshells (b).

luminescence decays of samples with Ag nanostructures were shorter than those of control samples without Ag nanostructures, which is in accordance with previously described MEF [131, 240, 241]. This shows another evidence of the partial contribution from emission enhancement, which can also reduce the lifetime of the fluorophores [128].

We have also extended a similar analysis to the second system under investigation the gold shell-coated nanoparticles. As shown in Figure 10.6b, in samples with gold nanoshells both green and red emissions were increased, by a factor of ∼9.1 times and ∼6.7 times, respectively. Investigations on metal surface enhanced luminescence of nanocrystals indicate that it is correlated with the spectra overlap between the absorption or emission band of the luminophores and the surface plasmon band of metals [249].

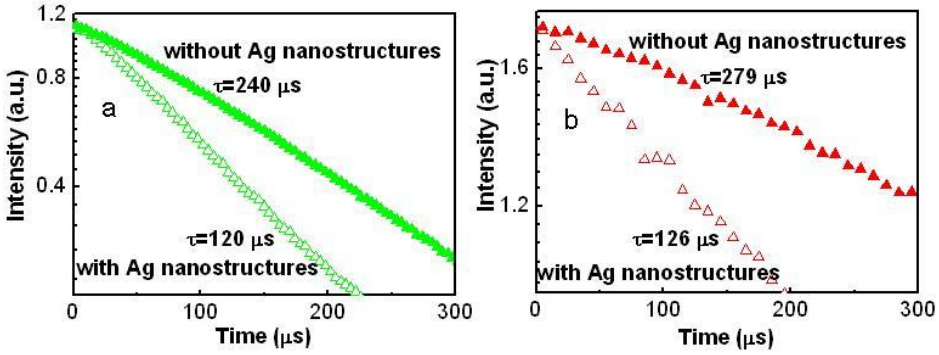

FIGURE 7.7: Representative UC luminescence decay times of the green(a) and the red(b) emissions from $NaYF_4 : Yb, Er$ nanoparticles with and without Ag nanostructures.

Therefore one could attribute this larger enhancement (∼9.1-fold) for green emission induced by gold nanoshells than the factor of 4.4 produced by silver nanostructures to better spectral overlap of gold plasmon band between 500-550 nm with the green upconversion luminescence, which can cause a better plasmonic coupling. We also found that the enhancement value (∼6.7-fold) for red emission induced by gold nanoshells was higher, compared to that induced by silver nanostructures (∼3.5 fold), and this again is consistent with the same argument. However other effects can also produce similar results, such as nanoparticle size in the first, bioassay system which increases the effective distance of fluorophores to the metal, as well as the role of surface recombination which is known to affect the green/red upconversion ratio in a major way [250, 251]. This surface recombination is expected to significantly vary between gold-shell coated and uncoated nanoparticles. Additionally, it is interesting to note that the luminescence decays for green and red emission in this study for gold shell-coated and uncoated samples behaved differently than in the case of silver, as shown in Figure 10.8. Specifically the red emission in gold shell-coated samples has a longer lifetime (∼389 μs) than in uncoated ones (∼316 μs), while the lifetimes of the green emission in these two samples are similar (∼456 μs). It should be stressed that plasmonic effect of the gold-shell coating is expected to reduce the lifetime in both green and red band, while the same coating protects nanoparticles from surface recombination, which has the opposite effect of lengthening the lifetimes. As a result the differences between lifetimes in coated and uncoated samples are likely to be reduced.

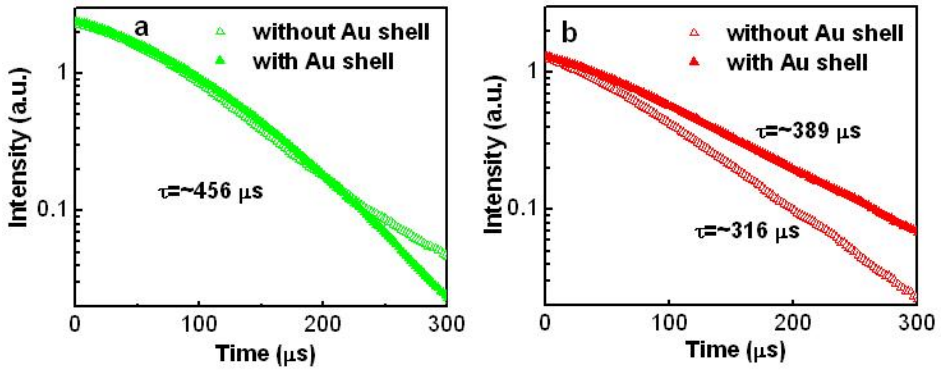

FIGURE 7.8: Representative UC luminescence decay times of the green(a) and the red(b) emissions from $NaYF_4 : Yb, Er$ nanoparticles with and without Au shells.

Conclusions

In summary, we have demonstrated the feasibility of using both silver nanostructures and gold nanoshells for UC luminescence enhancement. These two types of noble metal nanomaterials could produce clear luminescence enhancement (∼4.4-fold for green emission and ∼3.5-fold for red emission in the case of silver nanostructures; ∼9.1-fold and ∼6.7-fold in the case of gold nanoshells). We also demonstrated the shorter luminescence lifetimes induced by Ag nanostructures, confirming the MEF effect applied to UC luminescence enhancement. The results for gold nanoshells are attributed to a combination of plassmonic and surface recombination effects which can not be untangled in this geometry. Although further study will be necessary to fully elucidate the exact underlying mechanism, our results prove that UC emission can be enhanced by noble metals such as silver and gold, which promise potential applications of metal-UC nanoparticle composites in bioassays, bioimaging, and energy conversion requiring ultrahigh sensitivity and low background.

8

Ultrabright Eu-doped Plasmonic Ag@SiO_2 Nanostructures: Time-gated Bioprobes with Single Particle Sensitivity and Negligible Background

Introduction

Fluorescence has become one of the key detection methods in genomics, proteomics and cell biology and its applications extend as far as biomedical diagnostics [252–255]. Advances in this area have been accelerated by the development of new nanotechnology-inspired bioprobes such as quantum dots and silica or polymer encapsulated nanoparticles as well as smart detection strategies [99, 253–257]. In parallel, photonic techniques

have been pursued to take advantage of special optical properties, such as long fluorescence decay times or infrared multi-photon excitation wavelength (to name just a few) to suppress background noise in fluorescence detection [253, 258]. However, these developments have often occurred in isolation from one another, and, as a result, an ideal fluorescence detection strategy is yet to be developed. Its main objectives are well established and it should combine ultrabright bioprobes that have high absorption coefficients and high quantum yields, are clearly distinguishable and stable (free from bleaching and/or blinking). It should also provide high signal to noise ratio achievable by using photonics approaches such as time-gating.

Lanthanide fluorophores with their long lifetimes are desirable as bioprobes for ultrasensitive detection, since they can be used in a time-gating mode that offers exceptionally high background rejection [102, 259–262]. However the fluorescence intensity of all lanthanide-based fluorophores is very low compared with traditional fluorescent dyes, due to long (ms) fluorescence lifetimes. Recent efforts have been made to encapsulate lanthanide-based molecular complexes into nanoparticles, which produce amplified signals due to increased number of lanthanide ions per nanoparticle [257], but the limitation of slow radiative rates remains. The application of metallic nanostructures, particularly silver, provides a way to favorably modify the luminescence properties of close lanthanide fluorophores and to alleviate their classical constraints [263]. The metal-enhanced fluorescence (MEF) effect has been demonstrated with various types of metal nanostructures, including silver colloids, self-organised island films, nanorods, triangles, and fractal-like nanostructures [2, 264]. A range of fluorophore-doped metal (i.e. silver or gold) core/silica shell nanocomposites have been investigated as well [265–267].

The aim of this work is to explore and optimize the fluorescence enhancement of BHHCT-Eu-DPBT doped into Ag@SiO_2 nanocomposites, where both the silver-fluorophore distance and the Ag-core size are adjusted to optimize the fluorescence enhancement. This is achieved in the following way. Firstly, the thickness of the first silica shell is controlled by using different amount of tetraethyl orthosilicate (TEOS) which is able hydrolyze to generate silica sols on the surfaces of silver nanoparticles.

To facilitate this reaction ammonia is added as a catalyst for hydrolysis and condensation of TEOS. Once the core has been covered with the first shell, the APS-linked BHHCT-Eu-DPBT (APS-BHHCT-Eu-DPBT) is then covalently linked to a second, thinner exterior silica shell (see Fig. 11.1). Such system of layers makes it possible to systematically investigate the fluorescence enhancement of Eu chelates by Ag. Furthermore, the Ag-core size is varied by the growth of citrate-reduced silver colloids using metal deposition, which is an effective way of modifying the particle size. The fluorescence intensity enhancement from BHHCT-Eu-DPBT is also optimized by adjusting the Ag core size. At high excitation intensities, these nanocomposites showed greatly increased fluorescence enhancement factors of up to 145, due to significantly increased radiative rates in samples with metal cores, from about 700 s^{-1} in control samples to over 5000 s^{-1}. They are bright enough to be observed as single particles and are compatible with low background time-gating by using simple detection systems. A simple bioassay using avidin-biotin binding system was also carried out, demonstrating the potential of these bioconjugated nanocomposites to be used in a range of biological applications.

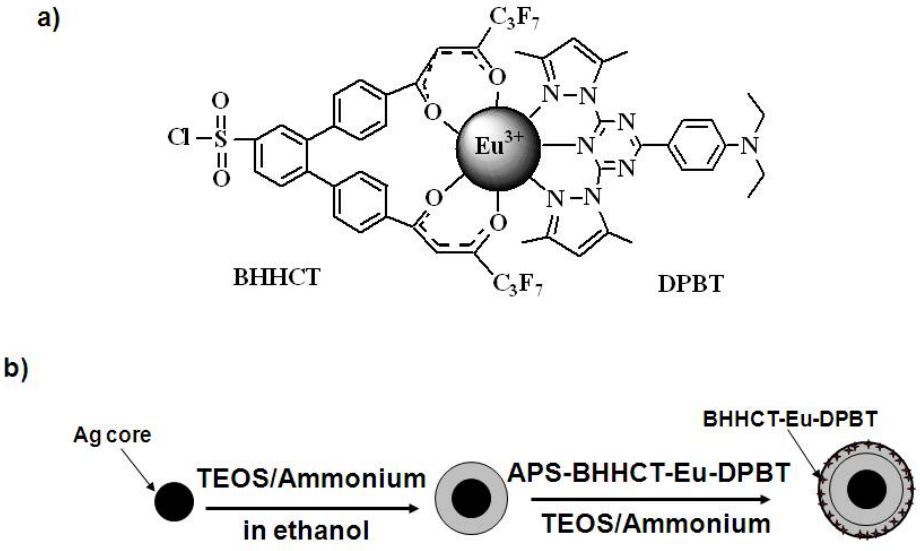

FIGURE 8.1: Schematic structure of europium chelate, BHHCT-Eu-DPBT (a) and steps required in the formation of BHHCT-Eu-DPBT-doped Ag@SiO_2 nanocomposites (b).

Experimental section

Materials

The following materials were purchased from Sigma-Aldrich and used as received: silver nitrate ($AgNO_3$), trisodium citrate, TEOS, (3−aminopropyl) trimethoxysilane (APTMS), biotinylated rabbit anti-mouse IgG antibody, glutaraldehyde, $NaBH_4$, ethanol, concentrated H_2SO_4, phosphate buffered saline (PBS), CH_3OH, streptavidin (SA), Tween 20, bovine serum albumin (BSA). 30% H_2O_2 was obtained from VWR. APS-BHHCT-Eu-DPBT was prepared as previously reported. Glass microscope slides were obtained from Fisher Scientific. Nanopure water (>18.0 MΩ) purified using the Millipore Milli-Q gradient system, was used in all experiments.

Synthesis of Ag Colloids

Silver nanoparticle colloids were prepared by reduction of silver nitrate with trisodium citrate [268, 269]. Freshly prepared 10 mL of 1% trisodium citrate was respectively added within 2 min into 490 mL of boiling aqueous solution containing 23 mg and 90 mg of $AgNO_3$ under vigorous stirring. After boiling for 1 hour, the reaction solution was cooled to room temperature. The as-prepared silver colloid solution was centrifuged at 500 rpm for 1 hour to remove the larger colloids. In this way, silver colloids with an average size of 81 nm and 52 nm were obtained. Smaller silver colloids were prepared from above silver colloids with an average size of 52 nm by using the following procedure. 20 mL of initial silver colloids was added to 380 mL of boiling Nanopure water followed by the addition of 90 mg of $AgNO_3$. Subsequently, 10 mL of 1% trisodium citrate was added dropwise to the suspension which was kept boiling for 30 min. This procedure leads to the formation of colloids with different silver core sizes. After cooling to room temperature, the final suspension was firstly centrifuged at 2000 rpm for 1 hour to separate larger Ag colloids followed by the second-round centrifugation of supernatant at 5000 rpm for 10 min to obtain smaller silver colloids. In this way, ∼33 nm silver colloids were obtained and used for further experiments.

Synthesis of BHHCT-Eu-DPBT-doped Ag@SiO_2 nanocomposites

Ag@SiO_2 nanocomposites were prepared using a method reported by Liu et al with some modifications [270]. Under vigorous stirring, 50 mL of the silver colloids solution was mixed with 200 mL of ethanol followed by the addition of 4 mL of 30%

ammonium hydroxide. After alkaline initiation, different amounts (2.5, 5 or 10 mL) of 10mM TEOS ethanol solution were added dropwise to the suspension. The reaction was stirred at room temperature for 24 hours. Each suspension of silica-coated silver colloids was centrifuged and washed 3 times with ethanol, followed by resuspension in 50 mL ethanol. The thickness of the silica shell was determined from TEM images and varied from ∼10 nm to ∼70 nm. The subsequent covalent conjugation of BHHCT-Eu-DPBT with such Ag@SiO_2 nanocomposites was achieved by using the following method. Typically, 500 μL of 2 mg/mL APS-BHHCT-Eu-DPBT toluene solution was added dropwise to 10 mL of Ag@SiO_2 ethanol solution under vigorous stirring followed by the addition of 0.24 mL of 30% ammonium hydroxide. After stirring for 20 minutes, 300 μL of 10 mM TEOS ethanol solution and 5 μL of APTMS was added dropwise into the suspension to form the second silica shell. The reaction was allowed to continue for 24 hour at room temperature. The Eu chelate-doped Ag@SiO_2 nanocomposites were centrifuged and washed 3 times with ethanol to remove excessive APS-BHHCT-Eu-DPBT, followed by resuspension in 5 mL ethanol. Measurements were performed on these stock suspensions.

Preparation of BHHCT-Eu-DPBT-doped hollow silica nanoshells

In order to evaluate the effects of metal core on BHHCT-Eu-DPBT in this Ag@SiO_2 system, the corresponding ″control ″ fluorophore-doped hollow silica nanoshells were also prepared by using the etching process where the metallic silver is oxidized to $Ag(CN)^{2-}$ by cyanide in the presence of air, according to

$$4Ag + 8CN^- + O_2 + 2H_2O \rightarrow 4Ag(CN)^{2-} + 4OH^-$$

This etching process ultimately leads to the formation of a hollow silica shell, as has been shown for the same reaction on silica-coated Au nanoparticles [271]. BHHCT-Eu-DPBT-doped hollow silica nanoshells were prepared from the corresponding chelate-doped Ag@SiO_2 nanocomposites by using the following strategy. 2 mL of 0.1M sodium cyanide solution was added to 1 mL of BHHCT-Eu-DPBT-doped Ag@SiO_2 nanocomposites with gentle stirring overnight to ensure complete etching of silver cores from those nanocomposites. The resulting hollow silica nanoshells were centrifuged and washed 3 times with ethanol, followed by resuspension in 1 mL ethanol. Since the

Eu chelates were covalently doped in the second silica layer, the etching of silver core with cyanide ions did not cause the leakage of the chelates from the silica layer. This procedure permits the same amount of the chelates to be excited with and without silver cores, allowing more precise evaluation of the effect of silver nanoparticles than by using pure silica nanoparticles as reference.

Conjugation of BHHCT-Eu-DPBT-doped Ag@SiO_2 **nanocomposites with biotynilated antibody**

1.0 mg nanocomposites and 0.3 mL of 1% glutaraldehyde were added to 2 mL of PBS containing 0.5 mg biotinylated rabbit anti-mouse IgG antibody. After stirring for 22 hs at R.T, 1.0 mg of $NaBH_4$ was added, and the solution was incubated for 2 h at R.T. The nanocomposites were washed with phosphate buffer 3 times and stored at 4^oC before use. The same method of conjugation with biotynilated antibody was used for BHHCT-Eu-DPBT-doped hollow silica nanoshells.

SA-biotin-based assay on glass slides

The microscope glass slide was first cleaned by piranha solution consisting of 4 parts of H_2SO_4 to 1 part of 30 %H_2O_2 at 60^oC (Caution: Piranha solution is extremely caustic. Use only with extreme care.) The glass surface then was derivatized with APTMS by immersing it into 10 mM methanolic solution of this organosilane. After 2 h, the glass slide was removed and rinsed with CH_3OH and deionized water to remove unbound monomers from the surface. After air drying, the slide was covered with a piece of tape with punched holes forming wells on the surface and each well was filled with 20 μL of SA (50μg mL^{-1}). After incubating overnight in a humid chamber, the slide was then rinsed with PBST (PBS with 0.05% Tween 20) and PBS, which were used in all washing procedures. Blocking was performed by adding the BSA solution and incubation for 1 h in a humid chamber. After rinsing, each well was incubated for 2 hs with 20 μL per well of BHHCT-Eu-DPBT doped Ag@SiO_2 nanocomposites or, in the control experiments, BHHCT-Eu-DPBT doped SiO_2 nanoshells without Ag cores. The slide was washed again with PBS buffer and stored at 4^oC before measurement. All operations were performed at room temperature.

Characterization

The absorption spectra of $Ag@SiO_2$ nanocomposites and hollow silica nanoshells in the solution were measured using a Cary spectrophotometer (Cary 5000 UV-Vis-NIR, Varian Inc.). Transmission Electron microscopy (TEM) images were taken on a PHILIPS CM10 system at an accelerating voltage of 100 kV. The samples were prepared by placing a drop of dilute ethanol dispersion of the nanocomposites and nanoshells on the surface of a copper grid. Scanning electron microscopy (SEM) images were taken by using a JEOL-JEM-6480 LA at an accelerating voltage of 200 kV. Fluorescence spectra of samples in the solution were obtained using a Fluorolog-Tau-3 system with 450W Xe lamp excitation. The spectral width was set to 8 nm. The emission spectra were excited at 365 nm and recorded over a range of 500-670 nm. Fluorescence lifetime was measured using a purpose-built UV epi-fluorescence microscopy system ($\times$10 objective; dichroic beam splitter (Zeiss, FT395)). A high-power UV LED (NCCU033A; Nichia Corp. Japan) with $\sim$250 mW power at 365 nm ($\Delta\lambda$ 10nm) was used for excitation. In this work the UV LED was operated in a pulsed mode (1 kHz, 100 μs, 10% duty cycle). In the lifetime measurements, a pair of filters (excitation band pass filter FF01-355/40-25 and emission bandpass filter FF01-607/36-25 BP, from Semrock, http://www.semrock.com/) was employed to suppress the long decay time noise generated from the UV LED. A silicon photomultiplier (SPMT) detector (SPMMini100, SensL, www.sensl.com) was positioned after the eyepiece, so that the long lifetime luminescence could be recorded as previously described. The values of lifetime were derived by a bi-exponential curve fitting (Origin 8.0 software) with the residual error function $\times$2 value of less than than 1.0. For the fluorescence imaging measurements, the glass coverslips were first soaked in a 4:1 (v/v) mixture of concentrated H_2SO_4 and 30%H_2O_2 overnight, extensively rinsed with water, sonicated in absolute ethanol for 2 min, dried in air. A dilute solution of the sample suspensions was dispersed on the precleaned coverslips. All measurements were performed using a time-gated UV epi-fluorescence microscopy system. The images of samples were recorded using a NIS-Elements BR 300 CCD camera (Nikon Instruments Inc. USA) at 2 s per frame. The imaging was performed using a $\times$60 objective and the time-gating was achieved by

using mechanical chopper (C995 Optical Chopper from Terahertz Technologies) operating at 2.5 kHz and positioned before CCD camera. This chopper was also acting as a trigger for the pulsed UV LED. The collected colour images were analyzed using only red channel whose spectral width overlaps with the 614 nm emission of Eu chelates. All measurements were performed in the dark at room temperature.

Results and discussion

The typical TEM images show as-prepared Ag@SiO_2 core-shell nanostructure with a dark contrast silver core and a light contrast silica shell. These verified the presence of the silica shell and the Ag core and provided information about their respective sizes, (see Fig. 11.2). The silica shell thickness used here gave average metal-fluorophore distances of 12 nm, 25 nm and 57 nm. In addition, as-prepared Ag colloids with different sizes were used as Ag cores with average diameters of 33 nm, 52 nm and 81 nm, as measured in the Ag@SiO_2 system. It is worth noting that 200 nm and 1000 nm long rod-shaped particles have also been observed, however, the number of rods is very low, less than 1% of the total number of particles.

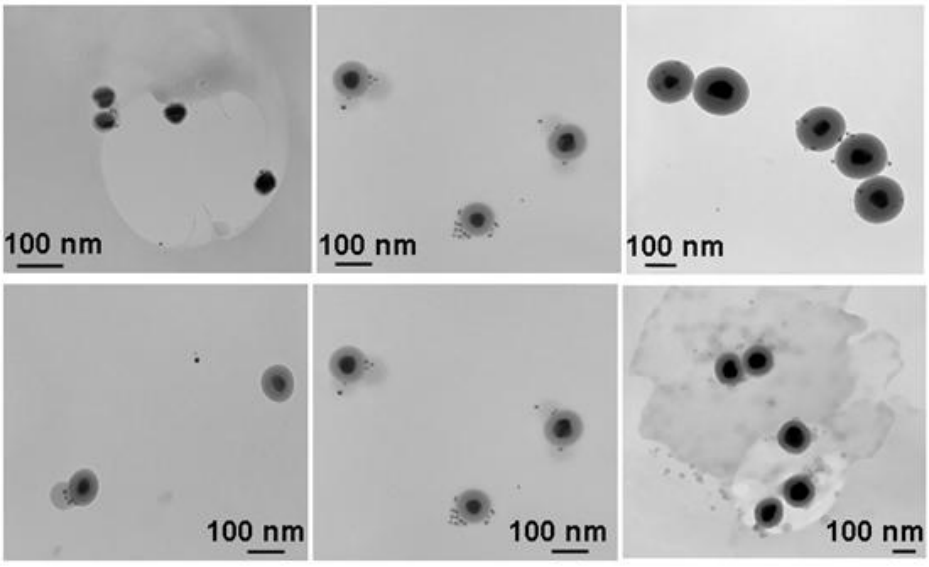

Figure 8.2: TEM images of Ag@SiO_2 nanocomposites with different thickness of silica shells (upper panel, from left to right: ∼12 nm, ∼25 nm and ∼57 nm) and Ag-core sizes (lower panel, from left to right: ∼33 nm, ∼52 nm and ∼81 nm).

Figure 11.3 shows the absorption spectra of the citrate-protected silver colloids and Ag@SiO_2 nanostructures with different silica shell thickness measured by using

UV-visible spectroscopy. Before coating, the Ag colloids had a characteristic surface plasmon peak at ∼425 nm. As the shell thickness is increased, there is a red shift to ∼450 nm in the position of the absorption maximum, due to the increase in the refractive index of silica around the particles. When the silica shell is sufficiently large, scattering becomes significant, resulting in a strong increase in the absorbance at shorter wavelengths. This effect promotes a blue shift of the surface plasmon band up to ∼432 nm and a weakening of its apparent intensity [272]. The absorption spectra of Ag@SiO_2 nanostructures with different Ag core sizes are displayed in Figure 11.3b . The surface plasmon absorption peak at ∼450 nm wavelengths was observed with Ag core of ∼33 nm. When the size of the silver core is increased, the plasmon absorption peak shifts towards longer wavelengths up to 484 nm. This could be attributed to the following reason: the formation of larger Ag colloids will result in a red shift of their plasmon absorption peak [269]. The etching process leads to the formation of a hollow silica shell, as has been shown for the same reaction on silica-coated Au nanoparticles [271]. Note that the dissolution of the core requires the transport through the silica shell of both molecular oxygen and cyanide ions, and for complete dissolution outward diffusion of silver cyanide complex anions. The decrease in the absorption of the light is shown (see Fig. 11.3c) as the solution changes from turbid yellow to colorless and essentially transparent. The inset in Figure 11.3c provides another evidence for the effectiveness of such etching process where Ag cores have been completely removed from the interiors in ∼1 day to leave behind silica nanoshells with fully intact wall structures.

Now we discuss the first of our key results, the demonstration of fluorescence enhancement of BHHCT-Eu-DPBT by tuning the metal-fluorophore distance and Ag-core size. The typical emission spectra of BHHCT-Eu-DPBT in Ag@SiO_2 nanocomposites where silica shell is ∼25 nm and Ag core is ∼52 nm, as well as the reference control without Ag core are presented in Figure 11.4. Fluorescence enhancement for all samples were calculated and shown in Table 8.1 and Table 8.2. We checked that in such nanocomposites the spectral shape of the emission is unchanged compared to Eu in solution, with the emission maximum typical of Eu^{3+} centered around 614 nm. For

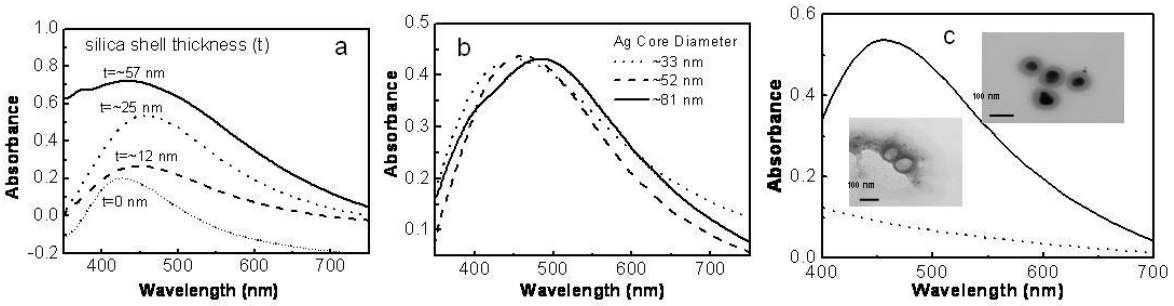

Figure 8.3: UV-visible absorption spectra of Ag@SiO_2 nanocomposites with different silica shell thickness (a), Ag core sizes (b) and hollow silica nanoshells (c). Insets are TEM images of the corresponding Ag@SiO_2 nanocomposites and SiO_2 nanoshells.

the samples with different SiO_2 shell thickness, a ∼10.7-fold increase for the silica shell thickness of ∼12 nm was obtained compared to the sample without the silver core. When the silica shell thickness was increased to ∼25 nm, the optimal fluorescence enhancement of ∼9.5 fold was observed. When this thickness reached up to ∼57 nm, a slight decrease (∼4.3 fold) in the fluorescence enhancement occurred (see Table 8.1). It's also worth noting that the fluorescence enhancement factors at shorter wavelengths of 580 nm and 589 nm were relatively higher compared to that 614 nm, with a marked decrease observed at 652 nm. This is consistent with the fact that a relatively stronger MEF effect is observed for wavelengths closer to the plasmon resonance for the silver nanoparticles. Furthermore, we also established the effects of Ag-core size on the fluorescence enhancement induced by metal nanostructures near fluorophores. In order to quantify this effect, we adjusted the size of Ag cores in Ag@SiO_2 nanocomposites from ∼20 nm to ∼100 nm. By comparing the sample with different Ag-core sizes with the corresponding reference control, we obtained the different fluorescence enhancement extent (see Table 8.2). The enhancement at 614 nm is slightly increased (∼2.0 fold) by Ag@SiO_2 nanocomposites with the Ag core of ∼33 nm compared to the reference sample without the Ag core. The optimal fluorescence enhancement of ∼10.7 fold occurred with the Ag core of ∼52 nm. Further increase in the Ag-core size caused a slight decrease in the fluorescence enhancement. A ∼8.4 fold increase in fluorescence intensity was observed with the Ag core of ∼81 nm.

For a more complete characterization of the effect of Ag@SiO_2 nanocomposites on

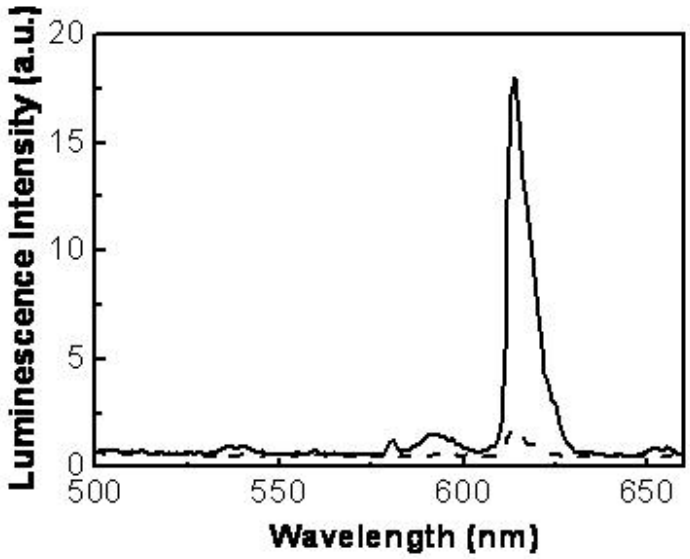

FIGURE 8.4: Luminescence intensities observed from BHHCT-Eu-DPBT-doped Ag@SiO_2 nanocomposites with ∼25 nm silica shell and ∼52 nm Ag-core size (solid line) and nanoshells without Ag core (dashed line).

the fluorescence enhancement we carried out the measurements of fluorescence lifetimes. As discussed in the literature [108] metal enhanced fluorescence is characterized by an increase in the quantum yield and a decrease in the lifetime of a fluorophore located in the proximity of the metallic nanostructures. Fluorescence decay curves were acquired (see Fig. 11.5) for samples with and without Ag cores, and results show that Ag@SiO_2 nanocomposites showed a shorter lifetime compared to the corresponding hollow silica nanoshells (see Table 8.3 and 8.4). A ∼3.5-fold decrease in the lifetime of BHHCT-Eu-DPBT (from 212 μs to 60 μs) was obtained by optimizing the metal-fluorophore distance and Ag-core size (silica shell: ∼12 nm and Ag core: ∼52 nm). The lifetime results make it possible to individually investigate the impact of silver nanostructures on the excitation and emission enhancements. These two contributors are important because the enhancement of fluorescence observed close to the nanostructured silver is a result of two effects: an increase of a local electromagnetic field near silver nanoparticles, leading to increased excitation rate of fluorophores and an increase of the radiative decay rate (τ) of fluorophores close to metal nanostructures, reflected both in the fluorescence lifetime and quantum yield [1]. The local electromagnetic field enhancement produces a higher excitation rate but it does not change the lifetime of the fluorophore;

Table 8.1: Fluorescence intensity enhancement analysis. t_{SiO2} denotes thickness of the silica shell, λ denotes the wavelength of the emission peak from Eu chelate.

	λ	580 nm	589 nm	614 nm	652 nm
	t_{SiO2}				
samples with fixed Ag-core	∼12 nm	11.2-fold	11.8-fold	10.7-fold	5.7-fold
size of ∼52 nm	∼25 nm	9.7-fold	9.3-fold	9.5-fold	4.5-fold
	∼57 nm	5.2-fold	5.8-fold	4.3-fold	3.4-fold
sample without Ag core	–	1.0-fold	1.0-fold	1.0-fold	1.0-fold

Table 8.2: Fluorescence intensity enhancement analysis. $D_{Ag-core}$ denotes denotes the diameter of Ag core, λ denotes the wavelength of the emission peak from Eu chelate.

	λ	580 nm	589 nm	614 nm	652 nm
	$D_{Ag-core}$				
samples with the silica shell	∼33 nm	1.6-fold	2.6-fold	2.0-fold	1.8-fold
thickness of ∼12 nm	∼52 nm	11.2-fold	11.8-fold	10.7-fold	5.7-fold
	∼81 nm	10.5-fold	12.5-fold	8.4-fold	2.6-fold
sample without Ag core	–	1.0-fold	1.0-fold	1.0-fold	1.0-fold

this effect is referred as excitation enhancement (E_{ex}). The second effect is referred as emission enhancement (E_{em}), increasing the quantum yield and reducing the lifetime of the fluorophore [1]. Results shown in Figure 11.4 and Figure 11.5 are in accordance with these arguments. The radiative decay rate modification of BHHCT-Eu-DPBT in close proximity to the silver nanostructures is consistent with the previous reports on the MEF phenomenon and is due to the proximity of the fluorophores to the silver nanostructures.

We present here the theoretical background to interpret the obtained results of the luminescence (fluorescence) enhancement and lifetimes. The radiative properties of Eu ions, in solution, and in various molecular environments are well established [273]. The radiative rate, A, of the Eu ion is given by the relationship:

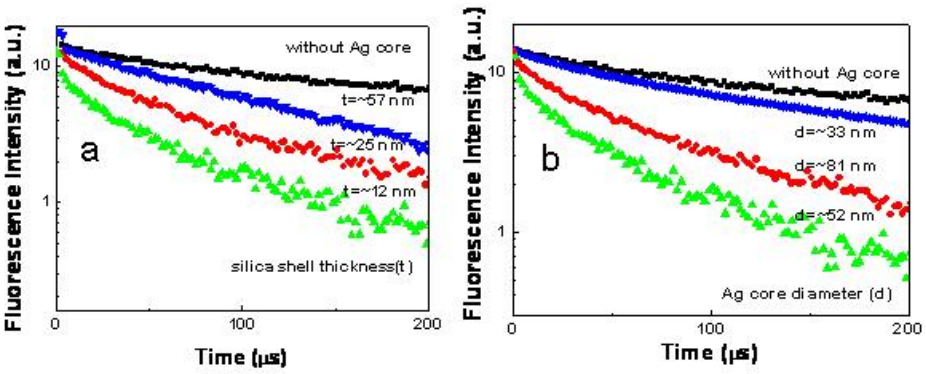

FIGURE 8.5: Representative fluorescence lifetime decay curves of BHHCT-Eu-DPBT in Ag@SiO_2 nanocomposites with different silica shell thickness(a) and with different Ag-core size(b).

TABLE 8.3: Fluorescence intensity decay analysis. t_{SiO2} denotes thickness of the silica shell, $\tau_{1,2}$ denotes decay times of the two lifetime components, τ is the average lifetime.

	t_{SiO2}	$\tau_1(\mu s)$	$\tau_2(\mu s)$	$\tau(\mu s)$
Eu-BHHCT-DBPT in the solution	–	306±4	33±2	301±3
Eu-BHHCT-DBPT-doped hollow silica nanoshell	–	216±3	32±2	212±2
Eu-BHHCT-DBPT-doped Ag@SiO_2	∼12 nm	60±4	5±3	60±3
nanostructures with fixed	∼25 nm	104±4	28±1	101±2
Ag-core size of ∼52 nm	∼57 nm	164±3	36±3	161±3

$$A = \frac{4e^2\omega^3}{3\hbar c^3}\frac{1}{2J+1}\chi\sum\lambda\Omega_\lambda\left\langle {}^5D_0\left\|U^\lambda\right\|{}^7F_J\right\rangle^2 \quad (8.1)$$

Here, e is the electronic charge, ω is the angular frequency of transition, $\hbar$ is the Planck's constant divided by 2π, c is the velocity of light, χ is the Lorentz local field correction given by $\chi = n(n^2+2)^2/9$, with the refractive index of silica n=1.5, $\left\langle {}^5D_0\left\|U^\lambda\right\|{}^7F_J\right\rangle^2$ are the reduced square matrix elements whose values are 0.0032 and 0.0023, for the states observed here with J=2 and 4, respectively [274]. The symbols Ω_λ denote Judd-Ofelt parameters. The expression for the radiative rate shown here is applicable to ions in a homogeneous dielectric and it is proportional to the density of photon states (producing the factor Ω^3 in the expression for A). The immediate

Table 8.4: Fluorescence intensity decay analysis. $D_{Ag-core}$ denotes the diameter of Ag core, $\tau_{1,2}$ denotes decay times of the two lifetime components, τ is the average lifetime.

	$D_{Ag-core}$	$\tau_1(\mu s)$	$\tau_2(\mu s)$	$\tau(\mu s)$
Eu-BHHCT-DBPT in the solution	–	306±4	33±2	301±3
Eu-BHHCT-DBPT-doped hollow silica nanoshell	0	216±3	32±2	212±2
Eu-BHHCT-DBPT-doped Ag@SiO_2	∼33 nm	187±4	3±1	185±3
nanostructures with silica shell	∼52 nm	60±4	5±1	60±2
thickness of ∼12 nm	∼81 nm	122±3	18±2	119±2

molecular environment has an effect on the emission of the Eu ion, and this is reflected in the modified radiative rates for various individual transitions, and consequently in changed relative intensities of the fluorescence bands attributed to various transitions in the $^5D_0 \rightarrow ^7F_J$ multiplet. The integrated intensities of the $^5D_0 \rightarrow ^7F_{0-4}$ transitions, I_{i-j}, are given by:

$$I_{i-j} = \hbar\omega_{i-j} A_{i-j} N_i \tag{8.2}$$

Here, i, j denote the initial ($^5D_0$) and final ($^7F_{0-4}$) levels, $\hbar\omega_{i-j}$ is the transition energy, A_{i-j} is the spontaneous transition rate and N_i is the population of the $^5D_0$ emitting level. The rates A_{i-j} can be retrieved from the relevant fluorescence intensities, by noting that the magnetic dipole transition $^5D_0 \rightarrow ^7F_1$ is insensitive to local molecular environment and can be used as a reference for the entire spectrum. Therefore the experimental spontaneous transition rates, A_{0J}, can be calculated as:

$$A_{0J} = A_{01} \frac{I_{0-J}}{I_{0-1}} \frac{\upsilon_{01}}{\upsilon_{0J}} \tag{8.3}$$

Here, υ_{01} and υ_{0J} are the median energies of the relevant transitions and the value of spontaneous emission rate A_{01} in silica empty shells (n=1.5) is 50 s^{-1} [273]. The total radiative rate A_{rad} is the sum of all rates A_{0J}, for all the observed transitions. The nonradiative rate is obtained by noting that the measured lifetime is related to

the radiative, A_{rad}, and nonradiative rate, A_{nrad} as:

$$\frac{1}{\tau} = A_{rad} + A_{nrad} \tag{8.4}$$

This method makes it possible to calculate the radiative and nonradiative rates in samples without metal. We emphasise, however, that the above expression of A implies that the local density of photon states was taken as in a homogenous dielectric. Thus a similar calculation or radiative rate can be carried out in metal core particles, however the radiative rates must be modified to take account of the changed density of photon states due to the presence of the metal. Equation /8.2/ indicates that the ′molecular′ rates obtained by applying Equations /8.1/, /8.3/ and /8.4/ needs to be multiplied by the observed fluorescence enhancement factor. This makes it possible to calculate the radiative rates, while nonradiative rates and the quantum yield in metal core particles are derived from Equation /8.4/.

It is worth emphasizing that thanks to the strong MEF, the synthesised Ag@SiO_2 nanocomposites doped with Eu were bright enough to be observed individually. This is documented in Figure 11.6 which shows the fluorescence images of nanocomposites with 52 nm Ag core and 25 nm SiO_2 shell (Fig. 11.6a) and corresponding control sample without Ag core (Fig. 11.6b). The sample with Ag@SiO_2 composites shows well-separated bright spots while in the control sample they are visibly darker. Because the solution used was diluted to the nanomole range, the collected images are likely to originate from single nanocomposites. In order to confirm this, we compared images of nanocomposites taken by the time-gated fluorescence microscope and SEM (Fig. 11.6c, d, e). They clearly demonstrate that each measured dot in the microscope image was, indeed, a single nanocomposite. The average value of the peak intensity in the fluorescent core/shell nanocomposites observed in these images was approximately ∼8.9-fold higher than that of the corresponding silica nanoshells, while in the ensemble measurement a similar factor of 9.5 was obtained.

In order to demonstrate the utility of these nanocomposites in biological applications, we carried out a fluorescent bioassay using streptavidin-biotin binding. To this aim the nanocomposites with 12 nm SiO_2 shell and with (or without) 52 nm Ag core

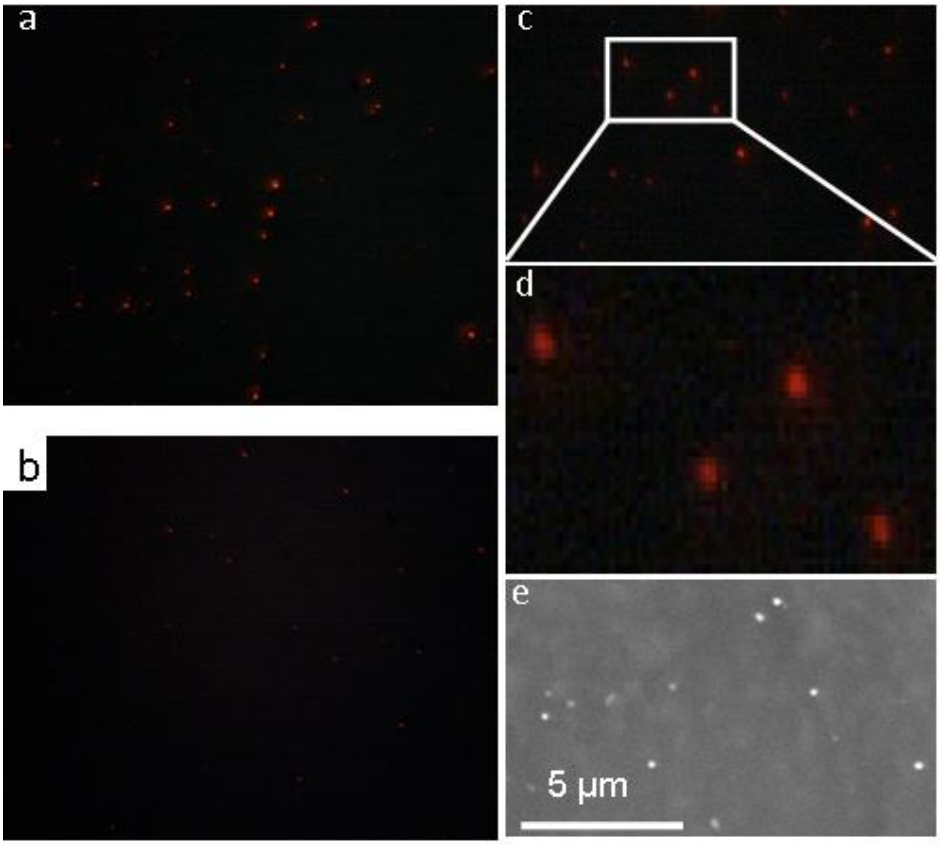

Figure 8.6: Time-gated luminescence images of single nanocomposites. a) BHHCT-Eu-DPBT-doped Ag@SiO_2 with 25 nm silica shell and 52 nm Ag core. b) BHHCT-Eu-DPBT-doped hollow nanocomposites with 25 nm silica shell and without 52 nm Ag core. c) Original red spots from BHHCT-Eu-DPBT-doped Ag@SiO_2 single nanocomposites. d) The enlarged image of spots in the square. e) Scanning electron microscope image of BHHCT-Eu-DPBT-doped Ag@SiO_2 nanocomposites. Data taken with ×60 magnification in the time-gated fluorescence microscope and 2 s exposure time.

were conjugated with biotynilated IgG antibody molecules. These were presented to streptavidin-coated glass slides where they were bound due to the avidin-biotin recognition mechanism (Fig. 11.7a, b). The enhancement factors were obtained by comparing the fluorescence intensity of bioassays with and without the Ag core at the same experimental conditions. The enhancement factor observed at high excitation intensity of 32.3 mW/cm^2 was ∼120 times (Fig. 11.8). This value is comparable although slightly lower than that from the nanocomposite suspension for the same excitation intensity (146 times). This phenomenon might be due to the effect of strong steric hindrance between the rigid nanocomposites and the solid-phase surface since biotin in this case

was tightly immobilised on the surface of the nanocomposites.

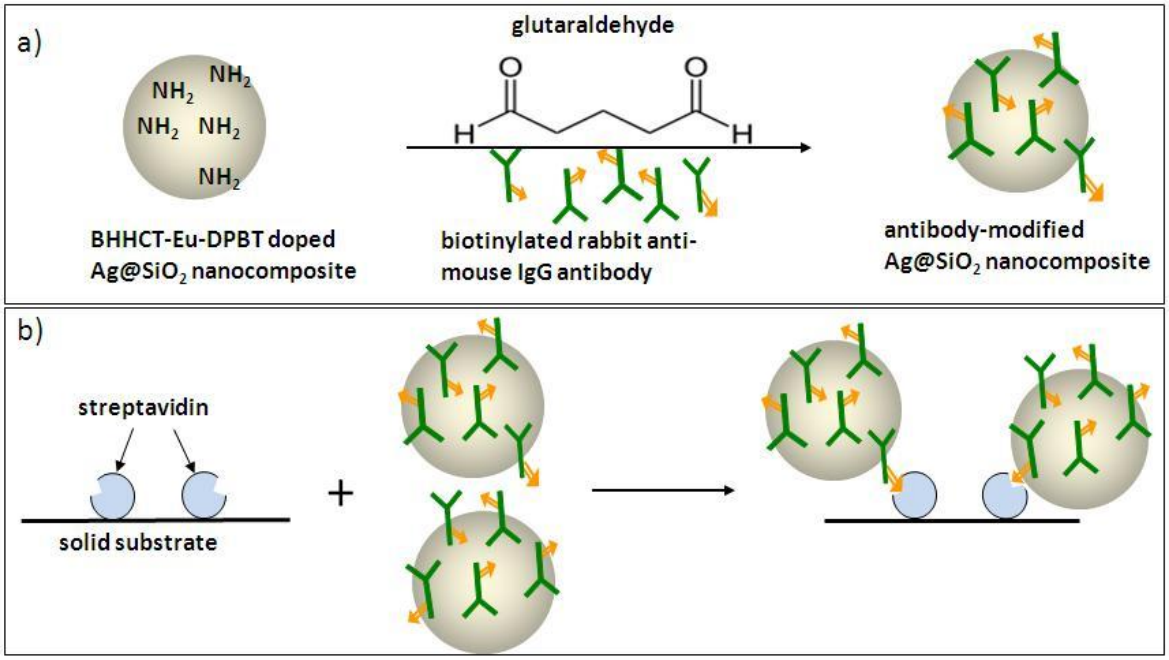

FIGURE 8.7: Schematic representation of conjugation of BHHCT-Eu-DPBT-doped Ag@SiO_2 nanocomposites with biotinylated antibody(a) and bioassay using Ag@SiO_2 nanocomposites as labels.

Conclusions

In conclusion, we successfully demonstrated an ultrabright time-gatable nanocomposite bioprobe by doping the Eu chelate, BHHCT-Eu-DPBT into Ag@SiO_2 core-shell nanostructures. We showed feasibility of bioassays with such probes and quantitatively interpreted the characterisation results. Such structures show a number of advantages in applications as bioprobes. The silica nanoparticles (<100 nm in diameter) are compatible with amino and carboxyl terminations on the surface, and suitable for immunoassays of molecular targets and cell labeling. Moreover, the lifetimes of doped Eu chelates in such core-shell nanocomposites, despite a strong decrease due to the proximity to a metal, still remain much longer than cellular autofluorescence, and therefore time-gating of fluorescence can be very effective to produce greatly improved signal to noise ratios. Finally, these nanocomposites are highly resilient to photobleaching/saturation, and can be used at high laser powers, where they offer greatly amplified fluorescence compared with nanoparticles without plasmonic effects. All these features

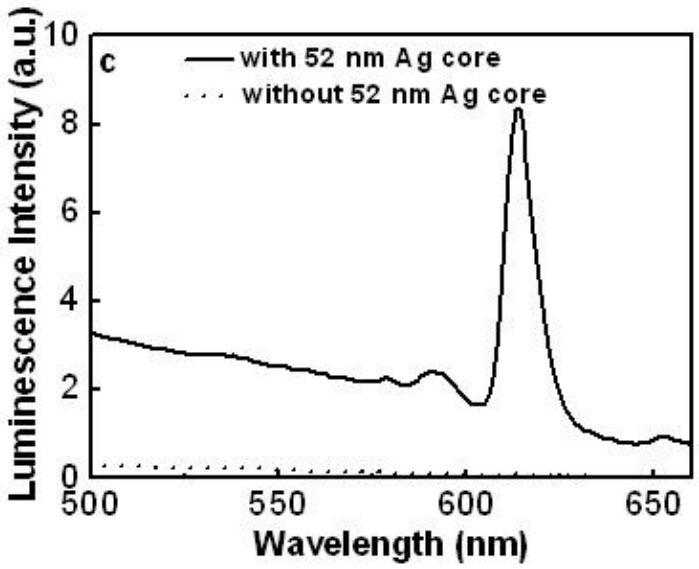

Figure 8.8: Luminescence spectra of nanocomposite-labeled antibody after bioassay. Solid line - BHHCT-Eu-DPBT-doped Ag@SiO_2 with 12 nm silica shell and 52 nm Ag core, dotted line - BHHCT-Eu-DPBT-doped hollow nanocomposites with 12 nm silica shell and without 52 nm Ag core.

pave the way for breaking new grounds in bioassays and bioimaging.

9

Conclusion

Summary

The work through my PhD project demonstrated the MEF technique and its bilogical applications. By using two kinds of MEF substrates, Ag nanostructure-coated silica beads and Ag@SiO_2 nanostructures, we investigated the feasibility of enhanced luminescence induced by silver nanostructures in bioassays and bioimaging and obtained high luminescence enhancement.

Development of MEF substrates

Firstly we fabricated micro-scaled silica beads coated with nanostructured silver, suitable for flow cytometry detection. In our method, a seed Au colloid is first covalently bound to (3-aminopropyl)-trimethoxysilane (APTMS) modified silica beads (400 nm and 5 μm in diameter), which enables controlled growth of uniform silver nanoparticles attached to the beads surface. Then silver enhancer solution was applied

to those Au colloids. The thickness of the silver layer overcoating was controlled by the duration of the silver enhancing step. By using a model immunoassay with a fluorescently labeled antibody, the commercial dye (Alexa 430) was attached to the surface of these silica beads.

In order to further evaluate the effect of silver nanoparticles on fluorescence intensity from fluorophores nearby, we developed another type MEF substrate, Ag-core/silica-shell nanocomposites, where both the silver-fluorophore distance and the Ag-core size were adjusted to optimize the fluorescence enhancement. This is achieved in the following way. Firstly, the thickness of the first silica shell is controlled by using different amount of tetraethyl orthosilicate (TEOS) which is able hydrolyze to generate silica sols on the surfaces of silver nanoparticles. To facilitate this reaction ammonia is added as a catalyst for hydrolysis and condensation of TEOS. Once the core has been covered with the first shell, the APS-linked BHHCT-Eu-DPBT (APS-BHHCT-Eu-DPBT) is then covalently linked to a second, thinner exterior silica shell (see Fig.11.1). Such system of layers makes it possible to systematically investigate the fluorescence enhancement of Eu chelates by Ag. Furthermore, the Ag-core size is varied by the growth of citrate-reduced silver colloids using metal deposition, which is an effective way of modifying the particle size. The fluorescence intensity enhancement from BHHCT-Eu-DPBT is also optimized by adjusting the Ag core size.

Feasibility of these MEF substrates used in different biological applications as fluorescence enhancer

In order to investigate the potential applications of enhanced fluorescence induced by these silver nanostructures in bioassays and bioimaging, we carried out a series of experiments using them and obtained satisfactory results which are consistant with those reported previously.

Firstly, we have demonstrated the use of silver nanostructures on the silica beads surface as an amplification mechanism for a flow cytometry bead immunoassay. The Ag-coated silica beads after 3 min silver enhancing time produced strong (8.5-fold and 10.1-fold) enhancement factor of emission intensity of Alexa 430 fluorophore excited at 430 nm for 400 nm and 5 μm beads respectively. The emission intensity increase

was accompanied by 3.5 times reduction in the lifetime of a fluorophore confirming the MEF mechanism of enhancement. Both 400 nm and 5 μm beads were compatible with flow cytometry readout at 488 nm, although lower enhancement factors of 3.0 and 3.7 were obtained, which were consistent with less favourable overlap of the plasmon resonance with 488 nm excitation wavelength used in the flow cytometry experiment. Based on these results, we expect that such beads will have much broader applicability. Firstly, silver nanoparticles are excellent biocompatible surfaces for the immobilization of enzymes and nucleic acids, and extension of the present work to, for example amplified DNA and RNA assays should be straightforward. These have implications not only for the detection of disease biomarkers and genes, but also microbial assays. Other advantages of the beads such as the ability to be used with various enrichment and filtering systems to concentrate the analyte are further enhanced by our fluorescence amplification approach.

Secondly, we applied such bead substrates to a simple bioassay and time-gated fluorescence imaging of Giardia lamblia cells stained by BHHCT $-$ Eu^{3+}. The fluorescence spectra of BHHCT $-$ Eu^{3+}-labeled SA-BSA on the silver nanostructures show a varying level of fluorescence enhancement depending on silver deposition times. The origin of the observed enhancement is attributed to an increased excitation rate from the local field enhanced by the interaction of incident light with nanostructures and higher quantum yield from the increase of the intrinsic decay rate of the fluorophore. Both the emission and excitation enhancement contributed the total enhancement values on the order of 11, which was accompanied by 2 times decrease of the lifetime. Moreover, we have also shown that silica beads with Ag nanostructures were able to produce brighter fluorescence images of cells labeled by BHHCT $-$ Eu^{3+}, suggesting that such substrates are applicable in the time-gated fluorescence bio-imaging. These important features will pave the way for application of such enhanced lanthanide chelates in many areas of life sciences and biotechnology such as fluorescence-based biological assays and bio-imaging.

Apart from the conventional dye (Alexa 430) and lanthanide chelate (BHHCT $-$ Eu^{3+}), we also applied these Ag nanostructure-coated silica beads to upconversion(UC)

nanoparticles, $NaYF_4 : Yb, Er$, and evaluated their performance on luminescence enhancement in the simple bioassay detection. In our method, silver nanostructures were firstly coated on 400 nm silica bead surface, followed by deposition of silica beads on the glass slide. In order to examine the effect on the UC luminescence intensity and lifetime induced by Ag nanostructures near $NaYF_4 : Yb, Er$ nanoparticles, we developed a bioassay, where streptavdin (SA)-labeled UC nanoparticles were bound to the biotinlyated anti-mouse IgG antibody, on the silica beads. This assay was carried out with and without Ag enhancement at the same experimental conditions. The strong luminescence enhancement (∼4.4-fold for the green mission and ∼3.5-fold for the red emission) was obtained. It indicates that both the local electromagnetic field and the rediative decay rates are enhanced and the combination of them results in strong UC luminescence. In addition, we also demonstrated the shorter luminescence lifetimes (∼2.0-fold for green emission and ∼2.2-fold for red emission, respectively) induced by clustered Ag nanostructures, confirming MEF applied to UC luminescence enhancement. These phenomena proved that UC emission can be enhanced by noble metals such as Ag, which promise potential application of metal-UC nanoparticle composites in bioassays.

As another type of MEF substrate, $Ag@SiO_2$ nanocomposites, we conducted a series of experiments to explore and optimize the fluorescence enhancement induced by them. The fluorescence was conferred by europium chelate, BHHCT-Eu-DPBT covalently bound into an outer part of the SiO_2 layer surrounding the silver core. This design enhances the europium signal intensity by more than one order of magnitude, and accelerates the decay time from 0.3 ms down to 60 μs, at low excitation conditions. Surprisingly, at high excitation intensities, the same nanocomposites showed greatly increased fluorescence enhancement factors of up to 145, due to significantly increased radiative rates in samples with metal cores, from about 700 s^{-1} in control samples to over 5000 s^{-1}. Single bioprobes were bright enough to be observed in time-gated fluorescence microscopy under 365 nm LED excitation. A simple bioassay using avidin-biotin binding system was also carried out with luminescence enhancement factor of ∼120 folds. Such nanocomposites show a number of advantages in applications as

bioprobes. The silica nanoparticles (<100 nm in diameter) are compatible with amino and carboxyl terminations on the surface, and suitable for immunoassays of molecular targets and cell labeling. Moreover, the lifetimes of doped Eu chelates in such core-shell nanocomposites, despite a strong decrease due to the proximity to a metal, still remain much longer than cellular autofluorescence, and therefore time-gating of fluorescence can be very effective to produce greatly improved signal to noise ratios. Finally, these nanocomposites are highly resilient to photobleaching/saturation, and can be used at high laser powers, where they offer greatly amplified fluorescence compared with nanoparticles without plasmonic effects.

References

[1] H. Raether. *Surface plasma oscillations and their applications.* Phys. Thin Films **9**, 145 (1977).

[2] S. Link and M. El-Sayed. *Shape and size dependence of radiative, non-radiative and photothermal properties of gold nanocrystals.* International Reviews in Physical Chemistry **19**(3), 409 (2000).

[3] J. Lakowicz. *Radiative decay engineering: biophysical and biomedical applications.* Anal. Biochem **298**(1), 1 (2001).

[4] F. Xie, M. Baker, and E. Goldys. *Homogeneous silver-coated nanoparticle substrates for enhanced fluorescence detection.* J. Phy. Chem. B **110**(46), 23085 (2006).

[5] E. Matveeva, Z. Gryczynski, J. Malicka, I. Gryczynski, and J. Lakowicz. *Metal-enhanced fluorescence immunoassays using total internal reflection and silver island-coated surfaces.* Analytical Biochemistry **334**(2), 303 (2004).

[6] E. Matveeva, I. Gryczynski, A. Barnett, Z. Leonenko, J. Lakowicz, and Z. Gryczynski. *Metal particle-enhanced fluorescent immunoassays on metal mirrors.* Anal. Biochem **363**(2), 239 (2007).

[7] J. Zhang, E. Matveeva, I. Gryczynski, Z. Leonenko, and J. Lakowicz. *Metal-enhanced fluoroimmunoassay on a silver film by vapor deposition.* Journal of Physical Chemistry B **109**(16), 7969 (2005).

[8] C. Sabanayagam and J. Lakowicz. *Increasing the sensitivity of DNA microarrays by metal-enhanced fluorescence using surface-bound silver nanoparticles.* Nucleic Acids Research **35**(2), 13 (2007).

[9] J. Zhang, Y. Fu, D. Liang, R. Zhao, and J. Lakowicz. *Enhanced fluorescence images for labeled cells on silver island films.* Langmuir **24**(21), 12452 (2008).

[10] K. Aslan, M. Wu, J. Lakowicz, and C. Geddes. *Metal enhanced fluorescence solution-based sensing platform 2: fluorescent core-shell* Ag@SiO_2 *nanoballs.* J. Fluores **17**(2), 127 (2007).

[11] J. Zhang, J. Malicka, I. Gryczynski, and J. Lakowicz. *Oligonucleotide-displaced organic monolayer-protected silver nanoparticles and enhanced luminescence of their salted aggregates.* Anal. Biochem **330**(1), 81 (2004).

[12] J. Suyver, A. Aebischer, D. Biner, P. Gerner, J. Grimm, S. Heer, K. Kramer, C. Reinhard, and H. Gudel. *Novel materials doped with trivalent lanthanides and transition metal ions showing near-infrared to visible photon upconversion.* Optical Materials **27**(6), 1111 (2005).

[13] P. Corstjens, S. Li, M. Zuiderwijk, K. Kardos, W. Abrams, R. Niedbala, and H. Tanke. *Infrared up-converting phosphors for bioassays.* In *IEEE Proc. Nanobiotechnol*, vol. 152, pp. 64–72 (2005).

[14] H. Zijlmans, J. Bonnet, J. Burton, K. Kardos, T. Vail, R. Niedbala, and H. Tanke. *Detection of cell and tissue surface antigens using up-converting phosphors: a new reporter technology.* Analytical Biochemistry **267**(1), 30 (1999).

[15] J. Hampl, M. Hall, N. Mufti, Y. Yao, D. MacQueen, W. Wright, and D. Cooper. *Upconverting phosphor reporters in immunochromatographic assays.* Analytical Biochemistry **288**(2), 176 (2001).

[16] M. Zuiderwijk, H. Tanke, R. Sam Niedbala, and P. Corstjens. *An amplification-free hybridization-based DNA assay to detect Streptococcus pneumoniae utilizing the up-converting phosphor technology.* Clinical Biochemistry **36**(5), 401 (2003).

[17] K. Kuningas, T. Ukonaho, H. Pakkila, T. Rantanen, J. Rosenberg, T. Lovgren, and T. Soukka. *Upconversion fluorescence resonance energy transfer in a homogeneous immunoassay for estradiol.* Anal. Chem **78**(13), 4690 (2006).

[18] D. Chatterjee, A. Rufaihah, and Y. Zhang. *Upconversion fluorescence imaging of cells and small animals using lanthanide doped nanocrystals.* Biomaterials **29**(7), 937 (2008).

[19] S. Lim, R. Riehn, W. Ryu, N. Khanarian, C. Tung, D. Tank, and R. Austin. *In vivo and scanning electron microscopy imaging of upconverting nanophosphors in Caenorhabditis elegans.* Nano Lett **6**(2), 169 (2006).

[20] T. Ukonaho, T. Rantanen, L. Jämsen, K. Kuningas, H. Päkkilä, T. Lövgren, and T. Soukka. *Comparison of infrared-excited up-converting phosphors and europium nanoparticles as labels in a two-site immunoassay.* Analytica Chimica Acta **596**(1), 106 (2007).

[21] R. Niedbala, T. Vail, H. Feindt, S. Li, and J. Burton. *Multiphoton up-converting phosphors for use in rapid immunoassays* **3913**, 193 (2000).

[22] J. Lakowicz. *Radiative decay engineering 5: metal-enhanced fluorescence and plasmon emission.* Anal. Biochem **337**(2), 171 (2005).

[23] K. Sokolov, G. Chumanov, and T. Cotton. *Enhancement of molecular fluorescence near the surface of colloidal metal films.* Anal. Chem **70**(18), 3898 (1998).

[24] C. Geddes, A. Parfenov, D. Roll, J. Fang, and J. Lakowicz. *Electrochemical and laser deposition of silver for use in metal-enhanced fluorescence.* Langmuir **19**(15), 6236 (2003).

[25] C. Geddes, H. Cao, I. Gryczynski, Z. Gryczynski, J. Fang, and J. Lakowicz. *Metal-enhanced fluorescence (MEF) due to silver colloids on a planar surface: potential applications of indocyanine green to in vivo imaging.* J. Phys. Chem. A **107**(18), 3443 (2003).

[26] K. Aslan, Z. Leonenko, J. Lakowicz, and C. Geddes. *Fast and slow deposition of silver nanorods on planar surfaces: application to metal-enhanced fluorescence.* J. Phys. Chem. B **109**(8), 3157 (2005).

[27] K. Drexhage. *Influence of a dielectric interface on fluorescence decay time.* J. Lumin **1**(2), 693 (1970).

[28] S. Nie and S. Emory. *Probing single molecules and single nanoparticles by surface-enhanced Raman scattering.* Science **275**(5303), 1102 (1997).

[29] K. Kneipp, H. Kneipp, V. Kartha, R. Manoharan, G. Deinum, I. Itzkan, R. Dasari, and M. Feld. *Detection and identification of a single DNA base molecule using surface-enhanced Raman scattering (SERS).* Phys. Rev. E **57**(6), 6281 (1998).

[30] J. Lakowicz, Y. Shen, S. D́Auria, J. Malicka, J. Fang, Z. Gryczynski, and I. Gryczynski. *Radiative decay engineering 2. effects of silver island films on fluorescence intensity, lifetimes, and resonance energy transfer.* Anal. Biochem **301**(2), 261 (2002).

[31] J. Lakowicz. *Principles of fluorescence spectroscopy* (Springer, 2006).

[32] H. Macleod. *Thin-film optical filters* (Institute of Physics: Philadelphia, USA, 2001).

[33] D. Wolfgang and G. Wolfgang. *Flow-through chamber for photometers to measure and count particles in a dispersion medium* (1971).

[34] S. Pyne, X. Hu, K. Wang, E. Rossin, T. Lin, L. Maier, C. Baecher-Allan, G. McLachlan, P. Tamayo, and D. Hafler. *Automated high-dimensional flow cytometric data analysis.* Proceedings of the National Academy of Sciences **106**(21), 8519 (2009).

[35] M. Melamed, T. Lindmo, and M. Mendelsohn. *Flow cytometry and sorting* (Wiley-Liss New York etc., 1990).

[36] D. Sandison and W. Webb. *Background rejection and signal-to-noise optimization in confocal and alternative fluorescence microscopes.* Applied Optics **33**(4), 603 (1994).

[37] C. Sheppard and D. Shotton. *Image formation in the confocal laser scanning microscope.* Confocal Laser Scanning Microscopy; Springer-Verlag, New York Inc.: New York pp. 15–31 (1997).

[38] S. Inoué and K. Spring. *Video microscopy: the fundamentals* (Springer, 1997).

[39] W. Denk, D. Piston, W. Webb, and J. Pawley. *Handbook of biological confocal microscopy.* Plenum Press, New York (1995).

[40] M. Minsky. *Memoir on inventing the confocal scanning microscope.* Scanning **10**(4), 128 (1988).

[41] J. Pawley and B. Masters. *Handbook of biological confocal microscopy.* J. Biomed Optics **13**, 029902 (2008).

[42] D. Patel and C. McGhee. *Contemporary in vivo confocal microscopy of the living human cornea using white light and laser scanning techniques: a major review.* Clinical & Experimental Ophthalmology **35**(1), 71 (2007).

[43] W. Becker, A. Bergmann, K. Koenig, and U. Tirlapur. *Picosecond fluorescence lifetime microscopy by TCSPC imaging.* In *Proc. SPIE*, vol. 4262, pp. 414–419 (2001).

[44] W. Becker, K. Benndorf, A. Bergmann, C. Biskup, K. Konig, U. Tirplapur, and T. Zimmer. *FRET measurements by TCSPC laser scanning microscopy.* In *ECBO*, vol. 1 (2002).

[45] W. Becker, A. Bergmann, C. Biskup, T. Zimmer, N. Klocker, and K. Benndorf. *Multi-wavelength TCSPC lifetime imaging.* In *Proc. SPIE*, vol. 4620, pp. 79–84 (2002).

[46] E. Buurman, R. Sanders, A. Draaijer, H. Gerritsen, J. Van Veen, P. Houpt, and Y. Levine. *Fluorescence lifetime imaging using a confocal laser scanning microscope.* Scanning **14**(3), 155 (1992).

[47] J. Sytsma, J. Vroom, C. De Grauw, and H. Gerritsen. *Time-gated fluorescence lifetime imaging and microvolume spectroscopy using two-photon excitation.* J. Microscopy **191**(1), 39 (1998).

[48] A. Ruck, F. Dolp, C. Happ, R. Steiner, and M. Beil. *Fluorescence liftime imaging (FLIM) using ps-pulsed diode lasers in laser scanning microscopes.* In *Manipulation and Analysis of Biomolecules, Cells, and Tissues.*, vol. 4962, pp. 160–167 (2003).

[49] M. Straub and S. Hell. *Fluorescence lifetime three-dimensional microscopy with picosecond precision using a multifocal multiphoton microscope.* Appl. Phys. Lett. **73**, 1769 (1998).

[50] P. So, T. French, W. Yu, K. Berland, C. Dong, and E. Gratton. *Time-resolved fluorescence microscopy using two-photon excitation.* Bioimaging **3**(2) (1995).

[51] P. So, T. French, and E. Gratton. *Frequency domain time-resolved microscope using a fast-scan CCD camera.* In *Proc. SPIE*, vol. 2137, p. 83 (1994).

[52] K. Carlsson and A. Liljeborg. *Simultaneous confocal lifetime imaging of multiple fluorophores using the intensity-modulated multiple-wavelength scanning (IMS) technique.* J. Microscopy **191**(2), 119 (1998).

[53] K. Carlsson and J. Philip. *Theoretical investigation of the signal-to-noise ratio for different fluorescence lifetime imaging techniques.* In *Proc. SPIE*, vol. 4622, pp. 70–78 (2002).

[54] C. Geddes and J. Lakowicz. *Metal-enhanced fluorescence.* J. Fluoresc **12**(2), 121 (2002).

[55] J. Kümmerlen, A. Leitner, H. Brunner, F. Aussenegg, and A. Wokaun. *Enhanced dye fluorescence over silver island films: analysis of the distance dependence.* Molecular Physics **80**(5), 1031 (1993).

[56] K. Sokolov, G. Chumanov, and T. Cotton. *Enhancement of molecular fluorescence near the surface of colloidal metal films.* Anal. Chem **70**(18), 3898 (1998).

[57] M. Kerker. *The optics of colloidal silver: something old and something new.* Journal of colloid and interface science **105**(2), 297 (1985).

[58] M. Faraday. *The Bakerian lecture: experimental relations of gold (and other metals) to light.* Philosophical Transactions of the Royal Society of London pp. 145–181 (1857).

[59] E. Hutter and J. Fendler. *Exploitation of localized surface plasmon resonance.* Adv. Mater **16**(19), 1685 (2004).

[60] J. Kottmann, O. Martin, D. Smith, and S. Schultz. *Spectral response of plasmon resonant nanoparticles with a non-regular shape.* Opt. Express **6**(11), 213 (2000).

[61] J. Mock, D. Smith, and S. Schultz. *Local refractive index dependence of plasmon resonance spectra from individual nanoparticles.* Nano Lett **3**(4), 485 (2003).

[62] A. Kirsch, V. Subramaniam, A. Jenei, and T. Jovin. *Fluorescence resonance energy transfer detected by scanning near-field optical microscopy.* J. Microscopy **194**(2), 448 (1999).

[63] S. Garoff, D. Weitz, M. Alvarez, and J. Gersten. *Electrodynamics at rough metal surfaces: photochemistry and luminescence of adsorbates near metal-island films.* J. Chem. Phys **81**, 5189 (1984).

[64] J. Lakowicz, Y. Shen, S. DAuria, J. Malicka, J. Fang, Z. Gryczynski, and I. Gryczynski. *Radiative decay engineering:: 2. Effects of silver island films on fluorescence intensity, lifetimes, and resonance energy transfer.* Anal. Biochem **301**(2), 261 (2002).

[65] K. Aslan, J. Lakowicz, and C. Geddes. *Rapid deposition of triangular silver nanoplates on planar surfaces: application to metal-enhanced fluorescence.* J. Phys. Chem. B **109**(13), 6247 (2005).

[66] J. Zhang, Y. Fu, M. Chowdhury, and J. Lakowicz. *Metal-enhanced single-molecule fluorescence on silver particle monomer and dimer: coupling effect between metal particles.* Nano Lett **7**(7), 2101 (2007).

[67] K. Aslan, Z. Leonenko, J. Lakowicz, and C. Geddes. *Fast and slow deposition of silver nanorods on planar surfaces: application to metal-enhanced fluorescence.* J. Phys. Chem. B **109**(8), 3157 (2005).

[68] C. Geddes, A. Parfenov, D. Roll, J. Fang, and J. Lakowicz. *Electrochemical and laser deposition of silver for use in metal-enhanced fluorescence.* Langmuir **19**(15), 6236 (2003).

[69] J. Zhang and J. Lakowicz. *Metal-enhanced fluorescence of an organic fluorophore using gold particles.* Anal. Biochem **337**, 171 (2005).

[70] I. Gryczynski, J. Malicka, Z. Gryczynski, and J. Lakowicz. *Surface plasmon-coupled emission with gold films.* Journal of Physical Chemistry B-Condensed Phase **108**(33), 12568 (2004).

[71] M. Chowdhury, K. Ray, S. Gray, J. Pond, and J. Lakowicz. *Aluminum nanoparticles as substrates for metal-enhanced fluorescence in the ultraviolet for the label-free detection of biomolecules.* Analytical Chemistry **81**(4), 1397 (2009).

[72] T. Förster. *Intermolecular energy migration and fluorescence.* Ann. Phys **2**, 55 (1948).

[73] J. Lakowicz, J. Malicka, S. *Ď*Auria, and I. Gryczynski. *Release of the self-quenching of fluorescence near silver metallic surfaces.* Anal. Biochem **320**(1), 13 (2003).

[74] J. Malicka, I. Gryczynski, C. Geddes, and J. Lakowicz. *Metal-enhanced emission from indocyanine green: a new approach to in vivo imaging.* J. Biomed. Opt **8**, 472 (2003).

[75] I. Gryczynski, J. Malicka, E. Holder, N. DiCesare, and J. Lakowicz. *Effects of metallic silver particles on the emission properties of* $[Ru(bpy)_3]^{2+}$. Chem. Phys. Lett **372**(3-4), 409 (2003).

[76] J. Lakowicz, J. Malicka, and I. Gryczynski. *Silver particles enhance emission of fluorescent DNA oligomers.* Bio Techniques **34**(1), 62 (2003).

[77] P. Brown and D. Botstein. *Exploring the new world of the genome with DNA microarrays.* Nature Genetics **21**(1 Suppl), 33 (1999).

[78] F. Komurian-Pradel, G. Paranhos-Baccala, M. Sodoyer, P. Chevallier, B. Mandrand, V. Lotteau, and P. André. *Quantitation of HCV RNA using real-time PCR and fluorimetry.* J. Virological Methods **95**(1-2), 111 (2001).

[79] N. Walker. *A technique whose time has come.* Science **296**(5567), 557 (2002).

[80] M. Difilippantonio and T. Ried. *Technicolor genome analysis* **7**, 291 (2003).

[81] J. Malicka, I. Gryczynski, and J. Lakowicz. *DNA hybridization assays using metal-enhanced fluorescence.* Biochemical and Biophysical Research Communications **306**(1), 213 (2003).

[82] K. Aslan and C. Geddes. *Microwave-accelerated metal-enhanced fluorescence: Platform technology for ultrafast and ultrabright assays.* Anal. Chem **77**(24), 8057 (2005).

[83] J. Zhang and J. Lakowicz. *A model for DNA detection by metal-enhanced fluorescence from immobilized silver nanoparticles on solid substrate.* J.Phys. Chem. B **110**(5), 2387 (2006).

[84] R. Weissleder, C. Tung, U. Mahmood, and A. Bogdanov. *In vivo imaging of tumors with protease-activated near-infrared fluorescent probes.* Nat. Biotech **17**, 375 (1999).

[85] I. Chen and A. Ting. *Site-specific labeling of proteins with small molecules in live cells.* Current Opinion in Biotechnology **16**(1), 35 (2005).

[86] T. Nagano and T. Yoshimura. *Bioimaging of nitric oxide.* Chem. Rev **102**(4), 1235 (2002).

[87] J. Zhang, Y. Fu, and J. Lakowicz. *Single cell fluorescence imaging using metal plasmon-coupled probe.* Bioconjugate Chem **18**(3), 800 (2007).

[88] E. Moal, E. Fort, S. Lévêque-Fort, F. Cordelières, M. Fontaine-Aupart, and C. Ricolleau. *Enhanced fluorescence cell imaging with metal-coated slides.* J. Biophysical **92**(6), 2150 (2007).

[89] J. Zhang, Y. Fu, D. Liang, K. Nowaczyk, R. Zhao, and J. Lakowicz. *Single-cell fluorescence imaging using metal plasmon-coupled probe 2: single-molecule counting on lifetime image.* Nano Lett **8**(4), 1179 (2008).

[90] K. Aslan, J. Lakowicz, H. Szmacinski, and C. Geddes. *Metal-enhanced fluorescence solution-based sensing platform.* J. Fluores **14**(6), 677 (2004).

[91] J. Chen, M. Iannone, M. Li, J. Taylor, P. Rivers, A. Nelsen, K. Slentz-Kesler, A. Roses, and M. Weiner. *A microsphere-based assay for multiplexed single nucleotide polymorphism analysis using single base chain extension.* Genome Research **10**(4), 549 (2000).

[92] A. Craciun, C. Vermeer, H. Eisenwiener, N. Drees, and M. Knapen. *Evaluation of a bead-based enzyme immunoassay for the rapid detection of osteocalcin in human serum.* Clinical Chemistry **46**(2), 252 (2000).

[93] J. Nolan and F. Mandy. *Suspension array technology: new tools for gene and protein analysis.* Cellular and molecular biology (Noisy-le-Grand, France) **47**(7), 1241 (2001).

[94] L. Yang, D. Tran, and X. Wang. *BADGE, beads array for the detection of gene expression, a high-throughput diagnostic bioassay* (2001).

[95] C. Vedrine, C. Caraion, C. Lambert, and C. Genin. *Cytometric bead assay of cytokines in sepsis: a clinical evaluation.* Cytometry Part B Clinical Cytometry. **60**(1), 14 (2004).

[96] M. Lowe, A. Spiro, Y. Zhang, and R. Getts. *Multiplexed, particle-based detection of DNA using flow cytometry with 3 DNA dendrimers for signal amplification.* Cytometry (2) (2004).

[97] Y. Zhao, X. Zhao, C. Sun, J. Li, R. Zhu, and Z. Gu. *Encoded silica colloidal crystal beads as supports for potential multiplex immunoassay.* Anal. Chem **80**(5), 1598 (2008).

[98] C. Huang, W. Wong, L. Li, C. Chiang, B. Chen, and S. Li. *Genotyping of chlamydia trachomatis by microsphere suspension array.* Journal of Clinical Microbiology (2008).

[99] V. Salas, B. Edwards, and L. Sklar. *Advances in multiple analyte profiling.* Advances in Clinical Chemistry **45**, 47 (2008).

[100] B. Battersby and M. Trau. *Optically encoded particles and their applications in multiplexed biomedical assays.* Australian Journal of Chemistry **60**, 343 (2007).

[101] S. Dunbar. *Applications of luminex@xMAP technology for rapid, high-throughput multiplexed nucleic acid detection.* Clinica Chimica Acta **363**(1-2), 71 (2006).

[102] M. Seul, C. Chau, H. Huang, S. Banerjee, J. Yang, and Y. Hong. *Arrays of microparticles and methods of preparation thereof* (2008). US Patent 7,335,153.

[103] E. Matveeva, I. Gryczynski, A. Barnett, Z. Leonenko, J. Lakowicz, and Z. Gryczynski. *Metal particle-enhanced fluorescent immunoassays on metal mirrors.* Analytical Biochemistry **363**(2), 239 (2007).

[104] F. Xie, M. Baker, and E. Goldys. *Homogeneous silver-coated nanoparticle substrates for enhanced fluorescence detection.* J. Phys. Chem. B **110**(46), 23085 (2006).

[105] N. Jana, L. Gearheart, and C. Murphy. *Seed-mediated growth approach for shape-controlled synthesis of spheroidal and rod-like gold nanoparticles using a surfactant template.* Advanced Materials **13**(18) (2001).

[106] S. Westcott, S. Oldenburg, T. Lee, and N. Halas. *Formation and adsorption of clusters of gold nanoparticles onto functionalized silica nanoparticle surfaces.* Langmuir **14**(19), 5396 (1998).

[107] J. Brummer, R. Langlois, M. Loth, A. Popov, R. Schmitz, G. Taft, R. Tanke, and A. Wruck. *Controlling synthesis of nanostructured silver aggregates by light.* Nanophotonics for Information Systems (Conference paper) (2004).

[108] S. Oldenburg, R. Averitt, S. Westcott, and N. Halas. *Nanoengineering of optical resonances.* Chemical Physics Letters **288**(2-4), 243 (1998).

[109] J. Bünzli and C. Piguet. *Taking advantage of luminescent lanthanide ions.* Chemical Society Reviews **34**(12), 1048 (2005).

[110] J. Yuan, K. Matsumoto, and H. Kimura. *A new tetradentate β-diketonate-europium chelate that can be covalently bound to proteins for time-resolved fluoroimmunoassay.* Anal. Chem **70**(3), 596 (1998).

[111] D. Bornhop, D. Hubbard, M. Houlne, C. Adair, G. Kiefer, B. Pence, and D. Morgan. *Fluorescent tissue site-selective lanthanide chelate, Tb-PCTMB for enhanced imaging of cancer.* Anal. Chem **71**(14), 2607 (1999).

[112] S. Petoud, S. Cohen and J. Bunzli. *Stable lanthanide luminescence agents highly emissive in aqueous solution: multidentate 2-hydroxyisophthalamide complexes of* Sm^{3+}, Eu^{3+}, Tb^{3+}, Dy^{3+}. J. Am. Chem. Soc **125**, 13324 (2003).

[113] N. Weibel, L. Charbonniere, M. Guardigli, A. Roda, and R. Ziessel. *Engineering of highly luminescent lanthanide tags suitable for protein labeling and time-resolved luminescence imaging.* J. Am. Chem. Soc **126**(15), 4888 (2004).

[114] J. Karvinen, V. Laitala, M. Makinen, O. Mulari, J. Tamminen, J. Hermonen, P. Hurskainen, and I. Hemmila. *Fluorescence quenching-based assays for hydrolyzing enzymes. application of time-resolved fluorometry in assays for caspase, helicase, and phosphatase.* Anal. Chem **76**(5), 1429 (2004).

[115] J. Lakowicz. *Radiative decay engineering: biophysical and biomedical applications.* Anal. Biochem **298**(1), 1 (2001).

[116] I. Gryczynski, J. Malicka, E. Holder, N. DiCesare, and J. Lakowicz. *Effects of metallic silver particles on the emission properties of* $[Ru(bpy)_3]^{2+}$. Chem. Phys. Lett **372**(3-4), 409 (2003).

[117] I. Gryczynski, E. Matveeva, P. Sarkar, S. Bharill, J. Borejdo, W. Mandecki, I. Akopova, and Z. Gryczynski. *Metal enhanced fluorescence on silicon wafer substrates.* Chemical Physics Letters **462**(4-6), 327 (2008).

[118] P. Muthu, I. Gryczynski, Z. Gryczynski, J. Talent, I. Akopova, and J. Borejdo. *Decreasing photobleaching by silver nanoparticles on metal surfaces: application to muscle myofibrils.* Journal of Biomedical Optics **13**, 014023 (2008).

[119] K. Ray, M. Chowdhury, and J. Lakowicz. *Aluminum nanostructured films as substrates for enhanced fluorescence in the ultraviolet-blue spectral region.* Anal. Chem **79**(17), 6480 (2007).

[120] A. Parfenov, I. Gryczynski, J. Malicka, C. Geddes, and J. Lakowicz. *Enhanced fluorescence from fluorophores on fractal silver surfaces.* Journal of Physical Chemistry B **107**(34), 8829 (2003).

[121] C. Geddes, A. Parfenov, D. Roll, I. Gryczynski, J. Malicka, and J. Lakowicz. *Silver fractal-like structures for metal-enhanced fluorescence: enhanced fluorescence*

intensities and increased probe photostabilities. Journal of Fluorescence **13**(3), 267 (2003).

[122] J. Lakowicz, J. Malicka, S. ĎAuria, and I. Gryczynski. *Release of the self-quenching of fluorescence near silver metallic surfaces.* Analytical Biochemistry **320**(1), 13 (2003).

[123] J. Lakowicz, I. Gryczynski, J. Malicka, Z. Gryczynski, and C. Geddes. *Enhanced and localized multiphoton excited fluorescence near metallic silver islands: metallic islands can increase probe photostability.* Journal of Fluorescence **12**(3), 299 (2002).

[124] J. Malicka, I. Gryczynski, C. Geddes, and J. Lakowicz. *Metal-enhanced emission from indocyanine green: a new approach to in vivo imaging.* Journal of Biomedical Optics **8**, 472 (2003).

[125] J. Lakowicz, J. Malicka, and I. Gryczynski. *Silver particles enhance emission of fluorescent DNA oligomers.* BioTechniques **34**(1), 62 (2003).

[126] B. Maliwal, J. Malicka, I. Gryczynski, Z. Gryczynski, and J. Lakowicz. *Fluorescence properties of labeled proteins near silver colloid surfaces.* Biopolymers (Biospectroscopy) **70**, 585 (2003).

[127] Y. Sun, H. Jiu, D. Zhang, J. Gao, B. Guo, and Q. Zhang. *Preparation and optical properties of* Eu(III) *complexes J-aggregate formed on the surface of silver nanoparticles.* Chemical Physics Letters **410**(4-6), 204 (2005).

[128] H. Nabika, S. Deki, A. Krummel, P. Mukherjee, M. Zanni, Y. Finkelstein, A. Saig, A. Danon, J. Koresh, and H. Xia. *Enhancing and quenching functions of silver nanoparticles on the luminescent properties of europium complex in the solution phase.* Journal of Physical Chemistry B **107**(35), 9161 (2003).

[129] Y. Sun, Z. Zheng, Q. Yan, J. Gao, H. Jiu, and Q. Zhang. *Effects of Ag colloidal nanoparticles on luminescent properties of* Eu(III) *β-diketone.* Materials Letters **60**(21-22), 2756 (2006).

[130] J. Yuan, S. Sueda, R. Somazawa, K. Matsumoto, and K. Matsumoto. *Structure and luminescence properties of the tetradentate β-diketonate–europium (III) complexes.* Chemistry Letters **32**(6), 492 (2003).

[131] J. Yuan, G. Wang, H. Kimura, and K. Matsumoto. *Highly sensitive time-resolved fluoroimmunoassay of human immunoglobulin E by using a new europium fluorescent chelate as a label.* Anal. Biochem **254**(2), 283 (1997).

[132] D. Jin, R. Connally, and J. Piper. *Practical time-gated luminescence flow cytometry. I: concepts.* Cytometry Part A (10) (2007).

[133] D. Jin, R. Connally, and J. Piper. *Long-lived visible luminescence of UV LEDs and impact on LED excited time-resolved fluorescence applications.* Journal of Physics D-Applied Physics **39**(3), 461 (2006).

[134] R. Leif, S. Yang, D. Jin, J. Piper, L. Vallarino, J. Williams, and R. Zucker. *Calibration beads containing luminescent lanthanide ion complexes.* Journal of Biomedical Optics **14**, 024022 (2009).

[135] D. Jin, J. Piper, R. Leif, S. Yang, B. Ferrari, J. Yuan, G. Wang, L. Vallarino, and J. Williams. *Time-gated flow cytometry: an ultra-high selectivity method to recover ultra-rare-event μ-targets in high-background biosamples.* Journal of Biomedical Optics **14**, 024023 (2009).

[136] J. Song, T. Atay, S. Shi, H. Urabe, and A. Nurmikko. *Large enhancement of fluorescence efficiency from* CdSe/ZnS *quantum dots induced by resonant coupling to spatially controlled surface plasmons.* Nano Lett **5**(8), 1557 (2005).

[137] A. Sigel. *The lanthanides and their interrelations with biosystems* (CRC, 2003).

[138] K. Li, M. Stockman, and D. Bergman. *Enhanced second harmonic generation in a self-similar chain of metal nanospheres.* Physical Review B **72**(15), 153401 (2005).

[139] J. R. Lakowicz. *Principles of fluorescence spectroscopy* (Kluwer Academic/Plenum: New York, 1999).

[140] P. Muthu, I. Gryczynski, Z. Gryczynski, J. Talent, I. Akopova, K. Jain, and J. Borejdo. *Decreasing photobleaching by silver island films: application to muscle.* Analytical Biochemistry **366**(2), 228 (2007).

[141] H. Mertens, A. Koenderink, and A. Polman. *Plasmon-enhanced luminescence near noble-metal nanospheres: comparison of exact theory and an improved Gersten and Nitzan model.* Physical Review B **76**(11), 115123 (2007).

[142] E. Moal, E. Fort, S. Lévêque-Fort, F. Cordelières, M. Fontaine-Aupart, and C. Ricolleau. *Enhanced fluorescence cell imaging with metal-coated slides.* Biophysical journal **92**(6), 2150 (2007).

[143] F. Auzel. *Materials and devices using double-pumped-phosphors with energy transfer.* Proceedings of the IEEE **61**(6), 758 (1973).

[144] V. Ovsyankin and P. Feofilov. *On the mechanism of adding of electronic excitations in doped crystals.* Sov. Phys. JETP Lett **3**, 322 (1966).

[145] M. Pollnau, D. Gamelin, S. Lüthi, H. Güdel, and M. Hehlen. *Power dependence of upconversion luminescence in lanthanide and transition-metal-ion systems.* Physical Review B **61**(5), 3337 (2000).

[146] F. Auzel. *Upconversion and anti-stokes processes with f and d ions in solids.* Chem. Rev. **104**, 139 (2004).

[147] J. Suyver, A. Aebischer, D. Biner, P. Gerner, J. Grimm, S. Heer, K. Krämer, C. Reinhard, and H. Güdel. *Novel materials doped with trivalent lanthanides and transition metal ions showing near-infrared to visible photon upconversion.* Optical Materials **27**(6), 1111 (2005).

[148] D. Gamelin and H. Gudel. *Upconversion processes in transition metal and rare earth metal systems.* Topics in Current Chemistry **214**, 1 (2001).

[149] W. Wright, N. Mufti, N. Tagg, R. Webb, and L. Schneider. *High-sensitivity immunoassay using a novel upconverting phosphor reporter.* In *SPIE Proceedings*, pp. 248–255 (SPIE International Society for Optical, 1997).

[150] S. Heer, K. Kompe, H. Gudel, and M. Haase. *Highly efficient multicolour upconversion emission in transparent colloids of lanthanide-doped* $NaYF_4$ *nanocrystals.* Advanced Materials(FRG) **16**(23), 2102 (2004).

[151] P. Corstjens, S. Li, M. Zuiderwijk, K. Kardos, W. Abrams, R. Niedbala, and H. Tanke. *Infrared up-converting phosphors for bioassays.* In *Nanobiotechnology, IEEE Proceedings*, vol. 152, pp. 64–72 (2005).

[152] J. Klostranec and W. Chan. *Quantum dots in biological and biomedical research: recent progress and present challenges.* Adv. Mater **18**, 1953 (2006).

[153] H. Zijlmans, J. Bonnet, J. Burton, K. Kardos, T. Vail, R. Niedbala, and H. Tanke. *Detection of cell and tissue surface antigens using up-converting phosphors: a new reporter technology.* Analytical Biochemistry **267**(1), 30 (1999).

[154] F. van de Rijke, H. Zijlmans, S. Li, T. Vail, A. Raap, R. Niedbala, and H. Tanke. *Up-converting phosphor reporters for nucleic acid microarrays.* Nature Biotechnology **19**, 273 (2001).

[155] O. Khalil, G. Cohn, G. Newman, J. Leary, F. He, L. Reece, M. Tanner, W. Coleman, C. Everett, and S. Robles. *In-vitro diagnostic instrumentation.* In *SPIE Proceedings*, vol. 3913, pp. 193–203 (2000).

[156] R. Niedbala, H. Feindt, K. Kardos, T. Vail, J. Burton, B. Bielska, S. Li, D. Milunic, P. Bourdelle, and R. Vallejo. *Detection of analytes by immunoassay using up-converting phosphor technology.* Analytical Biochemistry **293**(1), 22 (2001).

[157] M. Zuiderwijk, H. Tanke, R. Sam Niedbala, and P. Corstjens. *An amplification-free hybridization-based DNA assay to detect Streptococcus pneumoniae utilizing the up-converting phosphor technology.* Clinical Biochemistry **36**(5), 401 (2003).

[158] G. Yi, H. Lu, S. Zhao, Y. Ge, W. Yang, D. Chen, and L. Guo. *Synthesis, characterization, and biological application of size-controlled nanocrystalline* $NaYF_4 : Yb, Er$ *infrared-to-visible up-conversion phosphors.* Nano Lett **4**, 2191 (2004).

[159] S. Info, M. Nyk, R. Kumar, T. Ohulchanskyy, E. Bergey, and P. Prasad. *High contrast in vitro and in vivo photoluminescence bioimaging using near infrared to near infrared up-conversion in* Tm^{3+} *and* Yb^{3+} *doped fluoride nanophosphors.* Nano Lett **8**(11), 3834 (2008).

[160] *Up-conversion in rare-earth-doped systems: past, present, and future.*

[161] M. Malinowski, Z. Frukacz, M. Joubert, and B. Jacquier. *Blue up-conversion emission in* Yb^{3+} *sensitized* $YAG : Pr^{3+}$. Journal of Luminescence **75**(4), 333 (1997).

[162] D. Wang, Y. Guo, E. Zhang, X. Chao, L. Yu, J. Luo, W. Zhang, and M. Yin. *Synthesis and NIR-to-violet, blue, green, red upconversion fluorescence of* Er^{3+} : LaOBr. Journal of Alloys and Compounds **397**(1-2), 1 (2005).

[163] V. Rai, S. Rai, and D. Rai. *Optical studies of* Dy^{3+} *doped tellurite glass: observation of yellow-green upconversion.* Optics communications **257**(1), 112 (2006).

[164] K. Kramer, D. Biner, G. Frei, H. Gudel, M. Hehlen, and S. Luthi. *Hexagonal sodium yttrium fluoride based green and blue emitting upconversion phosphors.* Chemistry of Materials **16**(7), 1244 (2004).

[165] F. Auzel. *Upconversion and anti-stokes processes with f and d ions in solids.* Chem. Rev **104**(1), 139 (2004).

[166] M. Pollnau, D. Gamelin, S. Luthi, H. Gudel, and M. Hehlen. *Power dependence of upconversion luminescence in lanthanide and transition-metal-ion systems.* Physical Review B **61**(5), 3337 (2000).

[167] D. Gamelin and H. Gudel. *Design of luminescent inorganic materials: new photophysical processes studied by optical spectroscopy.* Acc. Chem. Res **33**(4), 235 (2000).

[168] H. Song, B. Sun, T. Wang, S. Lu, L. Yang, B. Chen, X. Wang, and X. Kong. *Three-photon upconversion luminescence phenomenon for the green levels in* Er^{3+}/Yb^{3+} *codoped cubic nanocrystalline yttria.* Solid State Communications **132**(6), 409 (2004).

[169] F. Vetrone, J. Boyer, J. Capobianco, A. Speghini, and M. Bettinelli. *Concentration-dependent near-infrared to visible upconversion in nanocrystalline and bulk* $Y_2O_3 : Er^{3+}$. Chemistry of Materials **15**(14), 2737 (2003).

[170] S. Singh, A. Singh, D. Kumar, O. Prakash, and S. Rai. *Efficient UV-visible upconversion emission in* Er^{3+}/Yb^{3+} *co-doped* La_2O_3 *nano-crystalline phosphor.* Applied physics. B, Lasers and optics **98**(1), 173 (2010).

[171] A. Patra, C. Friend, R. Kapoor, and P. Prasad. *Upconversion in* $Er^{3+} : ZrO_2$ *nanocrystals.* J. Phys. Chem. B **106**(8), 1909 (2002).

[172] A. Patra, C. Friend, R. Kapoor, and P. Prasad. *Fluorescence upconversion properties of* Er^{3+}*-doped* TiO_2 *and* $BaTiO_3$ *nanocrystallites.* Chem. Mater **15**(19), 3650 (2003).

[173] Y. Liu, W. Pisarski, S. Zeng, C. Xu, and Q. Yang. *Tri-color upconversion luminescence of Rare earth doped* $BaTiO_3$ *nanocrystals and lowered color separation.* Optics Express **17**(11), 9089 (2009).

[174] G. Yi, B. Sun, F. Yang, D. Chen, Y. Zhou, and J. Cheng. *Synthesis and characterization of high-efficiency nanocrystal up-conversion phosphors: ytterbium and erbium codoped lanthanum molybdate.* Chem. Mater **14**(7), 2910 (2002).

[175] S. Heer, O. Lehmann, M. Haase, and H. Gudel. *Blue, green, and red upconversion emission from lanthanide-doped* $LuPO_4$ *and* $YbPO_4$ *nanocrystals in a transparent colloidal solution.* Angewandte Chemie International Edition **42**(27), 3179 (2003).

[176] G. Yi, H. Lu, S. Zhao, Y. Ge, W. Yang, D. Chen, and L. Guo. *Synthesis, characterization, and biological application of size-controlled nanocrystalline* $NaYF_4 : Yb, Er$ *infrared-to-visible up-conversion phosphors.* Nano Letters **4**(11), 2191 (2004).

[177] Y. Zhang, X. Sun, R. Si, L. You, and C. Yan. *Single-crystalline and monodisperse* LaF_3 *triangular nanoplates from a single-source precursor.* Journal of the American Chemical Society **127**(10), 3260 (2005).

[178] J. Shan, X. Qin, N. Yao, and Y. Ju. *Synthesis of monodisperse hexagonal* $NaYF_4 : Yb, Ln$ *(*$Ln = Er, Ho$ *and* Tm*) upconversion nanocrystals in* TOPO. Nanotechnology **18**(44), 445607 (2007).

[179] J. Shan and Y. Ju. *A single-step synthesis and the kinetic mechanism for monodisperse and hexagonal-phase* $NaYF_4 : Yb, Er$ *upconversion nanophosphors.* Nanotechnology **20**, 275603 (2009).

[180] H. Qian and Y. Zhang. *Synthesis of hexagonal-phase core-shell* $NaYF_4$ *nanocrystals with tunable upconversion fluorescence.* Langmuir **24**(21), 12123 (2008).

[181] F. Vetrone, J. Boyer, J. Capobianco, A. Speghini, and M. Bettinelli. *Significance of Yb concentration on the upconversion mechanisms in codoped* $YO : Er, Yb$ *nanocrystals.* Journal of Applied Physics **96**, 661 (2004).

[182] X. Luo and W. Cao. *Ethanol-assistant solution combustion method to prepare* $La_2O_2S : Yb, Pr$ *nanometer phosphor.* Journal of Alloys and Compounds **460**(1-2), 529 (2008).

[183] L. Xu, Y. Yu, X. Li, G. Somesfalean, Y. Zhang, H. Gao, and Z. Zhang. *Synthesis and upconversion properties of monoclinic* $Gd_2O_3 : Er^{3+}$ *nanocrystals.* Optical Materials **30**(8), 1284 (2008).

[184] F. Zhang, Y. Wan, T. Yu, F. Zhang, Y. Shi, S. Xie, Y. Li, L. Xu, B. Tu, and D. Zhao. *Uniform nanostructured arrays of sodium Rare-earth fluorides*

for highly efficient multicolor upconversion luminescence. Angewandte Chemie International Edition **46**(42), 7976 (2007).

[185] F. Zhang, J. Li, J. Shan, L. Xu, and D. Zhao. *Shape, size, and phase-controlled Rare-earth fluoride nanocrystals with Optical up-conversion properties.* Chemistry–A European Journal **15**(41), 11010 (2009).

[186] G. Yi and G. Chow. *Colloidal* $LaF_3 : Yb, Er$*,* $LaF_3 : Yb, Ho$ *and* $LaF_3 : Yb, Tm$ *nanocrystals with multicolor upconversion fluorescence.* Journal of Materials Chemistry **15**(41), 4460 (2005).

[187] N. Zhuravleva, A. Eliseev, N. Sapoletova, A. Lukashin, U. Kynast, and Y. Tretyakov. *The synthesis of* EuF_3/TOPO *nanoparticles.* Materials Science & Engineering C **25**(5-8F), 549 (2005).

[188] N. Zhuravleva, N. Sapoletova, A. Eliseev, A. Lukashin, Y. Tretyakov, and U. Kynast. *The synthesis of monodisperse trioctylphosphine oxide-capped* EuF_3 *nanoparticles.* Optical Materials **28**(6-7), 606 (2006).

[189] R. Niedbala, T. Vail, H. Feindt, S. Li, and J. Burton. *Multiphoton up-converting phosphors for use in rapid immunoassays.* In *Proceedings of SPIE*, vol. 3913, p. 193 (2000).

[190] M. Ohmori and E. Matijevic. *Preparation and properties of uniform coated colloidal particles. VII. silica on hematite.* Journal of colloid and interface science **150**(2), 594 (1992).

[191] S. Sung, J. Chee, and E. Merrill. *Polymeric oxide films for improved bonding of titanium to silicate glass.* Ceramic Transactions **11**, 153 (1990).

[192] R. Abdul Jalil and Y. Zhang. *Biocompatibility of silica coated* $NaYF_4$ *upconversion fluorescent nanocrystals.* Biomaterials **29**(30), 4122 (2008).

[193] Z. Liu, G. Yi, H. Zhang, J. Ding, Y. Zhang, and J. Xue. *Monodisperse silica nanoparticles encapsulating upconversion fluorescent and superparamagnetic nanocrystals.* Chemical communications (Cambridge, England) (6), 694 (2008).

[194] G. Yi and G. Chow. *Water-soluble* $NaYF_4 : Yb, Er$ *(*Tm*)/*$NaYF_4$*/polymer core/shell/shell nanoparticles with significant enhancement of upconversion fluorescence.* Chem. Mater **19**(3), 341 (2007).

[195] L. Wang, Y. Zhang, and Y. Zhu. *One-pot synthesis and strong near-infrared upconversion luminescence of poly (acrylic acid)-functionalized* $YF_3 : Yb^{3+}/Er^{3+}$ *nanocrystals.* Nano Research **3**(5), 317 (2010).

[196] B. Ungun, R. PrudHomme, S. Budijon, J. Shan, S. Lim, Y. Ju, and R. Austin. *Nanofabricated upconversion nanoparticles for photodynamic therapy.* Optics Express **17**(1), 80 (2009).

[197] T. Zhang, J. Ge, Y. Hu, and Y. Yin. *A general approach for transferring hydrophobic nanocrystals into water.* Nano lett **7**(10), 3203 (2007).

[198] R. Naccache, F. Vetrone, V. Mahalingam, L. Cuccia, and J. Capobianco. *Controlled synthesis and water dispersibility of hexagonal phase* $NaGdF_4 : Ho^{3+}/Yb^{3+}$ *Nanoparticles.* Chem. Mater **21**(4), 717 (2009).

[199] F. Wang, D. Chatterjee, Z. Li, Y. Zhang, X. Fan, and M. Wang. *Synthesis of polyethylenimine/*$NaYF_4$ *nanoparticles with upconversion fluorescence.* Nanotechnology **17**, 5786 (2006).

[200] G. Yi and G. Chow. *Synthesis of hexagonal-phase* $NaYF_4 : Yb, Er$ *and* $NaYF_4 : Yb, Tm$ *nanocrystals with efficient up-conversion fluorescence.* Advanced Functional Materials **16**(18), 2324 (2006).

[201] M. Kamimura, D. Miyamoto, Y. Saito, K. Soga, and Y. Nagasaki. *Design of poly (ethylene glycol)/streptavidin coimmobilized upconversion nanophosphors and their application to fluorescence biolabeling.* Langmuir **24**(16), 8864 (2008).

[202] Z. Chen, H. Chen, H. Hu, M. Yu, F. Li, Q. Zhang, Z. Zhou, T. Yi, and C. Huang. *Versatile synthesis strategy for carboxylic acid- functionalized upconverting nanophosphors as biological labels.* J. Am. Chem. Soc **130**(10), 3023 (2008).

[203] H. Zhou, C. Xu, W. Sun, and C. Yan. *Clean and flexible modification strategy for carboxyl/aldehyde-functionalized upconversion nanoparticles and their optical applications.* Advanced Functional Materials **19**(24), 3892 (2009).

[204] L. Wang, R. Yan, Z. Huo, L. Wang, J. Zeng, J. Bao, X. Wang, Q. Peng, and Y. Li. *Fluorescence resonant energy transfer biosensor based on upconversion-luminescent nanoparticles.* Angewandte Chemie International Edition **44**(37), 6054 (2005).

[205] L. Wang and Y. Li. *Green upconversion nanocrystals for DNA detection.* Chem. Commu **2006**(24), 2557 (2006).

[206] T. Soukka, K. Kuningas, T. Rantanen, V. Haaslahti, and T. Lövgren. *Photochemical characterization of up-converting inorganic lanthanide phosphors as potential labels.* Journal of Fluorescence **15**(4), 513 (2005).

[207] J. Aubin. *Autofluorescence of viable cultured mammalian cells.* Journal of Histochemistry and Cytochemistry **27**(1), 36 (1979).

[208] P. Corstjens, M. Zuiderwijk, A. Brink, S. Li, H. Feindt, R. Niedbala, and H. Tanke. *Use of up-converting phosphor reporters in lateral-flow assays to detect specific nucleic acid sequences: a rapid, sensitive DNA test to identify human papillomavirus type 16 infection.* Clinical Chemistry **47**(10), 1885 (2001).

[209] K. Kuningas, T. Rantanen, T. Ukonaho, T. Lovgren, and T. Soukka. *Homogeneous assay technology based on upconverting phosphors.* Anal. Chem **77**(22), 7348 (2005).

[210] L. Wang, R. Yan, Z. Huo, L. Wang, J. Zeng, J. Bao, X. Wang, Q. Peng, and Y. Li. *Fluorescence resonant energy transfer biosensor based on upconversion-luminescent nanoparticles.* Angewandte Chemie(International ed. Print) **44**(37), 6054 (2005).

[211] K. Kuningas, T. Ukonaho, H. Pakkila, T. Rantanen, J. Rosenberg, T. Lovgren,

and T. Soukka. *Upconversion fluorescence resonance energy transfer in a homogeneous immunoassay for estradiol.* Anal. Chem **78**(13), 4690 (2006).

[212] K. Kuningas, H. Pakkila, T. Ukonaho, T. Rantanen, T. Lovgren, and T. Soukka. *Upconversion fluorescence enables homogeneous immunoassay in whole blood.* Clinical Chemistry **53**(1), 145 (2007).

[213] T. Rantanen, M. Järvenpää, J. Vuojola, K. Kuningas, and T. Soukka. *Fluorescence-quenching-based enzyme-activity assay by using photon upconversion.* Angewandte Chemie (International ed. in English) **47**(20), 3811 (2008).

[214] P. Zhang, S. Rogelj, K. Nguyen, and D. Wheeler. *Design of a highly sensitive and specific nucleotide sensor based on photon upconverting particles.* J. Am. Chem. Soc **128**(38), 12410 (2006).

[215] K. Kuningas, T. Rantanen, T. Ukonaho, T. Lovgren, and T. Soukka. *Homogeneous assay technology based on upconverting phosphors.* Anal. Chem **77**(22), 7348 (2005).

[216] J. Frangioni. *In vivo near-infrared fluorescence imaging.* Current Opinion in Chemical Biology **7**(5), 626 (2003).

[217] Q. de Chermont, C. Chanéac, J. Seguin, F. Pellé, S. Maîtrejean, J. Jolivet, D. Gourier, M. Bessodes, and D. Scherman. *Nanoprobes with near-infrared persistent luminescence for in vivo imaging.* Proceedings of the National Academy of Sciences **104**(22), 9266 (2007).

[218] K. Schenke-Layland, I. Riemann, O. Damour, U. Stock, and K. König. *Two-photon microscopes and in vivo multiphoton tomographs–powerful diagnostic tools for tissue engineering and drug delivery.* Advanced Drug Delivery Reviews **58**(7), 878 (2006).

[219] J. Boyer, L. Cuccia, and J. Capobianco. *Synthesis of colloidal upconverting* $NaYF_4$: Er^{3+}/Yb^{3+} *and* Tm^{3+}/Yb^{3+} *monodisperse nanocrystals.* Nano Lett **7**(3), 847 (2007).

[220] S. Lim, R. Riehn, W. Ryu, N. Khanarian, C. Tung, D. Tank, and R. Austin. *In vivo and scanning electron microscopy imaging of upconverting nanophosphors in Caenorhabditis elegans.* Nano Lett **6**(2), 169 (2006).

[221] R. Abdul Jalil and Y. Zhang. *Biocompatibility of silica coated* $NaYF_4$ *upconversion fluorescent nanocrystals.* Biomaterials **29**(30), 4122 (2008).

[222] P. Corstjens, M. Zuiderwijk, M. Nilsson, H. Feindt, R. Sam Niedbala, and H. Tanke. *Lateral-flow and up-converting phosphor reporters to detect single-stranded nucleic acids in a sandwich-hybridization assay.* Analytical Biochemistry **312**(2), 191 (2003).

[223] H. Hu, L. Xiong, J. Zhou, F. Li, T. Cao, and C. Huang. *Multimodal-luminescence core–shell nanocomposites for targeted imaging of tumor cells.* Chemistry–A European Journal **15**(14), 3577 (2009).

[224] R. Kumar, M. Nyk, T. Ohulchanskyy, C. Flask, and P. Prasad. *Combined optical and MR bioimaging using rare earth ion doped* $NaYF_4$ *nanocrystals.* Advanced Functional Materials **19**(6), 853 (2009).

[225] M. Nyk, R. Kumar, T. Ohulchanskyy, E. Bergey, and P. Prasad. *High contrast in vitro and in vivo photoluminescence bioimaging using near infrared to near infrared up-conversion in* Tm^{3+} *and* Yb^{3+} *doped fluoride nanophosphors.* Nano Letters **8**(11), 3834 (2008).

[226] M. Yu, F. Li, Z. Chen, H. Hu, C. Zhan, H. Yang, and C. Huang. *Laser scanning up-conversion luminescence microscopy for imaging cells labeled with rare-earth nanophosphors.* Analytical Chemistry **81**(3), 930 (2009).

[227] J. Feng, G. Shan, A. Maquieira, M. Koivunen, B. Guo, B. Hammock, and I. Kennedy. *Functionalized europium oxide nanoparticles used as a fluorescent label in an immunoassay for atrazine.* Anal. Chem **75**(19), 5282 (2003).

[228] Y. Liu, M. Summers, C. Edder, J. Fréchet, and M. McGehee. *Using resonance*

energy transfer to improve exciton harvesting in organic-inorganic hybrid photovoltaic cells. Advanced Materials **17**(24), 2960 (2005).

[229] S. Weiss. *Fluorescence spectroscopy of single biomolecules.* Science **283**(5408), 1676 (1999).

[230] J. Seifert, R. Connor, S. Kushon, M. Wang, and B. Armitage. *Spontaneous assembly of helical cyanine dye aggregates on DNA nanotemplates.* J. Am. Chem. Soc **121**(13), 2987 (1999).

[231] A. Alivisatos, W. Gu, and C. Larabell. *Quantum dots as cellular probes.* Biomedical Engineering **7** (2005).

[232] X. Michalet, F. Pinaud, L. Bentolila, J. Tsay, S. Doose, J. Li, G. Sundaresan, A. Wu, S. Gambhir, and S. Weiss. *Quantum dots for live cells, in vivo imaging, and diagnostics.* Science **307**(5709), 538 (2005).

[233] F. Wang and X. Liu. *Upconversion multicolor fine-tuning: visible to near-infrared emission from lanthanide-doped* $NaYF_4$ *nanoparticles.* Journal of the American Chemical Society **130**(17), 5642 (2008).

[234] F. Wang and X. Liu. *Recent advances in the chemistry of lanthanide-doped upconversion nanocrystals.* Chemical Society Reviews **38**(4), 976 (2009).

[235] N. Wu, H. Chen, Y. Chueh, S. Lin, L. Chou, and W. Hsu. *Doped spiral alumina nanowires.* Chemical Communications **2005**(2), 204 (2005).

[236] J. Zhang, Y. Fu, and J. Lakowicz. *Luminescent silica core/silver shell encapsulated with Eu (III) complex.* The Journal of Physical Chemistry C **113**(45), 19404 (2009).

[237] Y. Jin and X. Gao. *Plasmonic fluorescent quantum dots.* Nature Nanotechnology **4**(9), 571 (2009).

[238] K. Ray, R. Badugu, and J. Lakowicz. *Metal-enhanced fluorescence from* CdTe *nanocrystals: a single-molecule fluorescence study.* J. Am. Chem. Soc **128**(28), 8998 (2006).

[239] H. Mertens and A. Polman. *Plasmon-enhanced erbium luminescence.* Applied Physics Letters **89**, 211107 (2006).

[240] T. Aisaka, M. Fujii, and S. Hayashi. *Enhancement of upconversion luminescence of* Er *doped* Al_2O_3 *films by Ag island films.* Applied Physics Letters **92**(13), 132105 (2008).

[241] T. Som and B. Karmakar. *Nanosilver enhanced upconversion fluorescence of erbium ions in* Er : Ag-*antimony glass nanocomposites.* Journal of Applied Physics **105**, 013102 (2009).

[242] L. Sudheendra, J. Han, and I. Kennedy. *Frster resonance energy transfer measurement from a gold coated upconverting nanophosphor.* In *Proceedings of SPIE*, vol. 7576, p. 75760Y (2010).

[243] J. Zhang, R. Badugu, and J. Lakowicz. *Fluorescence quenching of CdTe nanocrystals by bound gold nanoparticles in aqueous solution.* Plasmonics **3**(1), 3 (2008).

[244] Z. Li, Y. Zhang, and S. Jiang. *Multicolor core/shell-structured upconversion fluorescent nanoparticles.* Advanced Materials **20**(24), 4765 (2008).

[245] W. Deng, K. Drozdowicz-Tomsia, D. Jin, and E. Goldys. *Enhanced flow cytometry-based bead immunoassays usingmetal nanostructures.* Analytical chemistry **81**(17), 7248 (2009).

[246] J. Boyer, F. Vetrone, L. Cuccia, and J. Capobianco. *Synthesis of colloidal upconverting* $NaYF_4$ *nanocrystals doped with* Er^{3+}, Yb^{3+} *and* Tm^{3+}, Yb^{3+} *via thermal decomposition of lanthanide trifluoroacetate precursors.* J. Am. Chem. Soc **128**(23), 7444 (2006).

[247] S. Karpov, A. Baśko, A. Popov, V. Slabko, and T. George. *Recent research developments in optics*. Research Signpost, Trivandrum, India (2002).

[248] N. Liu, B. Prall, and V. Klimov. *Hybrid gold/silica/nanocrystal-quantum-dot superstructures: synthesis and analysis of semiconductor-metal interactions*. J. Am. Chem. Soc **128**(48), 15362 (2006).

[249] Y. Chen, K. Munechika, I. Jen-La Plante, A. Munro, S. Skrabalak, Y. Xia, and D. Ginger. *Excitation enhancement of CdSe quantum dots by single metal nanoparticles*. Applied Physics Letters **93**, 053106 (2008).

[250] F. Wang, J. Wang, and X. Liu. *Direct evidence of a surface quenching effect on size-dependent luminescence of upconversion nanoparticles*. Angewandte Chemie International Edition **49**, 7456 (2010).

[251] Q. L, F. Guo, L. Sun, A. Li, and L. Zhao. *Surface modification of* $ZrO_2 : Er^{3+}$ *nanoparticles to attenuate aggregation and enhance upconversion fluorescence*. J. Phys. Chem. C **112**, 2836 (2008).

[252] R. Campbell, O. Tour, A. Palmer, P. Steinbach, G. Baird, D. Zacharias, and R. Tsien. *A monomeric red fluorescent protein*. Proceedings of the National Academy of Sciences of the United States of America **99**(12), 7877 (2002).

[253] W. Denk, J. Strickler, and W. Webb. *Two-photon laser scanning fluorescence microscopy*. Science **248**(4951), 73 (1990).

[254] W. Chan and S. Nie. *Quantum dot bioconjugates for ultrasensitive nonisotopic detection*. Science **281**(5385), 2016 (1998).

[255] C. Bradac, T. Gaebel, N. Naidoo, M. Sellars, J. Twamley, L. Brown, A. Barnard, T. Plakhotnik, A. Zvyagin, and J. Rabeau. *Observation and control of blinking nitrogen-vacancy centres in discrete nanodiamonds*. Nature Nanotechnology **5**(5), 345 (2010).

[256] L. Wang, K. Wang, S. Santra, X. Zhao, L. Hilliard, J. Smith, Y. Wu, and W. Tan. *Watching silica nanoparticles glow in the biological world.* Analytical Chemistry **78**(3), 646 (2006).

[257] J. Wu, Z. Ye, G. Wang, D. Jin, J. Yuan, Y. Guan, and J. Piper. *Visible-light-sensitized highly luminescent europium nanoparticles: preparation and application for time-gated luminescence bioimaging.* Journal of Materials Chemistry **19**(9), 1258 (2009).

[258] S. Botchway, M. Charnley, J. Haycock, A. Parker, D. Rochester, J. Weinstein, and J. Williams. *Time-resolved and two-photon emission imaging microscopy of live cells with inert platinum complexes.* Proceedings of the National Academy of Sciences **105**(42), 16071 (2008).

[259] R. Dale, J. Eisinger, and W. Blumberg. *The orientational freedom of molecular probes. the orientation factor in intramolecular energy transfer.* Biophysical journal **26**(2), 161 (1979).

[260] I. Hemmil and V. Mukkala. *Time-resolution in fluorometry technologies, labels, and applications in bioanalytical assays.* Critical Reviews in Clinical Laboratory Sciences **38**(6), 441 (2001).

[261] J. Yuan and G. Wang. *Lanthanide-based luminescence probes and time-resolved luminescence bioassays.* Trends in Analytical Chemistry **25**(5), 490 (2006).

[262] P. Selvin. *Principles and biophysical applications of luminescent lanthanide probes.* Annu. Rev. Biophys. Biomol. Struct **31**, 275 (2002).

[263] W. Deng, D. Jin, K. Drozdowicz-Tomsia, J. Yuan, and E. Goldys. *Europium chelate (*BHHCT $-$ Eu^{3+}*) and its metal nanostructure enhanced luminescence applied to bioassays and time-gated bioimaging.* Langmuir **26**(12), 10036 (2010).

[264] K. Aslan, I. Gryczynski, J. Malicka, E. Matveeva, J. Lakowicz, and C. Geddes. *Metal-enhanced fluorescence: an emerging tool in biotechnology.* Current Opinion in Biotechnology **16**(1), 55 (2005).

[265] O. Tovmachenko, C. Graf, D. van den Heuvel, A. van Blaaderen, and H. Gerritsen. *Fluorescence enhancement by metal-core/silica-shell nanoparticles.* Advanced Materials **18**(1), 91 (2006).

[266] M. Lessard-Viger, M. Rioux, L. Rainville, and D. Boudreau. *FRET enhancement in multilayer core-shell nanoparticles.* Nano letters **9**(8), 3066 (2009).

[267] Z. Ma, D. Dosev, and I. Kennedy. *A microemulsion preparation of nanoparticles of europium in silica with luminescence enhancement using silver.* Nanotechnology **20**, 085608 (2009).

[268] D. Cheng and Q. Xu. *Separation distance dependent fluorescence enhancement of fluorescein isothiocyanate by silver nanoparticles.* Chemical communications (3), 248 (2007).

[269] P. Lee and D. Meisel. *Adsorption and surface-enhanced Raman of dyes on silver and gold sols.* The Journal of Physical Chemistry **86**(17), 3391 (1982).

[270] S. Liu, Z. Zhang, and M. Han. *Gram-scale synthesis and biofunctionalization of silica-coated silver nanoparticles for fast colorimetric DNA detection.* Anal. Chem **77**(8), 2595 (2005).

[271] U. Resch, A. Eychmller, M. Haase, and H. Weller. *Absorption and fluorescence behavior of redispersible cadmium sulfide colloids in various organic solvents.* Langmuir **8**(9), 2215 (1992).

[272] T. Ung, L. Liz-Marzán, and P. Mulvaney. *Controlled method for silica coating of silver colloids. influence of coating on the rate of chemical reactions.* Langmuir **14**(14), 3740 (1998).

[273] M. Werts, R. Jukes, and J. Verhoeven. *The emission spectrum and the radiative lifetime of* Eu^{3+} *in luminescent lanthanide complexes.* Physical Chemistry Chemical Physics **4**(9), 1542 (2002).

[274] C. Peng, H. Zhang, J. Yu, Q. Meng, L. Fu, H. Li, L. Sun, and X. Guo. *Synthesis, characterization, and luminescence properties of the ternary europium complex covalently bonded to mesoporous SBA-15.* J. Phys. Chem. B **109**(32), 15278 (2005).

Contribution of Authors:

- Chapter 4: Enhanced Flow Cytometry-Based Bead Immunoassays Using Metal Nanostructures

Wei Deng: experiment set-up, sample preparation, data collection and analysis and manuscript preparation, 70%

Krystyna Drozdowicz-Tomsia: data analysis and some parts of manuscript preparation, 15%

Dayong Jin: data collection, 5%

Ewa M Goldys: theoretical analysis and manuscript revision, 10%

- Chapter 5: Metal Nanostructure Enhanced Fluorescence of Europium Chelate BHHCT _Eu^{3+} applied to Bioassays and Time-gated Bioimaging

Wei Deng: experiment set-up, sample preparation, data collection and analysis and manuscript preparation, 70%

Dayong Jin: experiment set-up and data collection, 11%

Drozdowicz-Tomsia: data analysis, 5%

Jingli Yuan: sample supply, 4%

Ewa M Goldys: theoretical analysis and manuscript revision, 10%

- Chapter 7: Upconversion in $NaYF_4$: Yb; Er Nanoparticles Amplified by Metal Nanostructures

Wei Deng: data collection and analysis and manuscript preparation, 45%

Sudheendra Lakshmana: sample supply, 15%

Jiangbo Zhao: data collection, 10%

Junxiang Fu: sample supply, 7%

Ian Kennedy: manuscript revision, 5%

Dayong Jin: lab equipment supply, 3%

Ewa M Goldys: theoretical analysis and manuscript revision, 15%

- Chapter 8: Ultrabright Eu-doped Plasmonic Ag@SiO_2 Nanostructures: Time-gated Bioprobes with Single Particle Sensitivity and Negligible Background

Wei Deng: experiment set-up, sample preparation, data collection and analysis and manuscript preparation, 42%

Dayong Jin: experiment set-up, data collection and analysis and some parts of manuscript preparation, 20%

Krystyna Drozdowicz-Tomsia: data collection and analysis, 10%

Yingli Yuan: sample supply, 4%

Jing Wu: sample supply, 4%

Ewa M Goldys: theoretical analysis and manuscript revision, 20%